université PARIS-SACLAY

Novel high-Q musical instrument-inspired MEMS structures

Nouvelles structures MEMS à fort facteur de qualité inspirées d'instruments de musique

Thèse de doctorat de l'université Paris-Saclay

École doctorale n°575 : electrical, optical, bio : physics and engineering (EOBE)
Spécialité de doctorat : Electronique, Photonique et Micro-Nanotechnologies
Graduate School : Sciences de l'ingénierie et des systèmes.
Référent : Faculté de Sciences d'Orsay

Thèse préparée dans la unité de recherche **Centre de Nanosciences et de Nanotechnologies (CNRS, Université Paris-Saclay)**, sous la direction de **Alexis BRENES**, Maître de conférences, le co-encadrement de **Elie LEFEUVRE**, Professeur

Thèse soutenue à Paris-Saclay, le 30 Septembre 2026, par

Tong ZHU

Composition du jury

Membres du jury avec voix délibérative

Adrien PELAT Professeur, LAUM, Le Mans Université	Président
Olivier THOMAS Professeur, Arts et Métiers ParisTech	Rapporteur & Examinateur
Samuel MARGUERON Professeur, FEMTO-ST, Université de Franche-Comté	Rapporteur & Examinateur
Ashwin SESHIA Professeur, University of Cambridge	Examinateur
Pascal NOUET Professeur, LIRMM, Université de Montpellier	Examinateur
Aleksandra MARKOVIC Chercheuse, ESYCOM, Université Gustave Eiffel	Examinatrice

THESE DE DOCTORAT
NNT : 2026UPAST108

université PARIS-SACLAY

ÉCOLE DOCTORALE
Physique et ingénierie : Electrons, Photons, Sciences du vivant (EOBE)

Titre : Nouvelles structures MEMS à fort facteur de qualité inspirées d'instruments de musique
Mots clés : MEMS, Résonateurs, Cloches plates, Fabrication SOI, Caractérisation, Fort facteur de qualité

Résumé : Cette thèse présente une nouvelle famille de résonateurs MEMS à facteur de qualité élevé, inspirée d'instruments de musique composés des plaques trapézoïdales appelés " en cloche plates" ou "bell plate" en anglais. Le concept proposé exploite la ligne nodale en forme de U contrôlable du mode de résonance (2,0) afin de réduire les pertes au niveau des ancrages, tout en conservant une géométrie plane simple compatible avec les procédés de fabrication MEMS standard sur silicium. Une méthodologie de conception complète, combinant optimisation structurelle, modélisation électromécanique, fabrication et validation expérimentale, est mise en place. Des plaques macroscopiques sont d'abord étudiées afin d'identifier la relation entre la géométrie, la position de la ligne nodale et le facteur de qualité. Des mesures expérimentales démontrent que les prototypes optimisés atteignent des facteurs de qualité allant jusqu'à 8 769 tout en conservant des fréquences de résonance proches de 642 Hz. La méthodologie est ensuite transposée aux résonateurs MEMS SOI utilisant un procédé de fabrication SOI standard. Une configuration d'électrodes optimisée est proposée et développée pour les modes d'ordre supérieur. Des mesures optiques vérifient la conception des cloches plates MEMS, les résonateurs fonctionnant à 180 kHz atteignant des facteurs de qualité d'environ $1,4 \times 10^5$. L'actionnement électrostatique et la détection capacitive, associés à une conception optimisée des électrodes, sont en outre démontrés sur des dispositifs SOI fortement dopés. Ces travaux établissent l'ingénierie des lignes nodales comme une stratégie efficace pour réduire les pertes d'ancrage et fournissent une méthodologie de conception pratique pour les futurs résonateurs, oscillateurs et capteurs résonants MEMS à haut Q.

Title : Novel high-Q instrument-inspired MEMS structures
Keywords : MEMS, Resonators, Bell plates, SOI fabrication, Characterization, High Q-factor

Abstract : This thesis presents a new family of high-quality-factor MEMS resonators inspired by trapezoidal bell plates. The proposed concept exploits the controllable U-shaped nodal line of the (2,0)-ringing-mode to reduce anchor loss while maintaining a simple planar geometry compatible with standard silicon MEMS fabrication. A complete design methodology combining structural optimization, electromechanical modelling, fabrication and experimental validation is established. Macroscopic bell plates are first investigated to identify the relationship between geometry, nodal-line position and quality factor. Experimental measurements demonstrate that optimized prototypes achieve quality factors up to 8769 while maintaining resonance frequencies near 642 Hz. The methodology is then transferred to SOI MEMS resonators with standard SOI fabrication process. A optimization electrode configuration is proposed and developed for higher-order gap-closing modes. Optical measurements verify the MEMS bell plate design, with resonators operating at 180 kHz achieving quality factors of approximately 1.4×10^5. Electrostatic actuation and capacitive detection with optimized electrode design are further demonstrated on highly doped SOI devices. This work establishes nodal-line engineering as an effective strategy for reducing anchor loss and provides a practical design methodology for future high-Q MEMS resonators, oscillators and resonant sensors.

Table of contents

ACKNOWLEDGEMENTS 7

LIST OF ABBREVIATIONS 9

LIST OF NOTATIONS 11

RÉSUMÉ 15

INTRODUCTION 21

1 STATE OF ART OF HIGH-Q MEMS RESONATORS 23
- 1.1 INTRODUCTION . . . 23
- 1.2 HIGH-Q MEMS . . . 23
- 1.3 ENERGY LOSSES SOURCES IN MEMS . . . 25
  - 1.3.1 AIR DAMPING . . . 25
  - 1.3.2 THERMOELASTIC DAMPING . . . 27
  - 1.3.3 ANCHOR LOSSES . . . 30
  - 1.3.4 OTHER DISSIPATION MECHANISMS . . . 31
- 1.4 CLASSIFICATION AND DESIGN STRATEGIES OF HIGH-Q MEMS RESONATORS . . . 33
  - 1.4.1 POSITIONING OF BELL PLATE RESONATOR WITHIN THE STATE-OR-ART . . . 34
- 1.5 STATE OF THE ART OF BELL PLATE . . . 35
- 1.6 ANALYSIS OF BELL PLATE DISSIPATION SOURCE . . . 38
- 1.7 CONCLUSION . . . 40

2 PRELIMINARY STUDY ON MACROSCOPIC BELL PLATE 43
- 2.1 INTRODUCTION . . . 43
- 2.2 OVERALL DESIGN . . . 43
- 2.3 MODELING OF MACROSCOPIC BELL PLATES . . . 43
  - 2.3.1 OBSERVATIONS ON THE FIRST VIBRATION MODES OF A BELL PLATES . . . 43
  - 2.3.2 QUALITY FACTOR OPTIMIZATION OF THE (2,0)-MODE . . . 46
- 2.4 FIRST QUANTITATIVE CHARACTERIZATION OF MACROSCOPIC BELL PLATE . . . 48
  - 2.4.1 EXPERIMENTAL SETUP AND CHARACTERISTIC OF THE BELL PLATES . . . 49
  - 2.4.2 RING-DOWN CHARACTERIZATION . . . 50
  - 2.4.3 FREQUENCY RESPONSE OF THE (2,0)-MODE . . . 52
- 2.5 CONCLUSION . . . 54

3 DESIGN AND FABRICATION OF MEMS BELL PLATE ON SOI WAFERS 57
- 3.1 INTRODUCTION . . . 57
- 3.2 DESIGN OF MICROSCOPIC BELL PLATE . . . 57
  - 3.2.1 DESIGN STRATEGY . . . 58
  - 3.2.2 FINAL DESIGNS . . . 60
- 3.3 FABRICATION OF MICROSCOPIC BELL PLATE ON SOI WAFER . . . 63
  - 3.3.1 FABRICATION PROCESS . . . 63
  - 3.3.2 SPIN COATING . . . 64

3.3.3 LITHOGRAPHY . . . 66
3.3.4 DRIE . . . 66
3.3.5 XeF_2 ETCHING . . . 68
3.3.6 METAL DEPOSITION . . . 68
3.3.7 CLEANING . . . 68
3.3.8 HF RELEASE ETCHING . . . 68
3.3.9 SIMPLIFIED FABRICATION PROCESS . . . 69
3.4 SCANNING ELECTRON MICROSCOPE (SEM) PHOTOS . . . 70
3.5 CONCLUSION . . . 70

4 CHARACTERIZATION OF MEMS BELL PLATE SYSTEM 75
4.1 INTRODUCTION . . . 75
4.2 SIMULATION OF MEMS BELL PLATE . . . 75
4.3 STATIC MEASUREMENTS . . . 77
4.3.1 SURFACE PROFILE . . . 77
4.3.2 STIFFNESS . . . 77
4.4 DYNAMIC MEASUREMENTS . . . 78
4.4.1 INSTRUMENTS AND SETUP CONFIGURATION . . . 78
4.4.2 FREQUENCY RESPONSE . . . 80
4.4.3 TEMPERATURE COEFFICIENT OF FREQUENCY (TCF) . . . 82
4.4.4 EVOLUTION OF RESONANT FREQUENCY AND Q WITH DC BIAS . . . 83
4.4.5 EVOLUTION OF Q WITH AMBIENT PRESSURE . . . 85
4.5 CONCLUSION . . . 86

5 ELECTRODE OPTIMIZED MEMS BELL PLATE 89
5.1 INTRODUCTION . . . 89
5.2 THEORETICAL CALCULATION OF ELECTRODE OPTIMIZATION . . . 89
5.3 SIMULATION OF ELECTRODE OPTIMIZATION . . . 92
5.4 OPTICAL DETECTION . . . 93
5.5 ELECTRICAL DETECTION . . . 94
5.5.1 ELECTRICAL CIRCUIT CONFIGURATION . . . 94
5.5.2 ELECTRICAL SIGNAL . . . 98
5.6 CONCLUSION . . . 99

6 CONCLUSION AND FUTURE PERSPECTIVES 101
6.1 SUMMARY OF THIS WORK . . . 101
6.2 FUTURE PERSPECTIVES . . . 102

APPENDIX 105
A EVOLUTION OF NATURAL FREQUENCY TO L_e . . . 105
A.1 FIRST BENDING MODE . . . 105
A.2 (2,0)-MODE . . . 106
A.3 CONCLUSION . . . 106
B SUPPLEMENTARY SEM PHOTOS . . . 107

LIST OF FIGURES 112

LIST OF TABLES 113

LIST OF PUBLICATIONS 115

REFERENCES 117

ACKNOWLEDGEMENTS

First and foremost, I would like to express my deepest gratitude to my supervisor, Alexis Brenes, for his unwavering support throughout my PhD. Whenever I encountered difficulties in my experiments, he was always willing to search for solutions with enthusiasm and determination. His outstanding expertise consistently helped me overcome technical challenges. He closely followed the progress of my research and carefully reviewed every detail of every manuscript I wrote. Above all, I am truly grateful for his patience, encouragement, and constant guidance throughout these years. I would also like to express my sincere gratitude to my adviser, Elie Lefeuvre. He was always generous with his time and knowledge, never hesitating to provide help whenever it was needed. His extensive expertise in MEMS and his remarkable ability to identify the key directions of the project provided invaluable guidance at every stage of my research. The successful completion of this work would not have been possible without the support and complementary guidance of both Alexis and Elie.

I am sincerely grateful to the members of my PhD defence jury, Samuel Margueron, Olivier Thomas, Pascal Nouet, Ashwin Seshia, Adrien Pelat and Aleksandra Markovic, for accepting to serve on my jury and for dedicating their time and expertise to the evaluation of my work.

My sincere thanks also go to Alain Bosseboeuf[1], who designed and built the vacuum chamber, undoubtedly the most essential part of my experimental setup. His dedication to research and his professionalism have always been a source of inspiration for me. As the initiator of this project, his extensive experience proved invaluable in every aspect of my work. I would also like to thank Muriel Thomasset[1] for her help in building the optical part of the experimental setup. Without their contributions, the realization of this experimental platform would not have been possible.

I would also like to thank the members of my annual Comité de Suivi Individuel : Jérôme Julliard[2], Michael Bahriz[3], and Andrea Barbarulo[4], for their constructive discussions and valuable advice throughout my doctoral studies. I would like to express my special thanks to Jérôme, who gave me advice throughout my PhD and designed the electrical detection circuit used in my experiments.

I also thank Etienne Herth[1], with whom I spent countless hours working on the fabrication process. His support and collaboration were invaluable during sample fabrication. I would also like to acknowledge all the engineers who contributed to the fabrication of my devices, especially David Bouville[1], Samson Edmond[1] and Téo Baptiste[1].

I am grateful to everyone in the MNBF Department, Pierre-Yves Jouber[1], Philippe Coste[1], Emile Martincic[1], Mehdi Amar[1], Clément Bessoue[1], Fabien Parrain[1], Gwenaël Bacon[1] and Charlotte Kutyla[1], for their assistance and for creating such a welcoming and supportive working environment.

I would also like to thank all the PhD students in the department, particularly Sarra Riahi[1], Alejandro Godinez Perez Medina[12], and Ayoub Dahani[1], who patiently taught me how to use many of the experimental instruments that were essential to my research. I am also grateful to our former intern, Rania Belmekki[1], for her valuable assistance with part of the experimental measurements.

Finally, I would like to express my heartfelt gratitude to my parents for their uncon-

ditional love, encouragement, and support throughout this journey. I also gratefully acknowledge the support provided by my laboratory, the doctoral school, and the university.

Last but certainly not least, I would like to thank all the people mentioned above, as well as all my friends who have accompanied me over the past few years. Your kindness, encouragement, and support have meant more than words can express. This thesis would not have been possible without you.

1. C2N, CNRS, Université Paris-Saclay
2. GeePs, CNRS, CentraleSupélec, Université Paris-Saclay, Sorbonne Université
3. IES, CNRS, Université de Montpellier
4. LMPS, CNRS, ENS Paris-Saclay, CentraleSupélec, Université Paris-Saclay

LIST OF ABBREVIATIONS

AC	Alternating Current
BAW	Bulk Acoustic Wave
BOX	Buried Oxide
CTE	Coefficient of Thermal Expansion
DC	Direct Current
DI	Deionised
DRIE	Deep Reactive Ion Etching
FEM	Finite Element Method
FWHM	Full Width at Half Maximum
HARPSS	High-Aspect-Ratio Poly and Single-Crystal Silicon
HF	Hydrofluoric Acid
ICP	Inductively Coupled Plasma
IPA	Isopropyl Alcohol
LN	Lithium Niobate
MEMS	Micro-ElectroMechanical Systems
PCB	Printed Circuit Board
PLL	Phase-Locked Loop
PML	Perfectly Matched Layer
PVD	Physical Vapour Deposition
Q	Quality Factor
RF	Radio Frequency
SAW	Surface Acoustic Wave
SCS	Single-Crystal Silicon
SEM	Scanning Electron Microscope
SH-SAW	Shear-Horizontal Surface Acoustic Wave
SiBAR	Silicon Bulk Acoustic Resonator
SOI	Silicon-On-Insulator
TCF	Temperature Coefficient of Frequency
TED	Thermoelastic Damping
UV	Ultraviolet
VHF	Vapour-Phase Hydrofluoric Acid Etching

LIST OF NOTATIONS

LATIN SYMBOLS

A	Vibration amplitude
A_i	Initial vibration amplitude of the ith mode
A_p	Plate area
A_{tot}	Total displacement amplitude of the ring-down response
a, b	In-plane dimensions of a rectangular plate
C	Electrical capacitance
C_0	Static capacitance
C_m	Motional component of the capacitance
C_p	Specific heat capacity
C_par	Parasitic capacitance
C_{comp}	Compensation capacitance
$C_{\mathrm{p}}^{\mathrm{th}}$	Specific heat capacity at constant pressure
c_{Bao}	Squeeze-film damping coefficient given by Bao's model
$c_{\mathrm{Christian}}$	Free-molecular damping coefficient given by Christian's model
d	Characteristic dimension of the resonator–support contact
E	Young's modulus
E_{stored}	Mechanical energy stored in the resonator
$E_{\mathrm{dissipated}}$	Energy dissipated during one oscillation cycle
f	Vibration frequency
f_0	Resonant frequency
$f_{\mathrm{TED,min}}$	Frequency corresponding to maximum thermoelastic dissipation
F	Applied force
F_m	Modal electrostatic driving force
$F_{m,\mathrm{max}}$	Maximum modal driving force
g	Initial electrode gap
G	Overall measurement gain
h	Characteristic air gap
h_{diff}	Effective thermal diffusion length
i_m	Motional current
$i_{m,\mathrm{max}}$	Maximum motional current
I_{out}	Total measured output current
I_{mot}	Motional-current component
I_{ft}	Electrical feedthrough-current component

k	Mechanical stiffness
k_{B}	Boltzmann constant
k_e	Electrostatic stiffness
k_{eq}	Equivalent mechanical stiffness
k_m	Modal stiffness
k_R	Characteristic resonator wavenumber
K_s	Knudsen number
L	Length of the triangular part of the bell plate
L_e	Length of the plate-edge extension
L_t	Length of the tang
L_{tot}	Total length of the bell plate
L_{circ}	Circumference of the plate
m_{eff}	Effective modal mass
m_m	Mass of a gas molecule
p_m	Thermoelastic modal participation factor
P	Ambient pressure
Q	Overall quality factor
Q_{air}	Quality factor limited by air damping
Q_{anchor}	Quality factor limited by anchor loss
Q_{others}	Quality factor associated with other dissipation mechanisms
Q_{SFD}	Quality factor limited by squeeze-film damping
Q_{TED}	Quality factor limited by thermoelastic damping
$Q_{\mathrm{TED},m}$	Thermoelastic quality factor of the mth mode
$Q_{\mathrm{TED,min}}$	Minimum quality factor predicted from thermoelastic damping
Q_{Zener}	Thermoelastic quality factor predicted by the Zener model
$\mathbf{r}$	Position vector
S	Electrode area or resonator–support contact area
t	Time
T	Plate thickness
T_0	Reference absolute temperature
$\mathbf{u}'_R$	Displacement field of the resonator mode
$\mathbf{u}_q^{(0)}$	Displacement field of the qth substrate mode
V_b	DC bias voltage
V_{ac}	Amplitude of the AC driving voltage
$v_{\mathrm{ac}}(t)$	Time-dependent AC driving voltage
$\widetilde{V}_{\mathrm{comp}}$	Complex compensation voltage
$w(\mathbf{r}, t)$	Total out-of-plane displacement field
W	Width of the bell plate

W_t	Width of the tang
x	Mechanical displacement
x_0	Static modal coordinate
$x_m(t)$	Time-dependent coordinate of the mth vibration mode
$x_{m,\max}$	Maximum modal displacement

GREEK SYMBOLS

α	Coefficient of thermal expansion
γ	Cubic stiffness or Duffing nonlinearity coefficient
Δ	Thermoelastic coupling factor
Δf	Full width at half maximum of the resonance peak
ε_0	Vacuum permittivity
ζ	Mechanical damping ratio
η	Electrostatic modal coupling coefficient
η_i	Voltage–frequency transduction coefficient of the ith mode
κ	Voltage–frequency transduction coefficient of the ith mode
λ	Plate eigenvalue
Λ	Molecular mean free path
μ	Dynamic viscosity of the surrounding gas
ν	Poisson's ratio
ρ	Material density
ρ_R	Density of the resonator
ρ_s	Density of the substrate
$\boldsymbol{\sigma}'_R$	Stress field of the resonator mode
$\boldsymbol{\sigma}_q^{(0)}$	Stress field of the qth substrate mode
τ	Phonon relaxation time
τ_{TH}	Thermal relaxation time
ϕ_i	Initial phase of the ith vibration mode
$\phi_0(\mathbf{r})$	Normalised static deformation shape
$\phi_m(\mathbf{r})$	Normalised shape of the mth vibration mode
χ	Thermal diffusivity
ω	Angular excitation frequency
ω_0	Resonant angular frequency
ω_i	Angular frequency of the ith vibration mode
ω_n	Natural angular frequency
ω_R	Angular frequency of the resonator mode
$\omega(q)$	Angular frequency of the qth substrate mode

RÉSUMÉ

Cette thèse propose une nouvelle structure de résonateurs MEMS à haut facteur de qualité inspirée des cloches plates (*bell plates*). Contrairement à la plupart des résonateurs MEMS conventionnels, dont les performances reposent sur des structures fortement symétriques ou sur des techniques complexes de confinement acoustique, l'approche développée dans ce travail consiste à réduire les pertes d'ancrage en contrôlant la position de la ligne nodale du mode de vibration (2,0). L'objectif principal de cette thèse est ainsi d'établir une méthodologie complète permettant de concevoir, fabriquer et caractériser cette nouvelle famille de résonateurs tout en conservant une géométrie planaire compatible avec les procédés standards de microfabrication sur silicium.

Le travail présenté s'articule autour d'une démarche progressive allant de l'étude des cloches plates macroscopiques jusqu'à la réalisation des premiers prototypes MEMS. Cette approche permet d'identifier les mécanismes physiques gouvernant les performances vibratoires avant leur transposition à l'échelle microscopique.

Une première partie du travail est consacrée à la compréhension des propriétés dynamiques des cloches plates. Une analyse numérique et théorique de ces plaques permet d'identifier l'impact des différentes dimensions du résonateur sur ses propriétés de résonance. Deux échantillons de plaques macroscopiques sont fabriqués et testés dans différentes conditions expérimentales pour mettre en particulier en évidence la dépendance du facteur de qualité à une des dimensions (longueur du bord - "edge") critiques de la plaque. Les plaques de cloche présentent une propriété particulièrement intéressante : le mode de vibration (2,0) possède une ligne nodale en forme de « U » dont la position dépend directement de la géométrie de la plaque. Lorsque cette ligne nodale est rapprochée de l'ancrage, notamment grâce à l'ajustement de cette dimension du bord, la transmission des ondes élastiques vers le substrat est fortement réduite, ce qui conduit naturellement à une augmentation du facteur de qualité.

Afin de comprendre quantitativement ce mécanisme, une étude complète a été réalisée sur des cloches plates macroscopiques (voir la Figure 1). Des modèles analytiques décrivant les fréquences propres du mode (2,0) ont été développés puis validés par simulations numériques utilisant la méthode des éléments finis, en se référant à la Figure 2. Une étude paramétrique met en évidence que les différents paramètres géométriques ne jouent pas le même rôle dans la conception du résonateur. En particulier, la longueur du prolongement rectangulaire L_e contrôle principalement la position de la ligne nodale tout en modifiant très faiblement la fréquence propre. Cette observation constitue un résultat important de cette thèse puisqu'elle montre qu'il est possible d'optimiser le facteur de qualité sans remettre en cause la fréquence de fonctionnement.

Des cloches plates en acier inoxydable ont été fabriquées et caractérisées expérimentalement par mesures de décroissance libre (*ring-down*) et par balayage fréquentiel. Elles présentent une résonance à haut facteur de qualité ($Q = 8769$) aux alentours de 640 Hz, soit une valeur environ 50 fois supérieure au facteur de qualité du premier mode de flexion des plaques elles-mêmes, situé vers 60 Hz. Les résultats obtenus confirment les prédictions issues des simulations numériques. Les dispositifs dont la ligne nodale est située au plus près de l'ancrage présentent systématiquement les facteurs de qualité les plus élevés. Cette étude permet ainsi d'établir une véritable méthodologie de conception

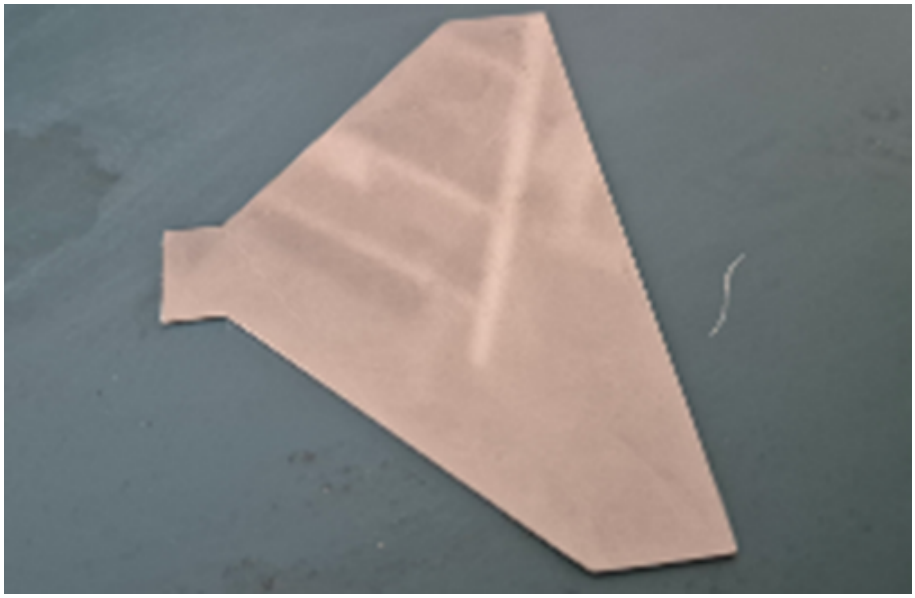

Figure 1 – Photo d'une cloche plate en métal fabriquée dans l'atelier de notre laboratoire.

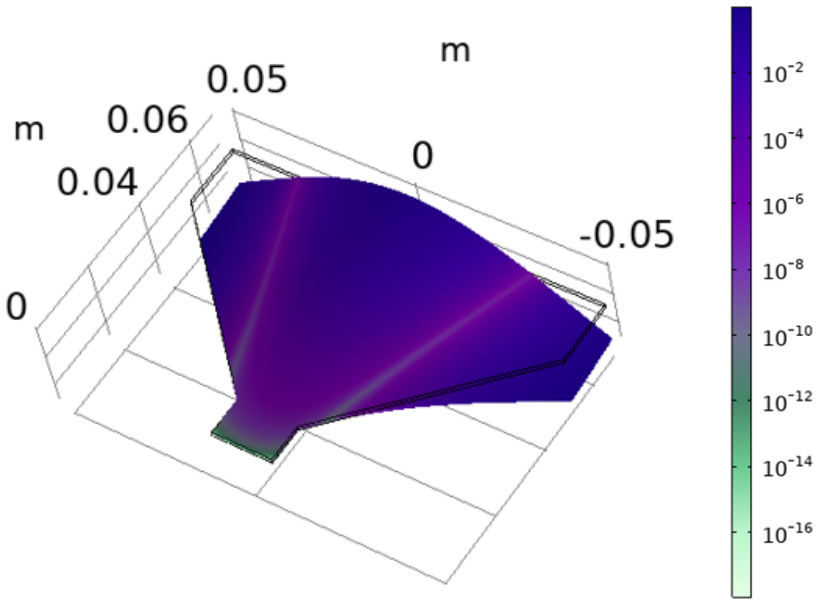

Figure 2 – Simulation par éléments finis de la déformée du mode (2,0) d'une cloche plate.

reliant directement les paramètres géométriques, la position de la ligne nodale, les pertes d'ancrage et le facteur de qualité.

Cette méthodologie est ensuite transposée aux résonateurs MEMS réalisés sur substrats SOI. Cette approche relie directement les paramètres géométriques aux performances mécaniques du résonateur et fournit ainsi des règles de conception pouvant être appliquées à d'autres structures MEMS fonctionnant sur des modes de vibration d'ordre élevé. La réduction d'échelle ne constitue pas une simple miniaturisation de la structure macroscopique ; elle nécessite de prendre en compte les contraintes liées aux procédés de microfabrication, aux propriétés mécaniques du silicium monocristallin ainsi

qu'au choix du mécanisme d'actionnement électrostatique. Une stratégie de conception spécifique est donc développée afin de satisfaire simultanément les contraintes de fréquence de résonance, de facteur de qualité, de tension d'actionnement et de faisabilité technologique.

Le procédé de fabrication développé dans cette thèse repose sur une technologie SOI basée sur des procédés classiques de microfabrication MEMS. Après la définition des différentes étapes technologiques, plusieurs générations de dispositifs ont été réalisées afin de valider la faisabilité de cette nouvelle structure. Les procédés développés comprennent notamment la photolithographie, la gravure profonde du silicium (DRIE), la métallisation ainsi que la libération des structures suspendues par gravure de la couche d'oxyde enterrée.

Par la suite, la première série de prototypes, telle qu'illustrée à la figure 3, a été caractérisée par des mesures optiques. Les mesures optiques permettent de vérifier les fréquences propres ainsi que les formes modales prédites par les simulations numériques. Pour la première série d'échantillons, seules des expériences portant sur les propriétés mécaniques ont été menées, toutes à l'aide d'un vibromètre laser-Doppler.

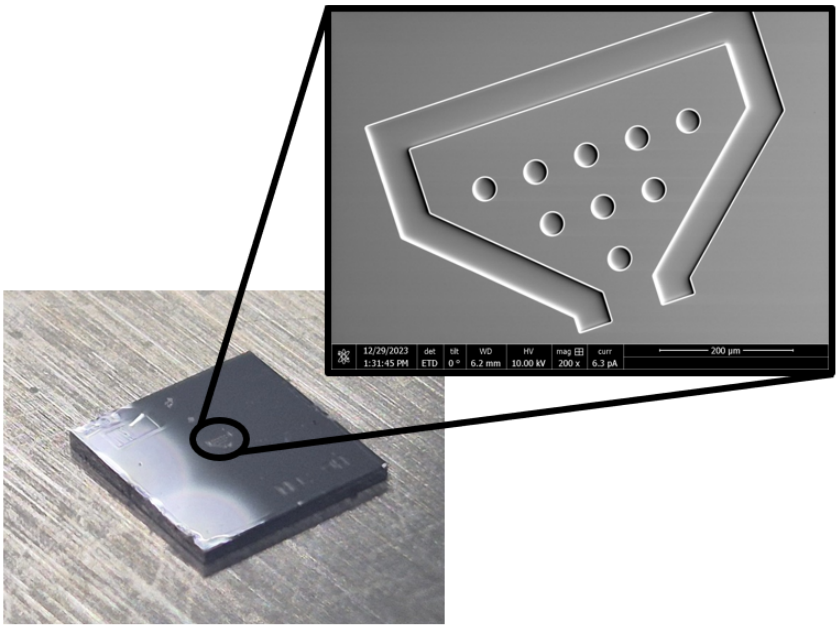

Figure 3 – Prototype MEMS réalisé sur substrat SOI, photo et image MEB.

Une caractérisation approfondie du lot initial de plaques MEMS en forme de cloche a été réalisée, incluant la détermination d'indicateurs de performance clés et une analyse comparative de différentes conceptions (voir la Figure 4). Nous avons caractérisé quatre échantillons présentant expérimentalement une résonance à haut facteur de qualité (Q) pour leur mode (2,0) aux alentours de 180 kHz. L'échantillon le plus performant a atteint un facteur de qualité de 160 k à 15 °C. Cette valeur est plus de deux fois supérieure à celle du premier mode de flexion (qui résonnait à 17 kHz). Cette conception permet ainsi d'obtenir un produit $f \times Q$ supérieur à 28 GHz. Une analyse détaillée et une interprétation des mesures ont été incluses dans cette étude. Pour le mode (2,0) de l'un des échantillons,

nous avons mesuré l'évolution de la fréquence de résonance et du facteur de qualité en fonction de la température, de la tension de polarisation continue (DC) et de la pression. Les mesures indiquent qu'une pression inférieure à 10^{-2} Pa était nécessaire pour que l'amortissement dû à l'air (par exemple, l'amortissement par film d'air comprimé et/ou l'amortissement visqueux) devienne négligeable par rapport aux pertes à l'encastrement, même pour des amplitudes de mouvement aussi faibles que 1 nm, niveau auquel les pertes peuvent être linéarisées. Par ailleurs, pour du silicium faiblement dopé, le coefficient de température de la fréquence (TCF) du mode (2,0) a été mesuré à -48 ppm/°C, une valeur inférieure à celle du premier mode (-85 ppm/°C). Ces résultats soulignent l'intérêt des cloches plates pour les applications MEMS.

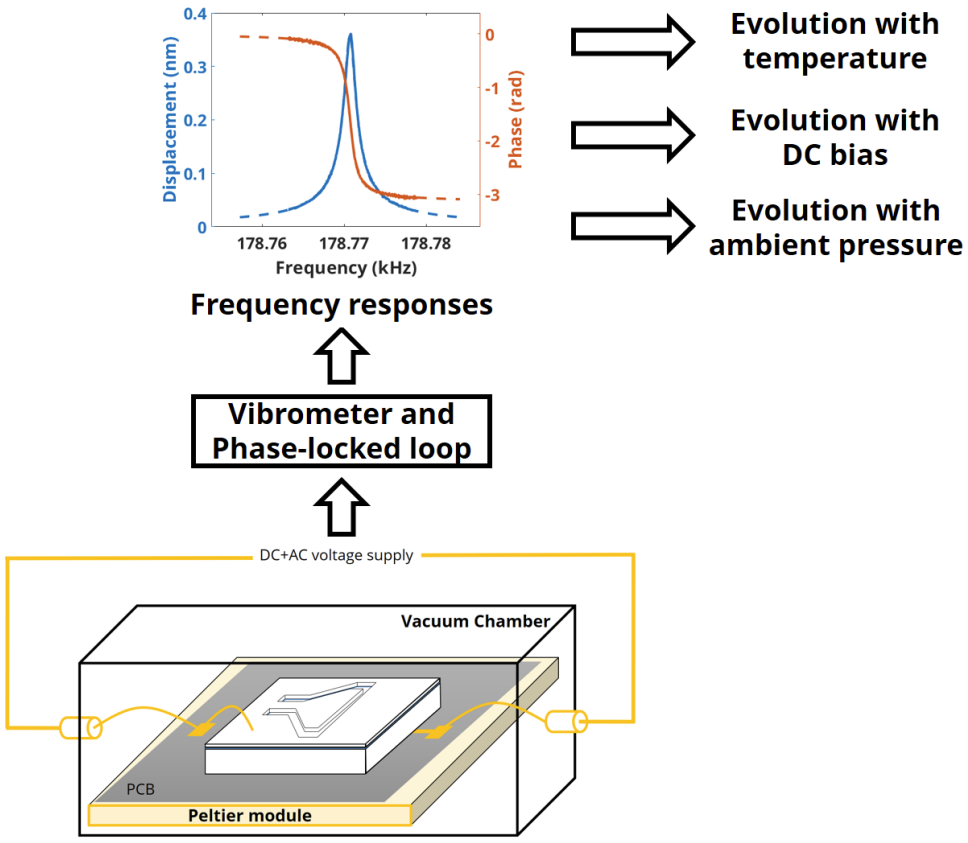

Figure 4 – Schéma du dispositif de caractérisation et de la configuration du MEMS pour une caractérisation complète.

Par la suite, une électrode optimisée et un circuit de réduction des capacités parasites ont été utilisés (voir la Figure 5). Le second résonateur à cloche plate MEMS a permis la détection électrique. Avec une déformation (par vibration mécanique) d'environ $50nm$, soit seulement 5% du gap, nous avons obtenu un signal de détection d'environ $0.04mV$ (avec un circuit amplificateur de courant). Ces résultats confirment donc pour la première fois, de manière expérimentale, la faisabilité d'un résonateur MEMS inspiré des cloches plates. Malheureusement, ces derniers échantillons utilisés pour la détection électrique présentent des défauts de fabrication notamment liés à l'utilisation de gravure HF en présence de silicium fortement dopé et d'électrodes d'or, qui a significativement déterioré la surface de l'échantillon. Une optimisation du procédé de fabrication, associée à une

amélioration de la géométrie des électrodes et à une encapsulation sous vide, devrait permettre de retrouver, sur ces derniers échantillons, le facteur de qualité obtenu dans le premier lot (sur le premier design) et ainsi d'augmenter significativement le facteur de qualité du dispositif. Une utilisation en régime d'oscillation plus large - incluant la non-linéarité d'actionnement et de détection électrique, ainsi qu'une éventuelle non-linéarité géométrique - permettra probablement à l'avenir d'améliorer significativement l'amplitude du signal électrique de résonance.

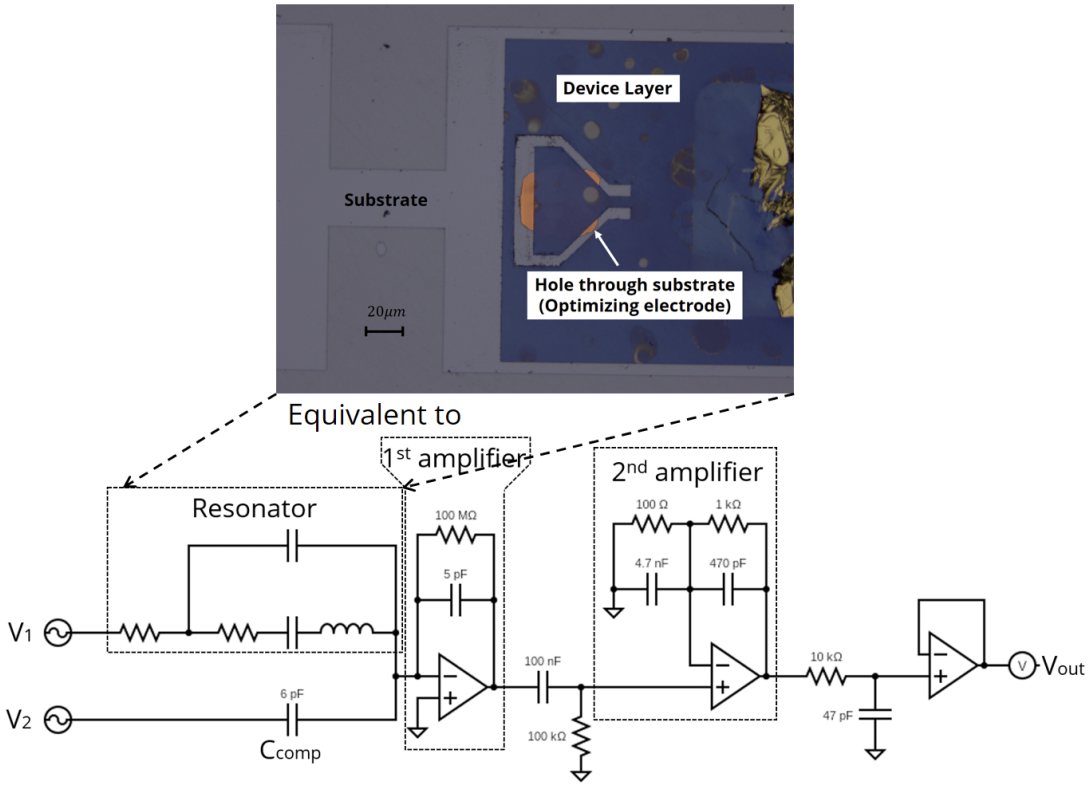

Figure 5 – un circuit de détection électrique permettant de réduire la capacité parasite, accompagné d'une photo d'un échantillon de cloche plate à électrode optimisée.

Les résonateurs inspirés des cloches plates présentent un fort potentiel pour de nombreuses applications. Leur faible fréquence de fonctionnement comparée aux résonateurs classiquement utilisés dans les horloges MEMS, leur facteur de qualité élevé ainsi que leur compatibilité avec l'actionnement électrostatique à très faibles tensions en font des candidats prometteurs pour des oscillateurs MEMS basse consommation. Leur utilisation en tant que capteur résonant pourrait également être envisagée. Plus généralement, les principes de conception développés dans cette thèse pourront être étendus à d'autres structures MEMS reposant sur l'ingénierie des formes modales afin de limiter les pertes d'ancrage et d'améliorer les performances dynamiques.

En conclusion, cette thèse démontre qu'une approche inspirée des cloches plates permet de développer une nouvelle famille de résonateurs MEMS à haut facteur de qualité. En établissant une méthodologie reliant la conception géométrique, la modélisation multiphysique, la fabrication et la validation expérimentale, ce travail pose les bases du développement futur de résonateurs MEMS fondés sur le contrôle des formes modales.

INTRODUCTION

Microelectromechanical systems (MEMS) resonators have become key components in a wide range of modern technologies, including timing references, radio-frequency communication systems, inertial sensors, biological sensors and precision measurement instruments [1]. By enabling efficient energy exchange between the electrical and mechanical domains, they can operate either as actuators, sensors, or self-sustained oscillators, depending on the application [2]. Their compatibility with silicon microfabrication further allows the realization of compact, low-power and highly integrated systems, making MEMS resonators increasingly attractive for both industrial and scientific applications [3, 4].

Regardless of their specific application, the performance of a resonant MEMS device is fundamentally governed by the properties of its mechanical resonator. Among the various performance metrics, the mechanical quality factor (Q) occupies an important position, as it directly influences energy dissipation, frequency stability, phase noise, resolution and sensitivity [5, 6]. A resonator capable of storing mechanical energy over many vibration cycles generally exhibits superior performance in sensing, frequency control and signal processing. For this reason, improving the quality factor has become one of the principal objectives in the development of MEMS resonators [5].

The quality factor is ultimately limited by the mechanisms through which mechanical energy is dissipated [6]. Depending on the resonator geometry, material properties and operating conditions, several loss mechanisms may contribute to the overall energy dissipation. Considerable efforts have therefore been devoted to understanding these mechanisms and to developing resonator designs capable of minimizing their influence. Over the past decades, advances in both theoretical modelling and microfabrication have enabled the realization of resonators with quality factors ranging from several thousands to several millions, depending on the operating frequency and vibration mode [2].

Beyond the understanding of dissipation mechanisms, the geometry of the resonator itself plays a fundamental role in determining its dynamic behaviour. Throughout the evolution of MEMS resonators, numerous structures have been proposed, including cantilevers, doubly-clamped beams, tuning forks, rings, disks, wheels, frames and bulk acoustic resonators [1, 2]. Each structure offers a different compromise between resonance frequency, quality factor, mechanical robustness, fabrication complexity and transduction efficiency [7, 8, 9]. Rather than converging towards a single optimal geometry, the diversity of resonator structures reflects the diversity of application requirements and the continuous search for improved mechanical performance. Consequently, the exploration of new resonator geometries remains an active research direction in MEMS resonator design.

Among these emerging structures, the bell-inspired resonator represents a particularly interesting yet largely unexplored configuration. Inspired by the vibration characteristics of handbells [10], this structure differs significantly from conventional beam- or ring-based resonators in both its geometry and its vibration behaviour. In contrast with classical resonator structures that have been extensively investigated over several decades, the bell-inspired MEMS resonator has not yet been the subject of a systematic study. Its vibration characteristics, dominant dissipation mechanisms, fabrication constraints and electrical transduction principles remain largely unknown. As a result, its potential advan-

tages, limitations and possible application domains have yet to be established.

The objective of this thesis is therefore not simply to demonstrate the operation of a bell-inspired MEMS resonator [10, 11], but rather to establish a comprehensive understanding of this emerging resonator structure. The work combines theoretical modelling, finite-element simulations, microfabrication and experimental characterization to investigate the behaviour of bell-inspired resonators from multiple perspectives. Particular attention is devoted to understanding the physical mechanisms governing their dynamic behaviour, evaluating their achievable performance and developing practical methodologies for their electrical actuation and detection. Through this systematic investigation, the thesis aims to determine whether the bell-inspired structure can provide an attractive alternative to more conventional MEMS resonator geometries.

This manuscript is organized into four main chapters. Following the present general introduction, Chapter 1 reviews the theoretical background of MEMS resonators and discusses the main energy dissipation mechanisms governing their performance, providing the physical basis for the subsequent study. Chapter 2 then introduces the macroscopic metallic bell plates and investigates their dynamic characteristics through numerical modelling and simulations, with the aim of establishing a systematic understanding of this new resonator structure. Chapter 3 presents the design strategy and detailed the fabrication process. Next, in Chapter 4 , the optical characterization of the fabricated devices, allowing the theoretical predictions to be experimentally validated. Chapter 5 addresses the practical electrical implementation of the resonator by developing an optimized capacitive transduction strategy together with a feedthrough compensation method for purely electrical actuation and detection. Finally, the manuscript concludes with a summary of the main contributions of this work and discusses perspectives for future developments.

1 - STATE OF ART OF HIGH-Q MEMS RESONATORS

1.1 . INTRODUCTION

Microelectromechanical systems (MEMS) resonators have attracted significant attention during the last three decades due to their wide range of applications in sensing [12, 13], signal processing [12, 5], timing references [12, 5], and communication systems [12, 3]. Owing to their small size, low power consumption, batch fabrication capability, and compatibility with integrated circuit technologies, silicon MEMS resonators are considered a promising alternative to conventional quartz crystal resonators in many applications.

A MEMS resonator is a mechanical structure designed to vibrate at one or several specific resonance frequencies [1]. Depending on the application, the resonator may operate as a sensing element or an embedded clock. Typical MEMS resonator geometries include cantilevers [4, 14], clamped-clamped beams [15], tuning forks [16], disks [8], rings [17], BAW (Bulk Acoustic Wave) [18] or SAW (Surface Acoustic Wave) resonators [19] and shell structures [9, 20]. Their resonant frequencies may range from a few kilohertz to several hundreds of megahertz depending on their dimensions, material properties, and vibration modes.

When combined with an electronic sustaining circuit, a MEMS resonator forms a MEMS oscillator. The oscillator converts the mechanical resonance into a stable electrical signal whose frequency is determined by the resonator. The overall performance of a MEMS oscillator is strongly influenced by the properties of the resonator, particularly its resonance frequency, quality factor, temperature stability, and long-term frequency stability.

Among the various performance parameters of a MEMS resonator, the quality factor is one of the most important ones with respect to frequency stability. It quantifies the ability of a resonator to store mechanical energy while minimizing energy dissipation during vibration. A high quality factor is generally associated with a narrow resonance bandwidth, a stronger resonant response, and improved device performance.

Since the quality factor is directly determined by the energy-loss mechanisms inside the resonator, considerable research efforts have been devoted to understanding and reducing these dissipation sources [21]. Over the last decades, numerous resonator structures have been proposed to achieve higher quality factors through improved energy confinement and reduced support losses [22, 23].

Consequently, the design of high-Q resonators has become a major research topic in the MEMS community. The following sections review the state of the art of high-Q MEMS resonators, the dominant dissipation mechanisms limiting their performance, and the principal design strategies that have been developed to increase the quality factor.

1.2 . HIGH-Q MEMS

The quality factor, commonly denoted by Q, is one of the most important figures of merit for mechanical resonators. For a resonator operating at angular frequency ω_0, the quality factor can be expressed as [6] :

$$Q = 2\pi \frac{E_{stored}}{E_{dissipated}} \tag{1.1}$$

where E_{stored} is the mechanical energy stored in the resonator and $E_{dissipated}$ is the energy lost during one oscillation cycle.

A high quality factor corresponds to low energy dissipation and therefore results in a narrow resonance linewidth. For a resonator operating at frequency f_0, the quality factor can also be expressed as :

$$Q = \frac{f_0}{\Delta f} \tag{1.2}$$

where Δf is the full width at half maximum (FWHM) of the resonance peak power(corresponding to the $\frac{1}{\sqrt{2}}$ of amplitude).

The interest in high-Q resonators originates from their direct impact on oscillator performance. According to the classical Leeson model, the phase noise of an oscillator decreases with increasing quality factor. Consequently, high-Q resonators generally exhibit improved frequency stability and lower close-to-carrier phase noise. These properties are particularly important for communication systems, precision sensors, inertial navigation devices, and timing references [5, 24].

The development of MEMS resonators has progressively pushed achievable quality factors from a few hundreds in early structures to several millions in state-of-the-art devices. Depending on the vibration mode and operating conditions, quality factors ranging from 10^3 to more than 10^7 have been reported in the literature [2].

Various resonator structures have been developed to achieve high quality factors. Flexural beam resonators generally exhibit moderate quality factors due to significant anchor losses and thermoelastic dissipation. Tuning fork resonators improve the quality factor by exploiting anti-phase motion and balanced reaction forces at the supports. Disk and ring resonators further increase quality factors by operating in contour or wine-glass modes, which naturally reduce energy leakage toward the anchors. More recently, shell resonators and hemispherical resonators have demonstrated exceptionally high quality factors exceeding one million owing to their highly symmetric vibration modes and reduced support losses.

In addition to the resonator geometry, the quality factor is strongly influenced by the surrounding environment. Operation under vacuum conditions suppresses gas damping and allows intrinsic dissipation mechanisms to dominate. Consequently, many high-performance MEMS resonators are packaged under vacuum to maximize their quality factors.

Although extremely high quality factors have been demonstrated in several MEMS structures, achieving microsystems with simultaneously low operating frequency, high quality factor, simple fabrication processes, and efficient electrostatic transduction remains challenging. This challenge motivates the investigation of resonator geometries capable of reducing energy dissipation while remaining compatible with conventional MEMS fabrication processes.

1.3 . ENERGY LOSSES SOURCES IN MEMS

The quality factor of a MEMS resonator is ultimately limited by the different mechanisms through which mechanical energy is dissipated during vibration. Understanding these dissipation mechanisms is essential for the design of high-performance resonators and for identifying the dominant limitations associated with a particular geometry, material, or operating environment [25, 26, 27].

In general, the total quality factor of a resonator can be expressed as the combination of several independent loss mechanisms :

$$\frac{1}{Q} = \frac{1}{Q_{air}} + \frac{1}{Q_{TED}} + \frac{1}{Q_{anchor}} + \frac{1}{Q_{others}} \tag{1.3}$$

where Q_{air} represents air damping (viscous and acoustic dissipation), Q_{TED} thermoelastic damping, Q_{anchor} anchor losses, and Q_{others} includes dissipation mechanisms such as material losses, surface losses, Akhiezer damping, and defect-related dissipation. Some papers also define the damping ratio ζ, related to the quality factor Q as [28] :

$$Q = \frac{1}{2\zeta} \tag{1.4}$$

allowing theoretical damping predictions to be directly compared with experimentally measured quality factors.

The relative importance of each contribution strongly depends on the resonator geometry, operating frequency, material properties, and environmental conditions. For resonators operating in atmospheric conditions, air damping is often the dominant source of energy dissipation. However, under vacuum conditions, intrinsic mechanisms such as thermoelastic damping and anchor losses generally determine the achievable quality factor.

For the resonators investigated in this thesis, which operate under vacuum conditions and are fabricated from single-crystal silicon, thermoelastic damping and anchor losses are expected to be the dominant mechanisms limiting the quality factor. Consequently, particular attention is devoted to these two contributions throughout this work. However, this section recalls some aspects of air damping that are relevant to the study presented in the manuscript.

1.3.1 . AIR DAMPING

Air damping originates from the interaction between the vibrating structure and the surrounding gas molecules. During oscillation, momentum is continuously exchanged between the resonator and the surrounding fluid, resulting in energy dissipation [14].

Several forms of air damping may occur depending on the resonator geometry. At small scales, for out-of-plane vibrating structures located near a substrate, squeeze-film damping is often dominant [29, 30, 31]. In this mechanism, the gas trapped between the resonator and the substrate is periodically compressed and expanded during vibration, generating viscous losses [32].As the ambient pressure decreases, the molecular mean free path increases, reducing the frequency of intermolecular collisions and weakening the interaction between the resonator and the surrounding gas. The molecular mean free path can be estimated as [28] :

$$\Lambda = \frac{\mu}{P}\sqrt{\frac{\pi k_B T}{2m_m}} \tag{1.5}$$

where μ is the gas viscosity, P is the ambient pressure, k_B is the Boltzmann constant, T is the absolute temperature, and m_m is the mass of a gas molecule.

The degree of gas rarefaction is characterized by the Knudsen number :

$$K_s = 1.016 \frac{\Lambda}{h} \tag{1.6}$$

where h is the characteristic air-gap thickness. According to Schaaf and Chambre, the free-molecular regime is generally reached when $K_s > 10$ [28].

In the free-molecular regime, the squeeze-film damping coefficient can be estimated using Bao's model [33] :

$$c_{\text{Bao}} = \frac{L_{\text{circ}}}{16\pi h} c_{\text{Christian}} \tag{1.7}$$

where L_{circ} is the circumference of the plate. The free-molecular damping coefficient proposed by Christian is :

$$c_{\text{Christian}} = 4A_p P \sqrt{\frac{2m_m}{\pi k_B T}} \tag{1.8}$$

where A_p is the plate area.

The corresponding squeeze-film-damping-limited quality factor is :

$$Q_{\text{SFD}} = \frac{m_{\text{eff}}\omega_n}{c_{\text{Bao}}} \tag{1.9}$$

which gives :

$$Q_{\text{SFD}} = \frac{2\pi^{3/2} m_{\text{eff}}\omega_n K_s h^2}{1.016 A L_{\text{circ}}\mu} \tag{1.10}$$

Assuming the MEMS resonator is a typical rectangular plate with dimensions $a = 250\mu m$ and $b = 300\mu m$, operating at frequencies in the range of several kilohertz and vibrating in air, Figure 1.1 shows the estimated results for squeezed-film damping. From the figure, the influence of air damping can be greatly reduced by operating the device under vacuum. As the pressure decreases, the mean free path of gas molecules increases and the interaction between the resonator and the surrounding gas becomes weaker. Consequently, the air damping coefficient decreases and the quality factor increases progressively until intrinsic dissipation mechanisms, such as thermoelastic damping, anchor loss, or material loss, become dominant. The pressure at which this transition occurs is strongly dependent on the resonator geometry, vibration mode, characteristic dimensions, and operating frequency, and therefore no universal threshold pressure can be defined [34, 28]. It can be expected that the plate will perform better when the gap is at least $1\mu m$ and the pressure is below $10^{-2}Pa$ or even below $10^{-4}Pa$ (at which point the effect of squeeze-film damping can be neglected and non-squeeze film damping dominate the dissipation).

For structures vibrating parallel to the substrate, slide-film damping may become significant [34, 35]. In addition, resonators operating in open environments are subjected to viscous damping caused by fluid drag arising from the relative motion between the vibrating structure and the surrounding fluid. As the resonator oscillates, it accelerates the adjacent fluid, generating viscous shear stresses and pressure disturbances around the structure. Part of the mechanical energy is therefore transferred to the fluid and dissipated through viscous friction, resulting in a reduction of the resonator quality factor. When no narrow fluid gap is present, the interaction between the vibrating structure and the surrounding unbounded fluid gives rise to external viscous damping (fluid drag) [36]. For this reason, high-performance MEMS resonators are generally characterized and operated under vacuum conditions.

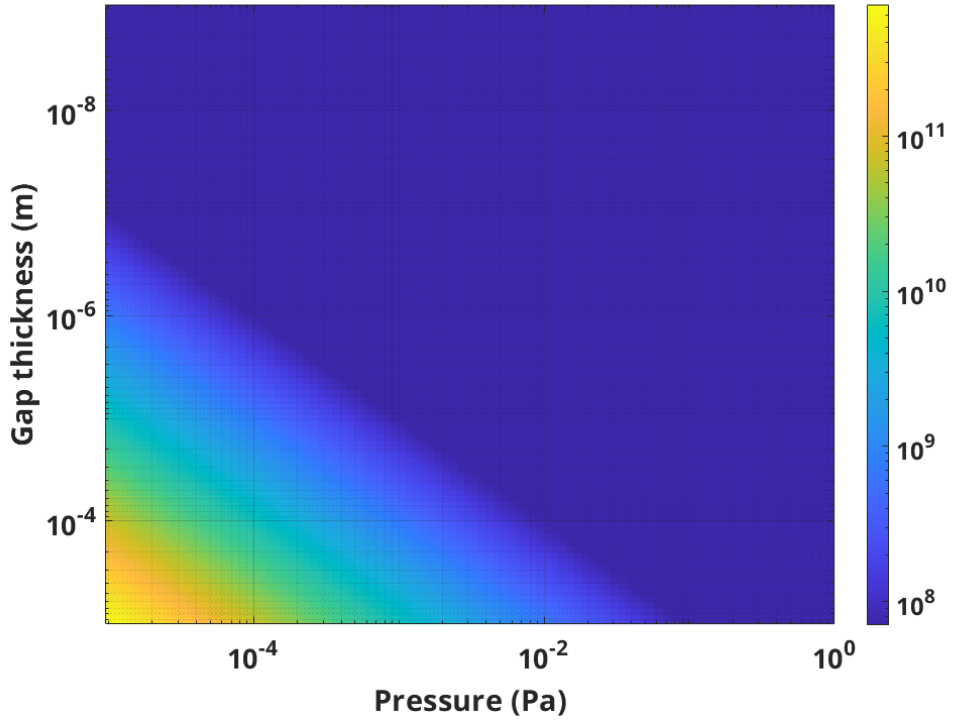

Figure 1.1 – Estimated evolution of Q_{SFD} with the thickness and air pressure of the plate gap.

1.3.2 . THERMOELASTIC DAMPING

Thermoelastic damping (TED) is one of the most important intrinsic dissipation mechanisms in MEMS resonators. It arises from the coupling between elastic deformation and heat transfer within the vibrating structure [37, 38, 39].

When a mechanical structure vibrates, some regions experience compression while others undergo tension. Due to the thermoelastic effect, compressed regions tend to increase in temperature whereas stretched regions experience a slight decrease in temperature. These temperature gradients induce heat flow inside the material. Since heat transfer is an irreversible process, part of the mechanical energy is converted into thermal energy during each oscillation cycle [40, 41].

The mechanism was first described by Zener for flexural vibrations and has since been extended to a large variety of resonator geometries. The magnitude of thermoelastic damping depends on the vibration frequency, the thermal diffusivity of the material, and the dimensions of the resonator [42].

Numerical simulation methods based on coupled thermo-mechanical finite element models are commonly used to estimate the TED-limited quality factor [43]. However some models propose a semi-quantitative analysis of the phenomenon for flexural plate mode resonators made of a uniform homogeneous isotrope material. The relative importance of thermoelastic damping (TED) can be evaluated using the classical Zener model [39] :

$$Q_{TED}^{-1} = \Delta \frac{\omega \tau_{TH}}{1 + (\omega \tau_{TH})^2} \tag{1.11}$$

where :

$$\Delta = \frac{E\alpha^2 T_0}{\rho C_p} \tag{1.12}$$

and :

$$\tau_{TH} = \frac{h_{diff}^2}{\pi^2 \chi}, \qquad \chi = \frac{\kappa}{\rho C_p} \tag{1.13}$$

Here, ω is the angular resonance frequency, τ_{TH} the thermal relaxation time, E denotes Young's modulus, α the thermal expansion coefficient, T_0 the absolute temperature, ρ the density, C_p the specific heat capacity, κ is thermal conductivity, χ the thermal diffusivity of the material, and h_{diff} the effective thermal path length, which is approximate to the thickness of the resonator for the case of a solid beam in flexure [39].

According to Equation (1.11), thermoelastic dissipation reaches its maximum when the oscillation frequency corresponds to the inverse of the thermal relaxation time :

$$\omega\tau = 1 \tag{1.14}$$

which corresponds to the minimum TED-limited quality factor (see Figure 1.2).

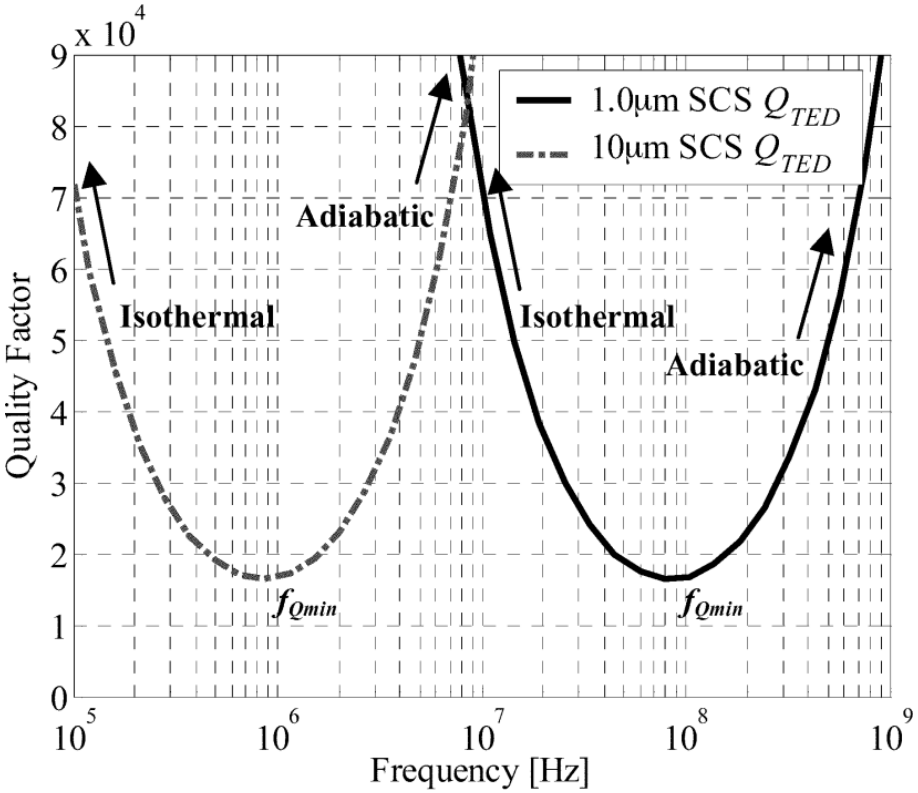

Figure 1.2 – Limit on resonator quality factor posed by thermoelastic dissipation for $1\mu m$- and $10\mu m$-wide single crystal silicon (SCS) beams [39].

The corresponding frequency can therefore be written as :

$$f_{TED,min} = \frac{1}{2\pi\tau_{TH}} = \frac{\pi\chi}{2h_{diff}^2} \tag{1.15}$$

An intuitive understanding of TED can be obtained by considering two limiting cases. When the vibration period is much longer than the thermal diffusion time, heat has sufficient time to flow and thermal equilibrium is nearly maintained throughout the structure. In this case, thermoelastic damping remains weak. Conversely, when the vibration period is much shorter than the thermal diffusion time, temperature gradients cannot relax efficiently and heat transfer is again limited. Maximum thermoelastic dissipation occurs when the mechanical oscillation period becomes comparable to the characteristic thermal relaxation time. For silicon MEMS resonators operating in the frequency range from several hundreds of kilohertz to a few megahertz, thermoelastic damping often establishes an important upper bound on the achievable quality factor.

For isotropic silicon, the maximum thermoelastic dissipation predicted by the Zener model occurs when $\omega\tau_{\mathrm{TH}} = 1$, yielding :

$$Q^{-1}_{TED,\max} = \frac{\Delta}{2} \tag{1.16}$$

or equivalently :

$$Q_{TED,\min} = \frac{2}{\Delta} \tag{1.17}$$

Using the room-temperature properties of single-crystal silicon ($E = 169$ GPa, $\alpha = 2.6\times10^{-6}$ K^{-1}, $\rho = 2330$ kg m^{-3}, $C_p = 700$ J kg^{-1}K^{-1}), the coupling factor is $\Delta \approx 2.1\times10^{-4}$, leading to $Q_{TED,\min} \approx 9.5\times10^{3}$. The corresponding frequency of maximum thermoelastic damping is $f_{TED,\min} = 1/(2\pi\tau_{TH})$, which is approximately 143 MHz for a 1-μm-thick silicon resonator and 1.43 MHz for a 10-μm-thick resonator.

The Zener expression provides a useful order-of-magnitude estimate, but it was originally derived for one-dimensional flexural motion with heat diffusion predominantly across the beam thickness. For a plate undergoing a complex vibration mode, the thermoelastic loss also depends on the spatial distribution of the modal curvature. In particular, the local thermoelastic source is related to the sum of the principal curvatures rather than directly to the displacement amplitude. Consequently, regions undergoing approximately anticlastic or saddle-shaped bending, for which the principal curvatures have opposite signs, generate significantly less thermoelastic loss than regions undergoing synclastic bending. Consequently, the thermal relaxation process is characterized by a single relaxation time τ_{TH}. This approximation is well suited for slender beams vibrating in their fundamental flexural mode, but becomes less accurate for resonators exhibiting complex plate modes.

For more complex plate modes, the thermoelastic dissipation depends on the complete distribution of the stress and curvature fields rather than on a single characteristic thermal relaxation time. Norris and Photiadis extended the classical Zener theory to arbitrary thin-plate vibration and demonstrated that the thermoelastic loss is governed by the modal curvature field and the associated thermoelastic energy distribution over the entire structure rather than solely by the vibration amplitude or local displacement [44]. Consequently, the beam-based Zener model should be regarded as an order-of-magnitude approximation for complex plate resonators. For an isotropic thin plate, this mode-shape dependence can be approximately included through a modal participation factor (p_m), such that [44] :

$$Q_{\mathrm{TED},m}^{-1} \simeq p_m Q_{\mathrm{Zener}}^{-1} \tag{1.18}$$

For plate resonators, the strain field generally varies in both in-plane directions and may include multiple regions of opposite curvature separated by nodal lines. The resulting temperature field therefore cannot be described by a one-dimensional diffusion process. Instead, thermoelastic damping is governed by the fully coupled thermo-mechanical equations, in which heat conduction occurs simultaneously in multiple directions. Consequently, several thermal relaxation modes may contribute to the energy dissipation, rather than a single characteristic relaxation time.

For this reason, finite-element thermoelastic simulations generally provide more accurate predictions for complex plate modes than the analytical Zener model. The FEM approach directly solves the coupled thermo-mechanical field over the complete resonator geometry, accounting for the actual strain distribution, multidimensional heat diffusion, and local stress concentrations. Therefore, the analytical model presented here should be regarded as a first-order estimation of the thermoelastic damping, while the quantitative values reported in this work are obtained from the finite-element simulations.

1.3.3 . ANCHOR LOSSES

Anchor losses correspond to the dissipation of mechanical energy through the supports connecting the resonator to the substrate [45, 46].

Unlike thermoelastic damping, which is an intrinsic material phenomenon, anchor losses are directly related to the resonator geometry and support configuration [47, 48]. During vibration, elastic waves generated inside the resonator can propagate through the anchor region and radiate into the substrate. Since the substrate behaves as a practically infinite mechanical domain, the transmitted energy is not recovered and is effectively lost from the resonator [49].

Anchor losses are often the dominant limitation in high-Q MEMS resonators operating under vacuum conditions. As other dissipation mechanisms are progressively reduced through improved materials and fabrication techniques, support losses increasingly determine the maximum achievable quality factor [50].

Anchor losses have been described using several complementary approaches, including elastic-wave radiation models for simple beam–support junctions [51] and phonon-tunnelling models for micro- and nanomechanical resonators [49]. Anchor losses originate from the radiation of elastic waves from the resonator into the supporting substrate and are therefore strongly dependent on both the resonator mode shape and the support geometry. Within this framework, the resonator is regarded as a localized elastic cavity weakly coupled to the continuum of substrate modes through the contact area S. Under the weak-coupling assumption ($k_R d \ll 1$, where d is the characteristic contact dimension and k_R^{-1} is the characteristic length scale over which the resonator mode varies appreciably, the support-limited dissipation can be expressed as [49] :

$$\frac{1}{Q_{anchor}} = \frac{\pi}{2\rho_s \rho_R \omega_R^3} \int_q \left| \int_S \left(\sigma_q^{(0)} \cdot \mathbf{u}_R' - \sigma_R' \cdot \mathbf{u}_q^{(0)} \right) \cdot \mathrm{d}\mathbf{S} \right|^2 \delta[\omega_R - \omega(q)] \tag{1.19}$$

where $\mathbf{u}_R'$ and σ_R' denote the displacement and stress fields of the resonator mode, $\mathbf{u}_q^{(0)}$ and $\sigma_q^{(0)}$ are the corresponding substrate eigenmodes, ρ_R and ρ_s are the material den-

sities of the resonator and substrate, respectively, and the surface integral is evaluated over the contact area between the resonator and its support [49].

Equation (1.19) provides direct physical insight into the design of low-loss resonators. Since the coupling is determined by the overlap between the resonator mode and the substrate modes over the contact area, several optimization strategies naturally emerge. First, placing the anchors at nodal points or nodal lines minimizes the resonator displacement $\mathbf{u}'_R$ at the support, thereby reducing the overlap integral and suppressing elastic-wave radiation. This principle has been widely adopted in wine-glass, ring, disk and plate resonators. Second, reducing the contact area or introducing narrow tethers decreases the coupling region S, thereby reducing the energy transferred into the substrate. Third, impedance-mismatched supports or quarter-wavelength tethers modify the substrate displacement field $\mathbf{u}_q^{(0)}$ through partial reflection of elastic waves, leading to a lower overlap with the resonator mode. Finally, phononic-crystal supports suppress the density of propagating substrate modes around the resonance frequency, thereby reducing the number of available energy leakage channels [52].

Although the phonon-tunnelling model provides a unified physical interpretation of most anchor-loss reduction strategies, it relies on the weak-coupling assumption and requires the support dimensions to remain small compared with the characteristic wavelength of the resonator mode. Moreover, the prediction accuracy depends on the representation of the support modes and idealized boundary conditions. Consequently, practical evaluation of anchor loss in complex MEMS structures is now commonly performed using finite-element simulations combined with absorbing boundaries or perfectly matched layers (PMLs) [53, 54], while the phonon-tunnelling model remains an essential theoretical framework for understanding the physical origin of support loss and guiding resonator design.

The bell plate structures investigated in this thesis follow the same philosophy of nodal anchoring. The amount of energy radiated through the supports strongly depends on the vibration mode shape. Modes exhibiting large displacements near the anchors generally suffer from significant support losses. Conversely, modes possessing nodal points or nodal lines near the support region can substantially reduce energy leakage. By appropriately tuning the geometric parameters of the resonator, the nodal line associated with the target vibration mode can be positioned close to the clamped region, thereby reducing anchor losses and increasing the quality factor.

1.3.4 . OTHER DISSIPATION MECHANISMS

In addition to air damping, thermoelastic dissipation, and anchor losses, several other dissipation mechanisms may contribute to the overall energy loss of MEMS resonators [55].

Surface losses originate from defects, contamination, oxidation layers, and atomic-scale imperfections located near the surface of the structure [56]. Since MEMS devices possess large surface-to-volume ratios, surface-related dissipation may become significant, particularly for nanoscale resonators [57].

Material losses arise from crystal defects, impurities, dislocations, and other internal friction mechanisms [6]. Although single-crystal silicon exhibits exceptionally low internal friction, material losses may still contribute under certain operating conditions.

When the vibration frequency becomes comparable to the inverse phonon relaxation

time, thermoelastic damping gradually gives way to Akhiezer damping as the dominant phonon-related dissipation mechanism. Unlike thermoelastic damping, which is associated with macroscopic heat flow, Akhiezer damping originates from the interaction between the oscillating strain field and the thermal phonon population within the crystal. The periodic strain perturbs the equilibrium phonon distribution, and the subsequent phonon relaxation towards thermal equilibrium dissipates mechanical energy. The strength of this mechanism is governed by the dimensionless parameter $\omega\tau$, where ω is the angular resonance frequency and τ is the phonon relaxation time. Akhiezer damping is most significant when $\omega\tau \approx 1$, whereas for $\omega\tau \ll 1$ and $\omega\tau \gg 1$ the dissipation decreases [58]. This mechanism originates from the interaction between the strain field generated by the vibration and the thermal phonon population inside the material.[58] The resulting redistribution of phonons leads to irreversible energy dissipation.

Finally, fabrication-induced imperfections, residual stresses, and electrical dissipation associated with transduction mechanisms may also contribute to the overall quality factor. The relative importance of these effects depends on the specific resonator design and operating conditions.

For the resonators investigated in this work, the relative importance of the various dissipation mechanisms can be estimated from the operating conditions and the characteristic quality factors reported in the literature. The devices operate under high vacuum, rendering air damping negligible. Their characteristic dimensions are several micrometres, substantially reducing the influence of surface-related dissipation compared with nanoscale resonators. Moreover, the resonant frequencies are around several hundred kilohertz, corresponding to $\omega\tau \ll 1$ for silicon at room temperature, such that Akhiezer damping is not expected to be a dominant intrinsic loss mechanism. Material dissipation in single-crystal silicon generally remains low and is influenced by factors such as crystal quality, impurity concentration, defect density, residual fabrication damage, and potentially the doping level. Table 1.1 summaries the loss sources with typical limitation. Consequently, for the devices considered in this work, thermoelastic damping and anchor loss are expected to constitute the principal intrinsic dissipation mechanisms limiting the quality factor, while the remaining mechanisms mainly provide secondary contributions.

Loss mechanism	**Typical limit**
Air damping [28]	$Q > 10^8$ (in vacuum)
Thermoelastic damping [59, 42]	$Q \sim 10^4$–10^7
Anchor loss [51, 49]	$Q \sim 10^3$–10^7
Material loss [6]	Device dependent; typically not limiting in single-crystal silicon.
Surface loss [56, 57]	Typically $Q > 10^6$ for micrometre-scale resonators.
Akhiezer damping [58]	$fQ \sim 10^{13}\,\mathrm{Hz}$ at room temperature.

Table 1.1 – Representative quality-factor limits associated with the main dissipation mechanisms in room-temperature silicon MEMS resonators.

1.4 . CLASSIFICATION AND DESIGN STRATEGIES OF HIGH-Q MEMS RESONA-

TORS

MEMS resonators can be broadly classified according to their dominant vibration mode into flexural resonators, bulk acoustic wave (BAW) resonators, surface acoustic wave (SAW) resonators and shell resonators [60]. Different MEMS resonator families have been developed to address different frequency ranges and application requirements.

Flexural resonators include cantilevers, tuning forks, ring resonators and plate resonators, for example in Figure 1.4 and 1.3. They generally operate from several kilohertz to a few megahertz and are widely used in sensing applications because of their relatively large vibration amplitudes and compatibility with electrostatic transduction [4]. However, their measured quality factors are often limited by air damping, support loss, surface loss, or thermoelastic damping, depending on geometry, pressure and material properties [61]. Their Q-factor rang widely–from 10^3 to 10^5–depending on the operating conditions and requirements. Overall, flexural resonators offer broad application potential due to their high design flexibility, particularly in the field of sensors.

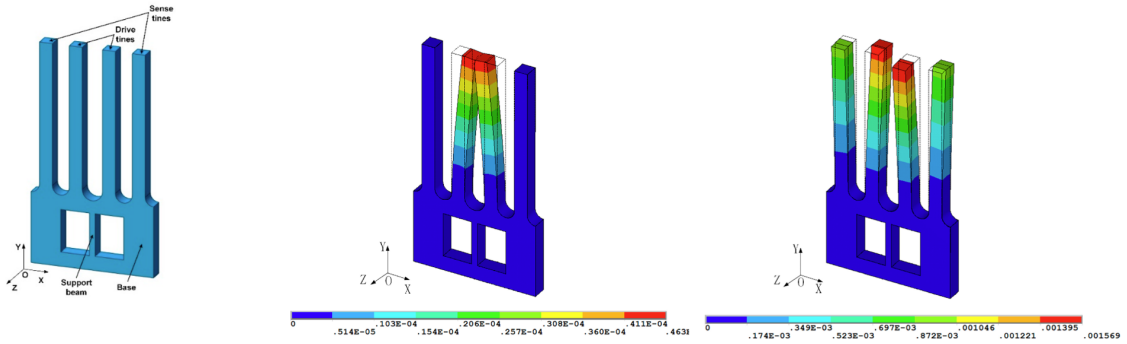

Figure 1.3 – (a) Structure of decoupling MEMS tuning fork gyroscope, (b) Driving mode, (c) Sensing mode [16].

In contrast, bulk acoustic wave (BAW) resonators employ longitudinal or extensional modes propagating through the device volume (see Figure 1.5) [62]. And Surface acoustic wave (SAW) resonators utilize acoustic waves travelling along the substrate surface (a example see Figure 1.6) and The vibration mode shape is depicted in Figure 1.7. Owing to their high stiffness, they usually operate from several tens of megahertz to the gigahertz range while maintaining excellent frequency stability and high quality factors up to 10^6. They typically operate from tens of MHz to several GHz and can achieve excellent frequency stability and high fQ products, making them particularly suitable for radio-frequency (RF) filtering and timing applications [63, 19]. However, reducing their frequency to the sub-MHz range would require acoustic wavelengths, and therefore device dimensions, in the millimetre-to-centimetre range, which is incompatible with compact MEMS integration.

Phononic-crystal (PnC) resonators use periodically patterned structures (see Figure 1.8) to create frequency bandgaps in which elastic-wave propagation is forbidden [65, 66, 67]. When a localized resonant mode lies inside such a bandgap, its mechanical energy is confined and radiation towards the substrate is suppressed, thereby reducing anchor

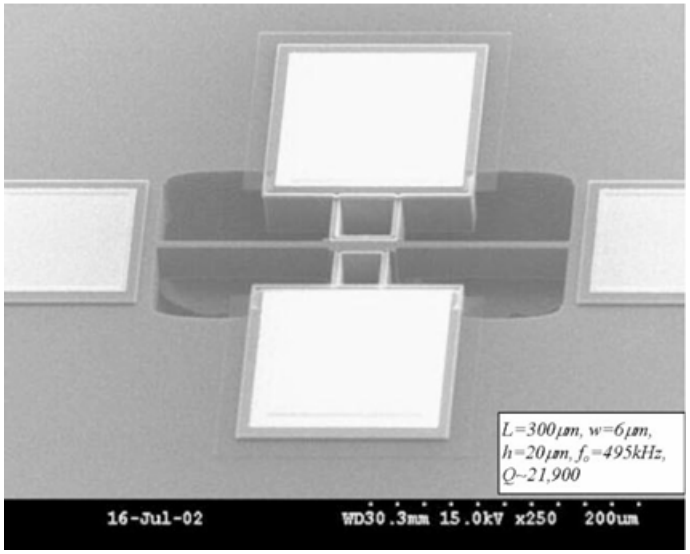

Figure 1.4 – SEM view of a clamped–clamped single crystal silicon beam resonators fabricated through the HARPSS process [61].

loss [52]. Reported quality factors range from approximately 10^4 for conventional PnC resonators to nearly 10^9 for soft-clamped, stress-diluted structures, with the performance depending on the material, unit-cell geometry, defect design, and operating conditions [52]. This approach has enabled very high quality factors in both silicon MEMS and soft-clamped nanomechanical resonators [68]. Its main limitations are the additional device area and the accurate fabrication required for the periodic structure.

Shell resonators constitute another important family of high-Q MEMS resonators (see Figure 1.9). Their nearly symmetric three-dimensional geometry confines vibration energy efficiently and reduces support loss by placing the stem close to a nodal region of the wine-glass mode, allowing quality factors exceeding one million. Hemispherical resonator gyroscopes based on fused silica shells can reach quality factors exceeding 10^7 in vacuum, but they generally require complex three-dimensional fabrication, trimming and balancing processes [69].

Despite the diversity of resonator geometries, the fundamental objective remains the same : minimizing mechanical energy dissipation to maximize the quality factor. Existing high-Q resonators mainly achieve this objective through force balancing, nodal anchoring, symmetry-based energy confinement or elastic-wave isolation [70].

Table 1.2 summarizes the main characteristics of representative MEMS resonator structures. Cantilever resonators are among the simplest and most widely studied MEMS resonator architectures, whereas other resonators generally achieve higher quality factors through different ways. The other devices in the table are true high-Q resonators, each offering unique advantages.

1.4.1 . POSITIONING OF BELL PLATE RESONATOR WITHIN THE STATE-OR-ART

Among these structures, the bell-plate resonator investigated in this thesis occupies an intermediate position between conventional balanced flexural resonators and more elaborate wave-confinement structures. Its operating principle is most closely related to those of tuning-fork and ring or disk resonators which reduce anchor loss through modal

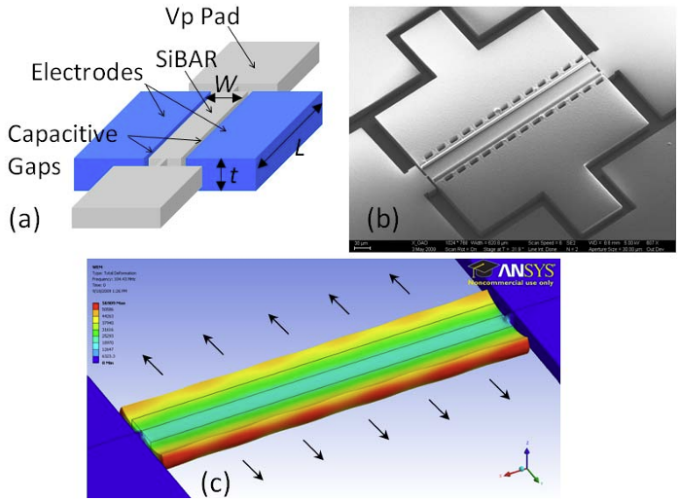

Figure 1.5 – (a) Structure, (b) SEM view, and (c) simulated width-extensional mode shape of the Silicon Bulk Acoustic resonator (SiBAR) device in ANSYS (t=10 µm) [19].

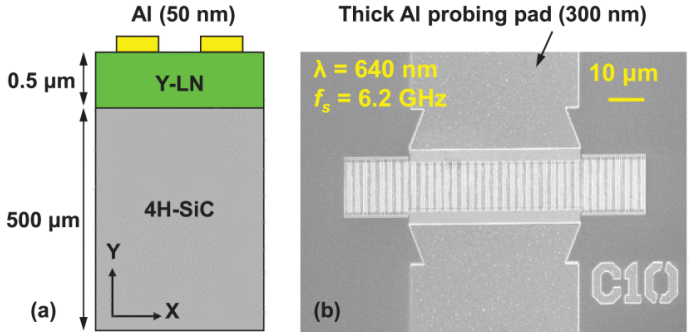

Figure 1.6 – (a) Unit cell model of the resonator based on LN/SiC. (b) SEM image of the C-band SH-SAW resonator proposed in this study [64].

engineering. The principal distinction is that the bell plate does not require two dynamically matched resonating elements, as in a tuning fork, nor complex geometric structure like three-dimensional shell resonators. It retains a simple planar geometry compatible with conventional MEMS fabrication (lithography, silicon etching, metallization, and release steps) while naturally operating in the low-frequency range. Its relatively large out-of-plane displacement also facilitates optical characterization and gap-closing electrostatic transduction, which requires low voltage supply.

This thesis focuses on high-Q MEMS resonators operating below $1\ MHz$, a frequency range relevant for many sensing applications where large displacement amplitude and simple readout are desirable, and for low-power timing systems where direct low-frequency operation can reduce the need for frequency division or complex PLL architectures. These features make them a promising candidate for high-Q low-frequency MEMS resonators.

1.5 . STATE OF THE ART OF BELL PLATE

Bells are one of the most oldest musical instruments in the world, probably older than the recorded history. They are wildly used in daily life, such as alarms and tocsins

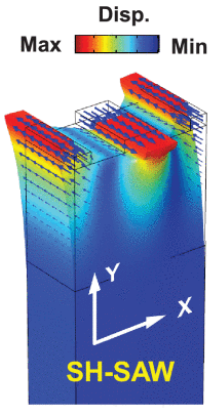

Figure 1.7 – Simulated mode shape of the SH-SAW resonator [19].

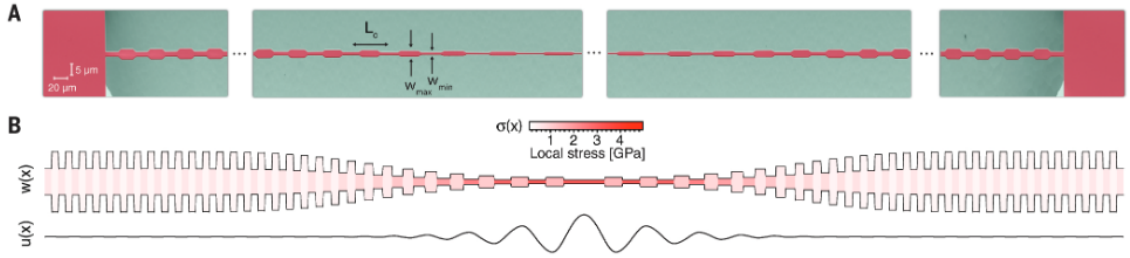

Figure 1.8 – Strain-engineered 1D phononic crystals. (A) Scanning electron microscopy (SEM) image of a tapered PnC nanobeam, vertically scaled for perspective. (B) Width/stress profile and defect mode shape of a device with 60 unit cells [67].

(see Figure 1.10). A defining feature of bells is their ability to produce stable and long, sustained resonant tones after striking on their surface, which is the manifestation of their high-quality factors [77]. This characteristic has made them a common musical instrument across civilizations of diverse origins and also makes bell-shaped structures potential candidates for high-Q resonators. The most common type of clock features a 3D structure like tocsin. Other scientists have also constructed resonators for such bells, for example in [78] a micro-bell resonator presented by Tal Nagourney *et al.* (see Figure 1.11), achieving exceptionally high quality factors. However, the manufacturing process for this structure is highly challenging and subject to material constraints, requiring the use of fused silica.

In recent year, a new type of bells is discovered which is bell plate. The structure of this bell consists of a plate of uniform thickness. Like bells of other designs, these bell plate have the same characteristic in producing pleasant sound and they are used in orchestra as well [11]. Bell plates typically come in two standard shapes : rectangular and trapezoidal (see Figure 1.12).

The trapezoidal bell plate is a unconventional shape. Compared to the triangle plates which have been investigated during long time, the advantage is the unconventional shape could make the position of nodal line of one specific mode close to the edge of shape under free-free boundary condition to increase the Q-factor, whereas the nodal lines of all modes of triangle plate never have this property (see Figure 1.13 [79]). Due to this property, we focused on the trapezoidal ones because they are more suitable for standard MEMS fabrication process.

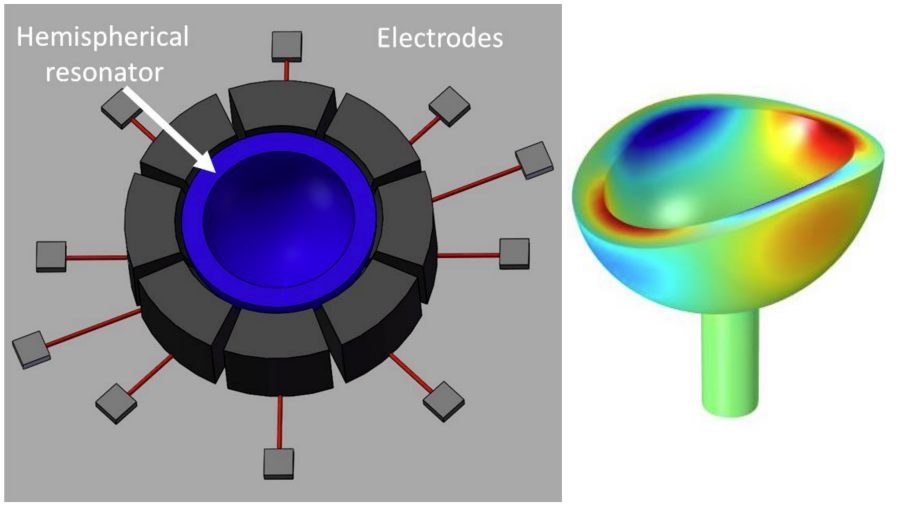

Figure 1.9 – (a) Hemispherical shell , (b) Second mode of vibration (n = 2) of a wineglass (hemisphere)-shaped resonator [69].



Figure 1.10 – A ringing tocsin of a church (Photo from internet).

Macroscopic bell plates were qualitatively analyzed by Lavin *et al.* [10]. This work indicated the high dependence of the produced sound with the bell plate geometry and evidenced the (2,0)-mode is the key mode of high-Q performance. They validated the advantage of bell plate by Chladni patterns (see Figure 1.14). The evolution indicated the mode shape of the ringing mode and they named the mode as (2,0)-mode according to the pattern of nodal line. In the next section, I will introduce the first quantitative characterization of macroscopic trapezoidal bell plate I did as the beginning of my work.

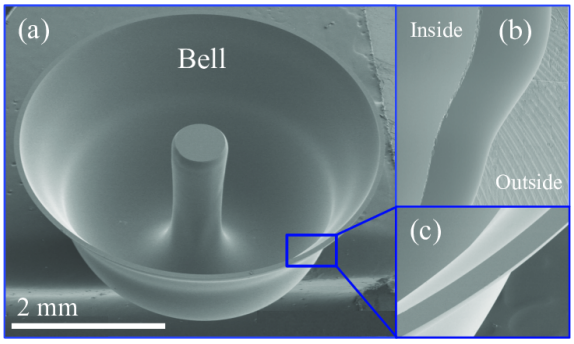

Figure 1.11 – Scanning electron micrographs of the bell resonator [78].



Figure 1.12 – Commercial bell plate musical instrument. Left : rectangular bell plate © Acolyte Instruments. Right : trapezoidal bell plate © Belleplates.

1.6 . ANALYSIS OF BELL PLATE DISSIPATION SOURCE

In this section, the dissipation mechanisms of the bell plate resonator are analysed according to Equation (1.3). The contribution of air damping is minimized by operating the device under vacuum conditions and, in future implementations, by packaging the device under very low pressure. The term Q_{others} is neglected because its contribution is generally smaller than those associated with thermoelastic damping and anchor losses. In most MEMS resonators, Q_{others} is not expected to be the dominant loss mechanism.

As discussed in the previous section, the ability to reduce anchor losses is one of the main advantages of the bell plate geometry and constitutes the primary motivation of the present work. Bell plate resonators are especially attractive in this context. The target (2,0)-ringing-mode exhibits a U-shaped nodal line whose position can be continuously tuned through geometric parameters such as the plate dimensions and extension length. By bringing this nodal line closer to the clamped region, the vibration amplitude at the support can be significantly reduced, thereby decreasing the amount of elastic energy radiated into the substrate.

TED is the dominant dissipation mechanism apart from anchor loss in this work. However, no additional design optimization is introduced to improve (Q_{TED}), because, for

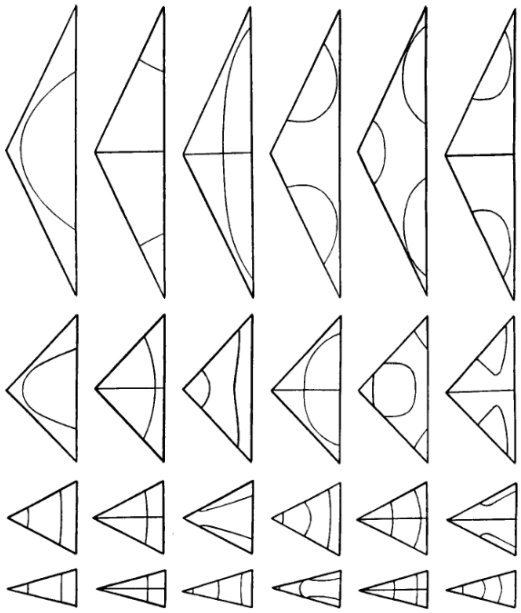

Figure 1.13 – Nodal patterns for isosceles triangular plates with same triangle height and different ratio of height to length [79].

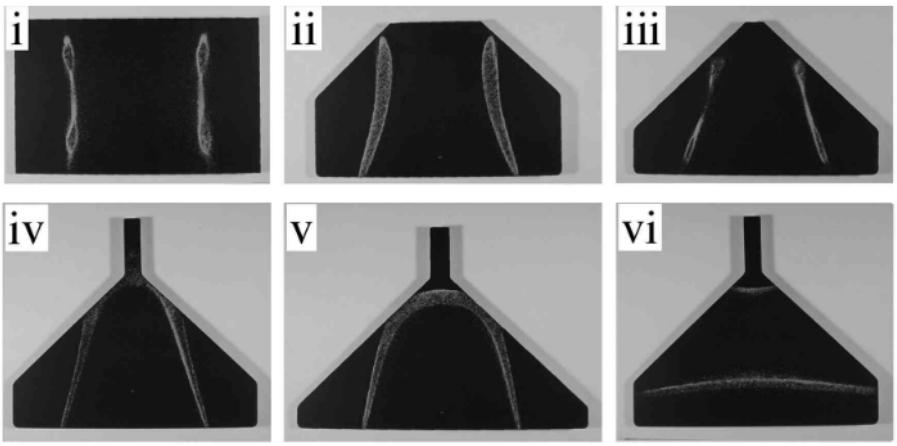

Figure 1.14 – Evolution of Chladni patterns of bell plate. (iv) is the ringing mode of bell plate (called (2,0)-mode) when the bell plated designed properly [10].

all MEMS bell-plate samples characterized in this work, the predicted (Q_{TED}) is several orders of magnitude higher than both the Q_{anchor} obtained from FEM simulations and the experimentally measured Q. Further details are provided in Chapter 3.

Consequently, although thermoelastic damping establishes an intrinsic upper limit for the achievable quality factor, the bell plate geometry provides a direct and efficient means of controlling anchor losses. For this reason, the present work focuses primarily on anchor-loss reduction through nodal-line engineering, with the objective of progressively approaching the intrinsic dissipation limit imposed by thermoelastic damping.

1.7 . CONCLUSION

This chapter reviewed the state-of-art of high-Q MEMS resonators and the principal mechanisms governing their performance. The concepts of resonance, quality factor, and frequency stability were first introduced, highlighting the critical role of mechanical energy dissipation in determining the performance of MEMS oscillators. High-Q resonators are essential for achieving low phase noise and high frequency stability, making the reduction of dissipation mechanisms a central objective in MEMS resonator design.

The main energy-loss mechanisms encountered in MEMS resonators were subsequently discussed, including air damping, thermoelastic damping, anchor losses, and other intrinsic or extrinsic dissipation processes. For vacuum-operated silicon resonators, thermoelastic damping and anchor losses were identified as the dominant contributions. While thermoelastic damping establishes an intrinsic upper bound on the achievable quality factor, anchor losses remain strongly dependent on the resonator geometry and support configuration.

A review of existing high-Q MEMS resonator structures demonstrated that most successful approaches rely on reducing anchor losses through modal engineering. Although these structures exhibit excellent performance, they often involve complex geometries, large footprints, or demanding fabrication processes.

Within this context, bell plate resonators represent an attractive alternative for low-frequency MEMS applications. Their distinctive feature lies in the presence of a controllable nodal line associated with the target ringing mode. By appropriately adjusting the geometric parameters of the resonator, this nodal line can be positioned close to the support region, thereby reducing the transmission of elastic energy into the substrate and lowering anchor losses. Unlike many existing high-Q resonator structures, this approach can be implemented while maintaining a relatively simple planar geometry compatible with conventional MEMS fabrication technologies.

An analysis of the dissipation mechanisms specific to bell plate resonators further showed that the operating frequencies considered in this work remain below the frequencies corresponding to maximum thermoelastic dissipation. Combined with finite-element simulations predicting TED-limited quality factors significantly higher than the experimentally measured values, this observation suggests that thermoelastic damping is not the dominant limitation in the investigated devices. Instead, anchor losses are expected to play a major role in determining the overall quality factor.

Consequently, the remainder of this thesis focuses on the reduction of anchor losses through geometric optimization of bell plate resonators. Particular attention is devoted to the relationship between resonator geometry, nodal-line position, and quality factor. To establish this relationship, the next chapter first investigates the dynamic behaviour of macroscopic bell plates, providing experimental and numerical insights into the mechanisms responsible for their high-Q performance before transferring these concepts to MEMS-scale resonators.

Resonator type	Frequency	Q	Main observed losses	High-Q principle	Applications
Cantilever [4, 61]	kHz–MHz	10^3˘10^5	TED, anchor		Sensing, AFM
Tuning fork [16, 7]	kHz–MHz	10^4˘10^6	Anchor, TED	Force balance	Sensing, timing
Ring / disk [71, 8, 72]	MHz–GHz	10^4˘10^6	Anchor loss, TED	Nodal anchoring	Timing, sensing
BAW[73, 64, 74]	MHz–GHz	10^4˘10^6	Material, electrode, anchor	Energy confinement	RF filters, timing
SAW [75, 63, 19]	GHz	10^2˘10^4	Material, electrode, leakage	Surface-wave confinement	RF filters, sensing
PnC [67, 68]	kHz–GHz	10^4–10^9	Material, surface, TED	Phononic bandgap	Sensing, optomechanics, RF
Shell [76, 69]	kHz–MHz	10^6-10^7	Material, surface, anchor	Nodal support	Sensing
Bell Plate (this work)	kHz–MHz	$> 10^5$	Anchor, TED	Nodal line	Sensing, timing (Possible)

Resonator type	Typical dimensions	Typical excitation voltage
Cantilever	100–500 μm	1–20 V
Tuning fork	100–1000 μm	5–30 V
Ring / disk	10–100 μm	5–30 V
BAW	50–1000 μm	5–50 V
SAW	0.5–10 μm	0.02–0.2 V
PnC	100 μm–10 mm	Transduction dependent
Shell	0.5–10 mm	5–50 V
Bell plate (this work)	$500\mu m$	$1–10V$

Table 1.2 – Comparison of MEMS resonator families and dominant dissipation mechanisms.

2 - PRELIMINARY STUDY ON MACROSCOPIC BELL PLATE

2.1 . INTRODUCTION

In Chapter 1, we introduced a novel high-Q musical instrument reported as "bell plate". Before the study of microscopic bell plates, a preliminary study on centimeter-scale bell plates, easier to fabricate, would provide interesting insights for the optimal design of MEMS bell plate resonators.

This section presents the design, modeling, and experimental characterization of macroscopic bell plates, which serve as a test platform for validating the proposed high-Q resonator concept. The objective is to establish a clear relationship between geometric parameters, vibration modes and energy dissipation mechanisms, with a particular focus on minimizing anchor losses.

In section 2.2, the overall geometry of bell plates is introduced, highlighting the role of the tang and its influence on boundary conditions. The first four modes of the plates are simulated by finite element method (FEM). Then, a theoretical model of the plate is developed to analyze the natural frequencies of the dominant vibration modes, namely the first bending mode and the (2,0)-mode. Special attention is given to the dependence of these modes on geometric parameters.

Next, in section 2.4, based on FEM simulations, macroscopic prototypes are fabricated and characterized from experimental ring-down and frequency response measurements. The results are compared to simulations to validate the model.

2.2 . OVERALL DESIGN

Figure 2.1 illustrates the geometry of a trapezoidal bell plate, with key segments and parameters labeled to facilitate description and understanding in the following sections. When used as musical instruments [10], bell plates are traditionally clamped at the end of the so-called "tang".

2.3 . MODELING OF MACROSCOPIC BELL PLATES

An example of bell plate geometric parameters is given in Table 2.1. In this section, the influence of geometric dimensions is analyzed based on theoretical considerations supported by FEM simulations (via COMSOL Multiphysics). The plate length L_{tot} is constrained by five parameters. Equation (2.1) provides the geometrical relationship between the length of the tang L_t, the length of the triangle-like part L, the length of the edge L_e, the width of the plate W and the width of the tang W_t.

$$L_{tot} = L_t + L + L_e - W_t \frac{L}{W} \tag{2.1}$$

2.3.1 . OBSERVATIONS ON THE FIRST VIBRATION MODES OF A BELL PLATES

Like any other clamped-free beam or plate, bell plates eigenmodes include several bending modes. Four mode shapes are illustrated in Figure 2.2. Among all interesting

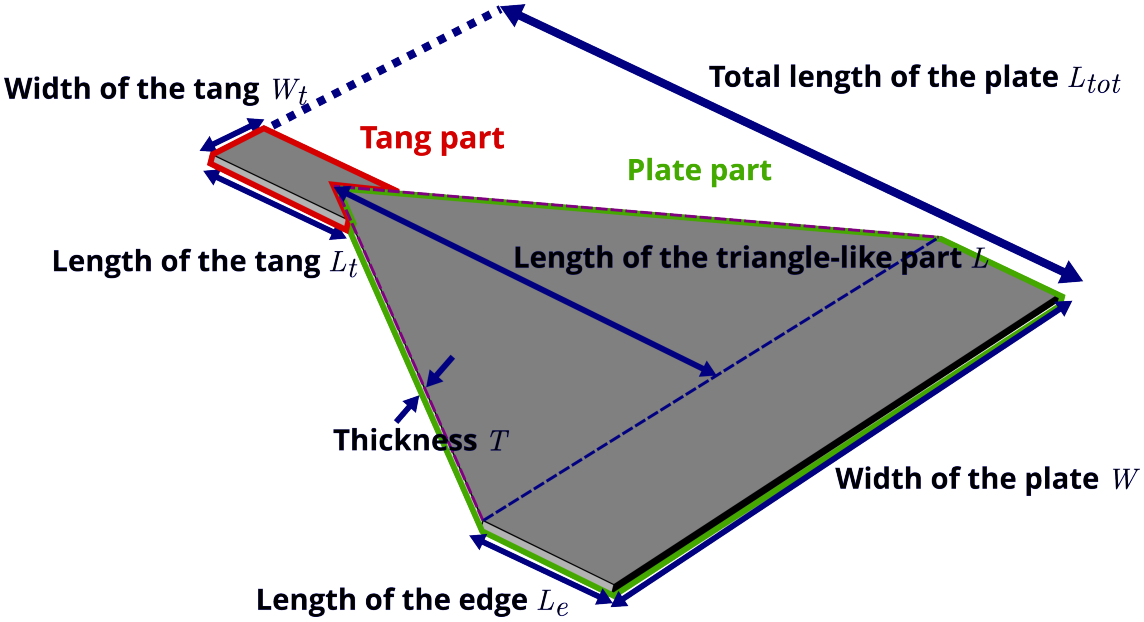

Figure 2.1 – Schematic of the bell plate.

T	W_t	L_t	W	L	L_e
1	16	10	100	50	18

Table 2.1 – Dimensions (in mm) of a macroscopic bell plate example. L_{tot} is $70\ mm$ (see 2.1).

bending modes that can be expected from such a plate [10], the (2,0)-mode is depicted in Figure 2.2(d). In some cases, the order of these four modes may vary. In particular, the frequency of the (2,0)-mode may be lower than that of the (0,1)-mode depending on the dimensions.

The next paragraph provides a specific analysis of the (2,0)-mode based on FEM simulation. Since the experiments on macroscopic plate will be performed with stainless steel (see subsection 2.4), we assume an isotropic material with a Young's modulus of approximately 2×10^2 GPa and a Poisson's ratio of 0.3 [80].

SPECIFIC FOCUS ON THE (2,0)-MODE NATURAL FREQUENCY

For all the considered bell plates, the width of the tang W_t is much smaller than the width of the plate W (typically more than 5 times). In addition, based on [10], high-Q bell plates exhibit almost no deformation of the tang part when ringing in the (2,0)-mode. Under these assumptions, the natural frequency of the (2,0)-mode is easier to analyze compared to the first bending mode because it is highly and almost solely dependent on the plate part (see Figure 2.1). The plate part can be approximated as a deformed isosceles triangular plate combined with an edge part. Therefore, assuming a uniform isotropic material, the natural frequency of the (2,0)-mode should follow Equation (2.2) [79], where $\lambda(\frac{W}{L})$ is the eigenvalue λ depends on the variable $\frac{W}{L}$, E the Young's modulus of

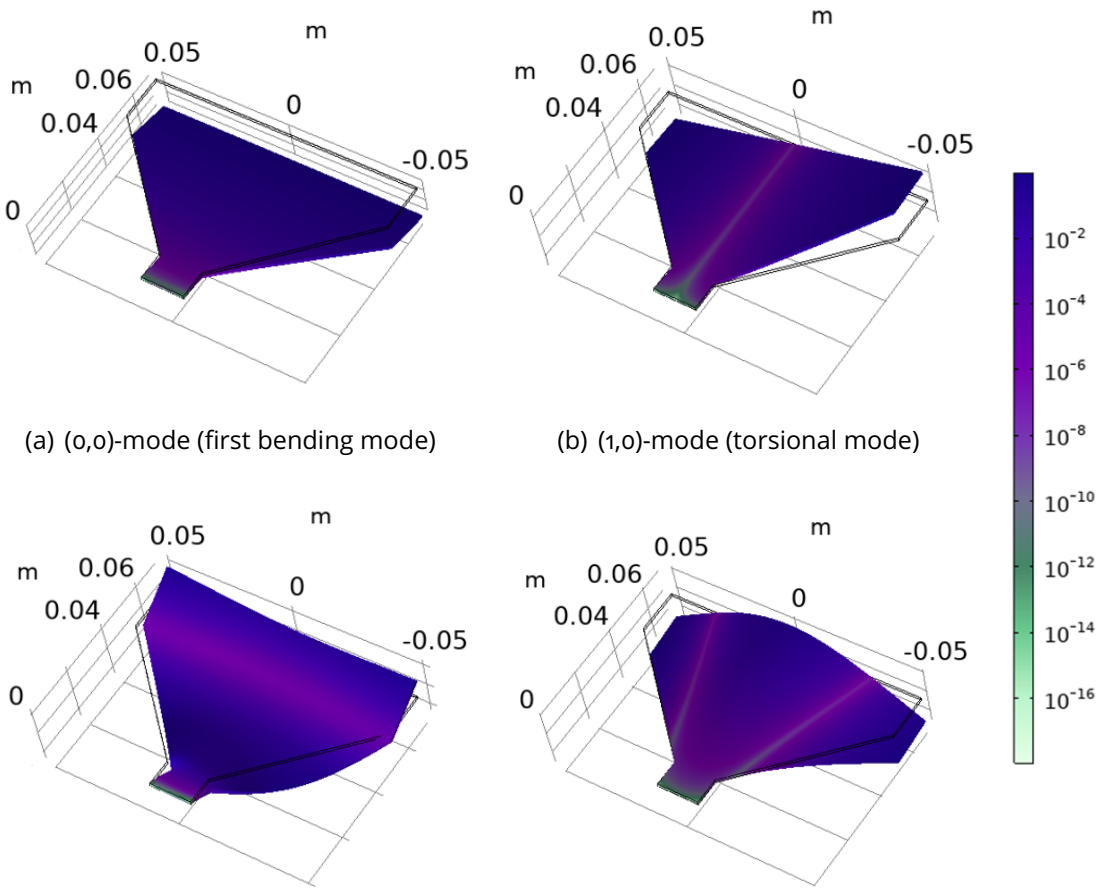

(a) (0,0)-mode (first bending mode)

(b) (1,0)-mode (torsional mode)

(c) (0,1)-mode

(d) (2,0)-mode

Figure 2.2 – Mode shapes of the first four modes under clamped-free condition (clamped on the edge of the tang) for the design of Table 2.1.

the material, ρ the density and ν the Poisson ratio.

$$f = \frac{\lambda(\frac{W}{L})T}{4\sqrt{3}\pi L^2}\sqrt{\frac{E}{\rho(1-\nu^2)}} \tag{2.2}$$

The ratio $\frac{W}{L}$ determines λ, which governs the natural frequency. Since there is no explicit expression of $\lambda(\frac{W}{L})$, its value is obtained from FEM simulations for specific values of the ratio $\frac{W}{L}$. Hence, FEM simulations are performed for a plate with $W = 100mm$, $T = 1mm$ and $L = 50mm$. From these numerical simulations, Figure 2.3 allows to extract $\lambda(\frac{W}{L})$, as summarized in Table 2.2. other geometries were simulated, with different L or T and their natural frequencies were calculated using Equation (2.2) for the same ratios $\frac{W}{L}$ as the reference. The theoretical predictions (from Equation (2.2) combined with Table 2.2) show excellent agreement with FEM simulations, with discrepancies lower than 1%, validating the model. Changes in the triangular geometry strongly affect the (2,0)-mode natural frequency as shown in Figure 2.3. Additional FEM simulations have shown that the length of the edge L_e affects the natural frequency in general. However, this study focuses on bell plates that exhibit a high-Q (2,0)-mode. The next paragraph will demonstrate that this condition imposes a very limited range of L_e for a given set of the other geometric

dimensions. For this reason, the impact of L_e on the natural frequency of the (2,0)-mode is not detailed in this manuscript and is only illustrated in Appendix B.

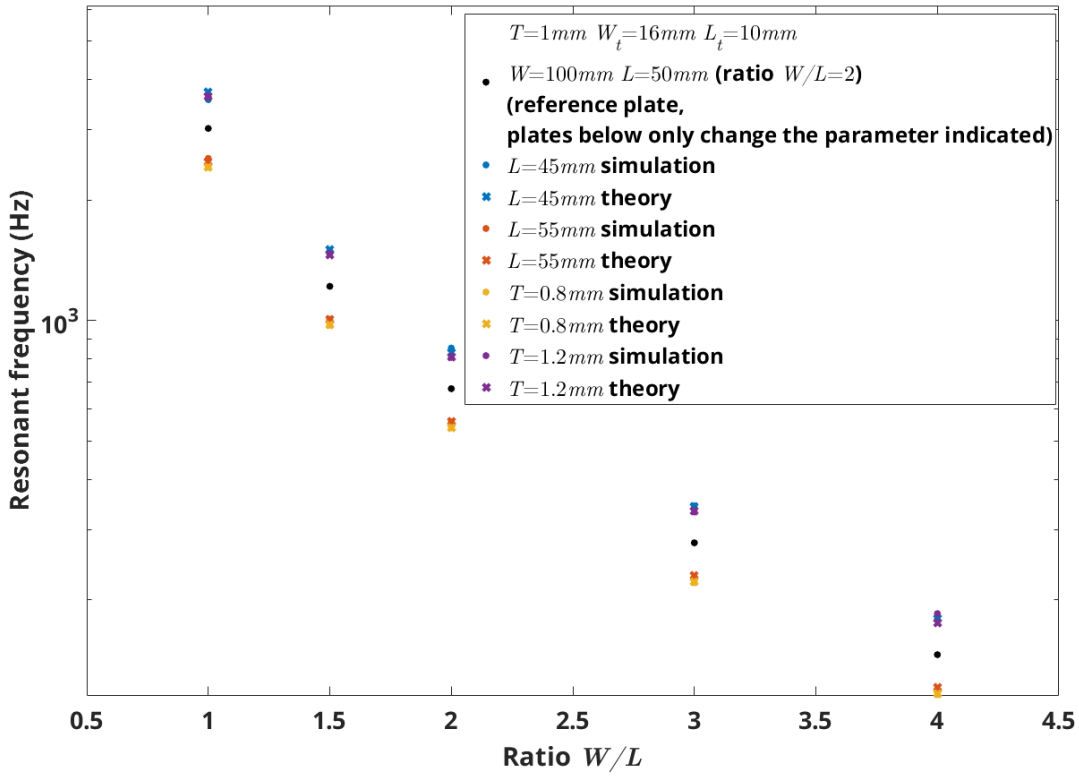

Figure 2.3 – Evolution of simulated natural frequency of the (2,0)-mode with $\frac{W}{L}$ for five plates of different geometries. Parameters not listed in the legend are identical to example parameters (dark dots, see Table.2.1). The discrepancies between theory and simulation are lower than 1%, so that crosses and dots appear superimposed.

$\frac{W}{L}$	λ
4	1.5
3	2.9
2	7
1.5	12.6
1	31.3

Table 2.2 – Eigenvalue λ of the (2,0)-mode for bell plates in different value of $\frac{W}{L}$.

Now that the natural frequency of the (2,0)-mode has been modeled, section 2.3.2 focuses on considerations about the Q-factor.

2.3.2 . QUALITY FACTOR OPTIMIZATION OF THE (2,0)-MODE

As indicated by qualitative studies, the nodal line of the (2,0)-mode should lie on the edge of the tang under free-free boundary conditions. After clamping, the anchor losses are expected to be smaller when the nodal line is close to the clamping position. Figure 2.4

illustrates a comparison of two bell plates with different L_e (all other dimensions being identical). As a qualitative conclusion, the bell plate with the lower quality factor (w.r.t. acoustic losses through the clamped end) corresponds to the plate where the modification induced by the presence of the clamping (compared to the free vibration scenario) is the largest.

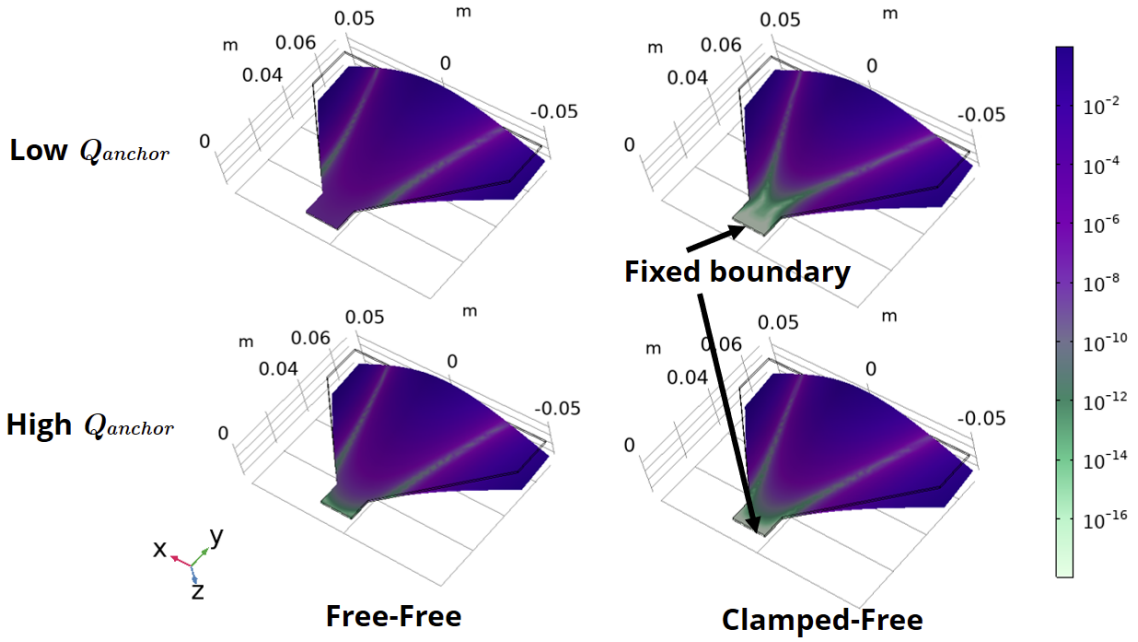

Figure 2.4 – Normalized mode shape simulations of (2,0)-mode under two boundary conditions. Green indicates the nodal line. Left : free-free condition ; right : clamped-free condition. Top : high Q_{anchor} plate ; bottom : high Q_{anchor} plate.

As discussed in section 2.3.1, the whole bell plate may be divided into the tang part and the plate part and the plate part into a triangular part and an edge part. According to FEM simulations, the edge part affects the position of the nodal line and the anchor losses while having little impact on the (2,0)-mode natural frequency. In contrast, changes in the triangular geometry strongly affect both the nodal line position and the (2,0)-mode natural frequency. The evolution of the quality factor with these geometric parameters must still be addressed.

To estimate the potential impact of energy lost at the clamped end, we apply the "low-reflectivity" assumption at this end, meaning that all acoustic energy flowing through the clamping is lost (semi-infinite space). Figure 2.5, Figure 2.6 and Figure 2.7 show the evolution of the Q-factor with respect to L_e, obtained from FEM simulations. Each plate presents an optimum Q_{anchor} for a different value of L_e. Although the exact optimal value depends on geometry, the trend indicates that a maximum Q_{anchor} can be achieved through proper design of L_e.

The second takeaway from Figure 2.5 lies in the dependency of the maximum Q-factor with respect to the length of the tang L_t. When all other dimensions are fixed (except L_e and L_t), increasing L_t appears to increase the maximum achievable Q_{anchor} at the optimal L_e. However, this comes at the cost of an increasingly large sensitivity to L_e, which makes it practically irrelevant to study very long tangs. In general, the higher the optimum Q-factor is, the stronger the sensitivity with respect to L_e (as shown by the width of each peak),

but excessively large values are impractical due to fabrication constraints and reduced stiffness of the first bending mode. Therefore, the design requires a trade-off between Q-factor and structural robustness.

From Figure 2.6, a thicker and larger plate may increase the Q_{anchor}. Interestingly, within a same requirement of natural frequency, a larger and thicker plate has the potential to reach a higher Q_{anchor} without increasing the sensitivity to L_e around the optimum. This may be attributed to the corresponding increase of mass. The increase of mechanical energy stored in the resonator is stronger than the increase in radiated power. However, the trend of Q_{anchor} as increasing T is not monotonic. When the thickness is excessive—for instance, exceeding $10mm$ for plate with the dimension of Table 2.1, the Q-anchor value becomes lower than the maximum Q_{anchor} of each curve in Figure 2.6, about 15×10^3. This indicates that the $Q_{anchor} - versus - T$ relationship shown in the Figure 2.6 represents a local optimization specific to a particular scenario. Extreme cases involving excessive deformation of the bell plate are not discussed in this paper, because the vibration of that plate is out of the scope of bell plate ; or even the (2,0)-mode doesn't belong to the flexural plate mode. Nevertheless, one should keep in mind that, since the scope of this thesis aims at MEMS-scale bell plates, some requirements in MEMS design limit the thickness of bell plate, such as the actuation voltage to excite the plate (detail in section 3).infinitely-increasing trend of the bell plate Q-factor, such as the actuation voltage to excite the plate (detail in section 3).

Figure 2.7 shows that a larger W (larger $\frac{W}{L}$) tends to increase the Q_{anchor}. However, many properties change at the same time, such as the natural frequency and the stiffness of the first bending mode. The evolution of the frequency with W is included in λ according to Equation (2.2). During design, we set the value $\frac{W}{L}$ and modify the other dimensions to match specific requirements (eg. frequency, voltage, fabrication constrains).

CONCLUSION ON Q-FACTOR EVOLUTION

In this section, the influence of geometric parameters on macroscopic bell plates has been analyzed using theoretical models and FEM simulations. The results show that the natural frequency of the (2,0)-mode is mainly governed by the plate geometries with good agreement between analytical predictions and simulations.

The study also highlights that the quality factor is strongly linked to the position of the nodal line. In particular, the edge length L_e is identified as the key parameter for optimizing Q_{anchor}, as it significantly affects anchor losses while having a limited impact on the natural frequency. For each geometry, an optimal value of L_e exists.

Finally, several design trade-offs are identified, notably involving L_t, $\frac{W}{L}$, and the overall size of the plate, which influence both Q-factor and mechanical robustness. These results provide useful guidelines for the design of high-Q bell plates (detailed in next Chapter 3).

In the next section, based on the theory, macroscopic bell plates are designed, fabricated and characterized.

2.4 . FIRST QUANTITATIVE CHARACTERIZATION OF MACROSCOPIC BELL PLATE

To verify some some of the main takeaways of section 2.3, a set of stainless-steel bell plates was fabricated in our workshop at C2N. These plates were designed with different

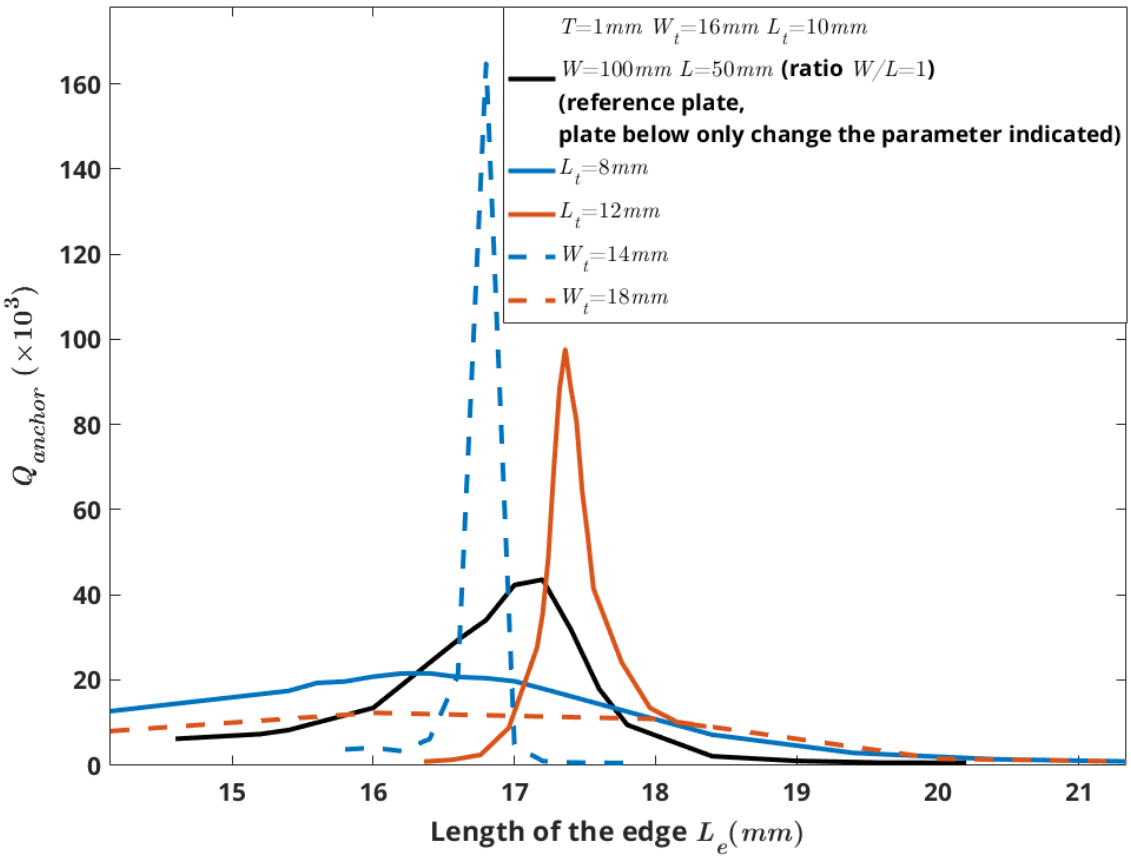

Figure 2.5 – Evolution of Q_{anchor} of the (2,0)-mode with L_e by FEM simulation under tang variations.

dimensions to investigate their influence on the bell plate resonant properties. In particular, our study from section 2.3 highlights that L_e is the only parameter that combines a strong impact on the shape of the nodal lines and a relatively low impact on the natural frequency. For this reason, we now focus on fine-tuning L_e for Q-factor optimization.

2.4.1 . EXPERIMENTAL SETUP AND CHARACTERISTIC OF THE BELL PLATES

To verify the sensitivity to L_e, two bell plates were characterized. Their dimensions are listed in Table 2.3. Table 2.5 summarizes the Q-factors and natural frequencies of the two plates obtained from FEM simulations.

Sample	T	Wt	Lt	W	L	Le
Plate 1	1	16	10	100	48	18
Plate 2	1	16	10	100	48	20

Table 2.3 – Dimensions (in mm) of the fabricated macroscopic bell plates. L_{tot} of Plate 1 and Plate 2 are $68.3mm$ and $70.3mm$ respectively.

The two plates are very similar, except for the edge length, which was intentionally varied to analyze the influence of the nodal line position on Q.

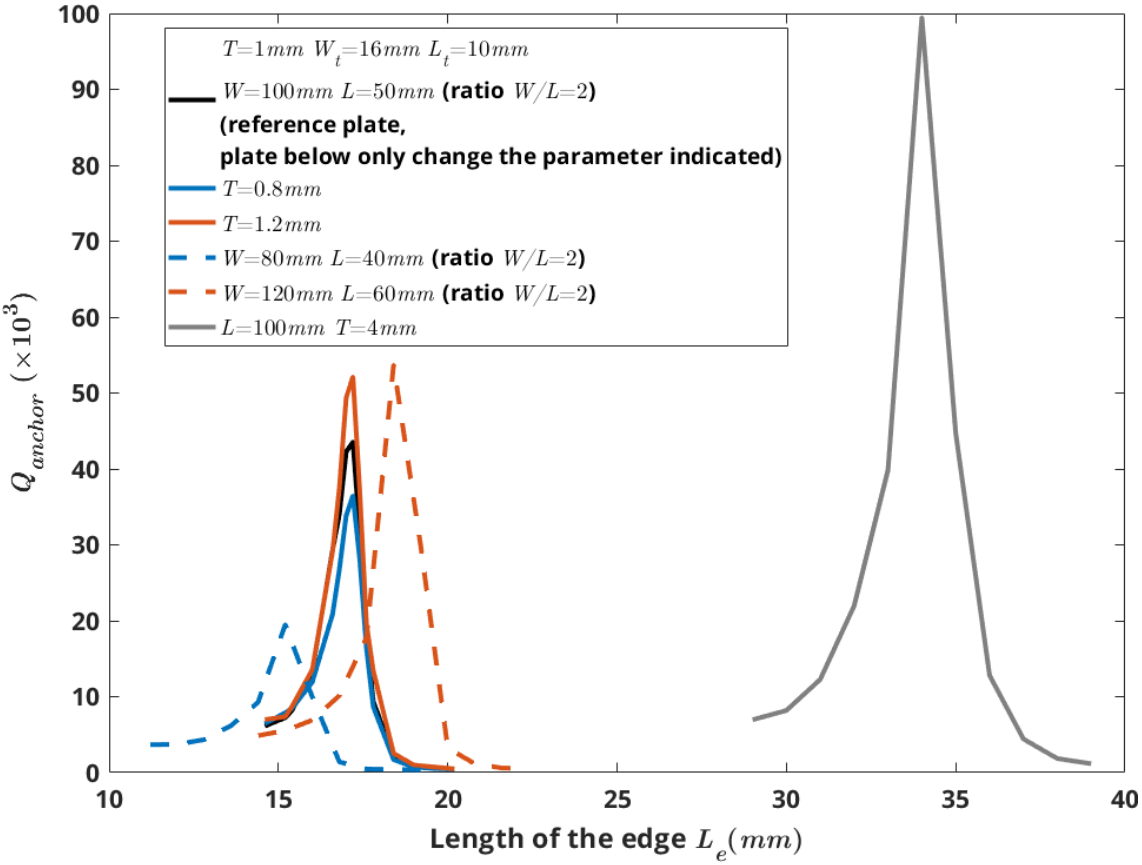

Figure 2.6 – Evolution of Q_{anchor} of the (2,0)-mode with L_e by FEM simulation for different thicknesses and widths of the plates (maintaining the ratio $\frac{W}{L}$). The grey line corresponds to changing T and L at the same time while maintaining the natural frequency of the reference (dark line).

Sample	First mode		(2,0)-mode	
	f (Hz)	Q_{anchor}	f (Hz)	Q_{anchor}
Plate 1	58	561	674	42266
Plate 2	60	563	678	20092

Table 2.4 – Simulation results of the two plates under clamped-free conditions and estimation of the air damping after comparison with ring-down measurements.

Section 2.4.2 presents experimental ring-down results and section2.4.3.

2.4.2 . RING-DOWN CHARACTERIZATION

Both plates were fabricated from stainless steel. The two plates were fixed on a heavy copper support to ensure stable clamping at the tang. The ring-down response at the center of the free end was measured using a laser displacement sensor (KEYENCE LK-H050 with controller LK-G5001P). An example of ring-down result is shown in Figure 2.8.

Two modes are observed in each ring-down response. The ring-down responses are modeled as logarithmic decrement curves assuming no coupling between the two modes.

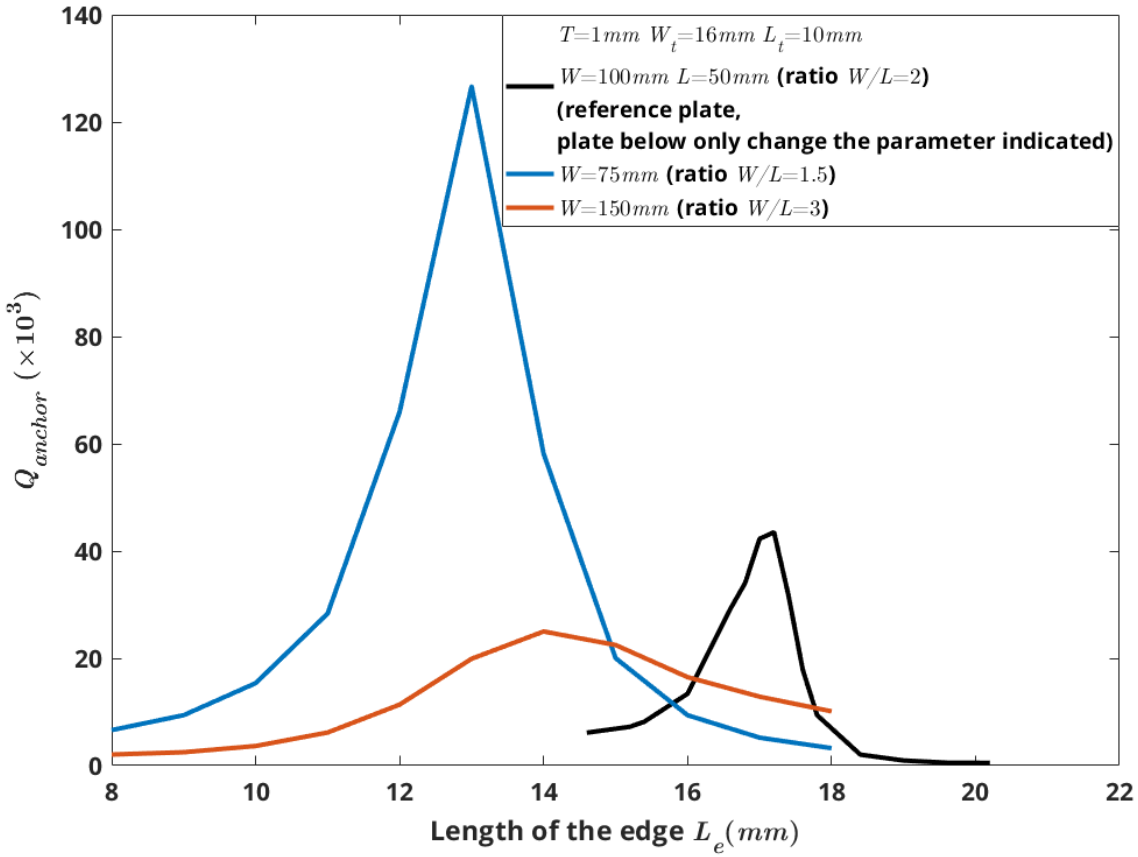

Figure 2.7 – Evolution of Q_{anchor} of the (2,0)-mode with L_e by FEM simulation with different ratio $\frac{w}{L}$

The following expression is used :

$$A_{tot} = \sum_{i=1,2} A_i \times e^{\left(-\frac{\omega_i t}{2Q_i}\right)} \sin(\omega_i t + \phi_i) \tag{2.3}$$

where A_i is the initial displacement amplitude, Q_i is the quality factor, ω_i is the angular frequency, and ϕ_i is the phase at $t = 0$.

Table 2.5 summarizes the Q-factors and natural frequencies of the two plates.

Sample	First mode		(2,0)-mode	
	f (Hz)	Q	f (Hz)	Q
Plate 1	60	178	642	7350
Plate 2	68	150	676	4998

Table 2.5 – Summary of ring-down responses of two plates under clamped-free conditions

According to simulation results (see Table.2.4), the $60Hz$ signal corresponds to the first bending mode and the $650Hz$ signal to the (2,0)-mode. As predicted by the simulations,

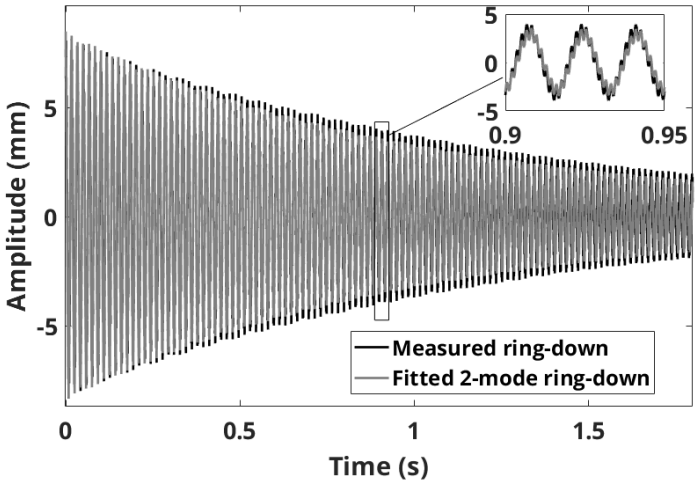

Figure 2.8 – Ring-down response and fitting curve including two modes for each macroscopic bell plate.

Plate 1 exhibits a higher Q, exceeding 7000 in air. Based on research of other musical instrument, such as [81], [82] and [83], this result is within an expected range, between 10^3 and 10^5.

According to the FEM simulation results, the dissipation is dominated by anchor losses and in the interaction between the moving structure and the surrounding air. Whether these latter losses are due to viscous damping (friction) of to acoustic radiation has not been analyzed further, due to our final objective to operate MEMS bell plates under vacuum.

Anchor losses are hard to predict precisely from ab initio FEM simulations because they depend on various clamping conditions (constraint, exact position). Nonetheless, the Q-factor related to dissipation in air (Q_{air}) is estimated at the magnitude level of 10^4 to 10^5 based on these experimental results. Acoustic radiation and fluid interaction introduce a damping ratio typically on the order of 10^{-4} to 10^{-2} for vibrating structures in air, as shown in study [84]. This corresponds to quality factors related to the interaction with air in the range of 10^2–10^4. Even though there is a large uncertainty on the estimated Q_{air}, in the future study of MEMS, the device will work under vacuum, at levels of pressure where acoustic dissipation and friction are practically negligible.

This characterization together with FEM simulation results demonstrates that only a careful geometric design enables the bell plate to achieve a high Q. In particular, the sensitivity of Q_{anchor} to L_e is validated.

2.4.3 . FREQUENCY RESPONSE OF THE (2,0)-MODE

In addition to ring-down measurements, frequency sweep experiments were performed on Plate 1 (higher-Q sample) to verify that the (2,0)-mode can be independently actuated. This is even more required that the previous ring-down measurements may have resulted from coupling between the two modes, which was so far assumed nonexistent in our experimental parameter estimation. The plate was mounted on a shaker (Figure 2.9) capable of generating frequency sweeps around resonance.

Two sweeps were performed at acceleration levels of 0.63 ± 0.03 m/s^2 and 1.58 ± 0.08

m/s^2, as shown in Figure 2.10.

The system is modeled as a linear Lorentzian response at low amplitudes and as a nonlinear oscillator including a cubic term at larger amplitudes. The governing equation is :

$$\frac{d^2x}{dt^2} + \frac{\omega_0}{Q}\frac{dx}{dt} + \omega_0^2(x + \gamma x^3) = a\sin(\omega t + \phi) \tag{2.4}$$

Model parameters are estimated using a previously published method [85], and the fitted results are shown in Figure 2.10.

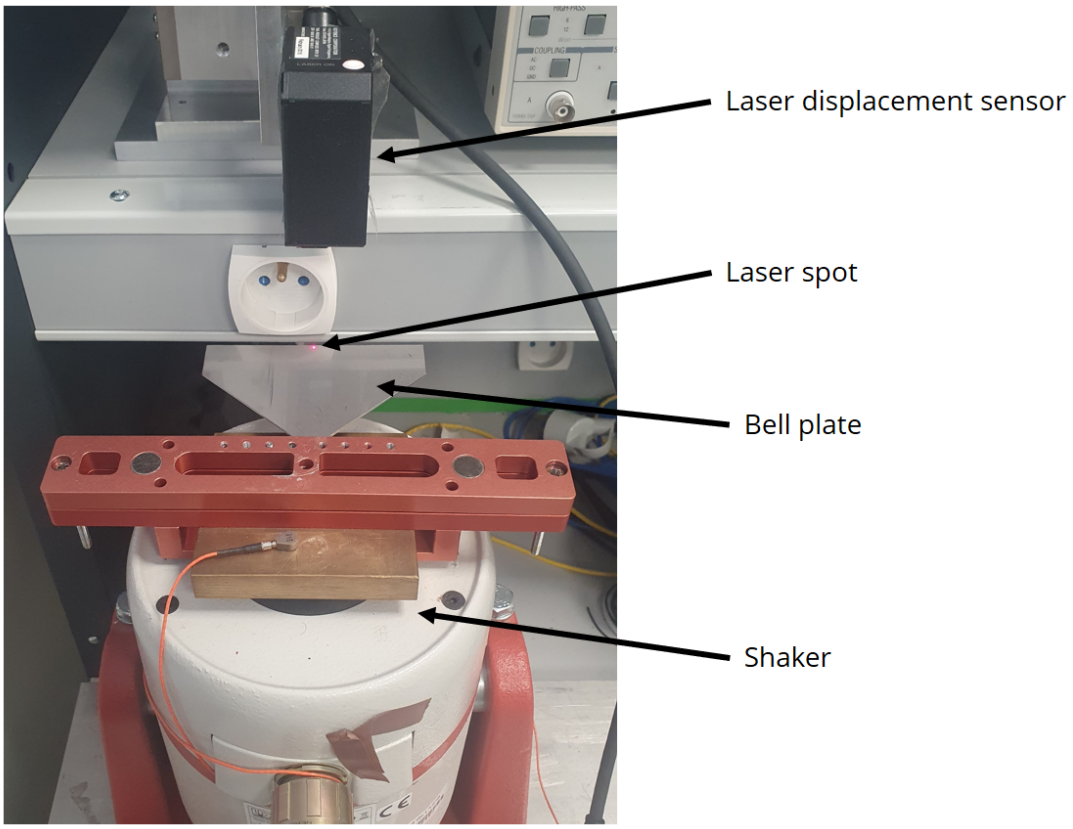

Figure 2.9 – Experimental setup for macroscopic bell plate

The agreement between the model and the measured response is excellent. The natural frequency is estimated at 641.84 Hz, and the quality factor is 8769. The discrepancy between Q values obtained from frequency response and ring-down measurements (8769 and 7350 respectively) are likely due to variations in clamping conditions between the two setups.

At large amplitude oscillations, several sources of nonlinearity may be involved, including geometric effects or stress at the clamped end [86]. To investigate this, static nonlinear FEM simulations were performed. Three forces were applied as shown in Figure 2.11, with relative magnitudes $F_c : F_m : F_w = 3 : 16 : 28.2$ to obtain a similar static deformation of (2,0)-mode.

The results, shown in Figure 2.12, compare nonlinear simulations with linear ones. Large deformations induce a slight spring-hardening effect. Fitting the FEM data with $F(x) = K(x + \gamma x^3)$ yields $\gamma = 563m^{-2}$, which is consistent with the value extracted

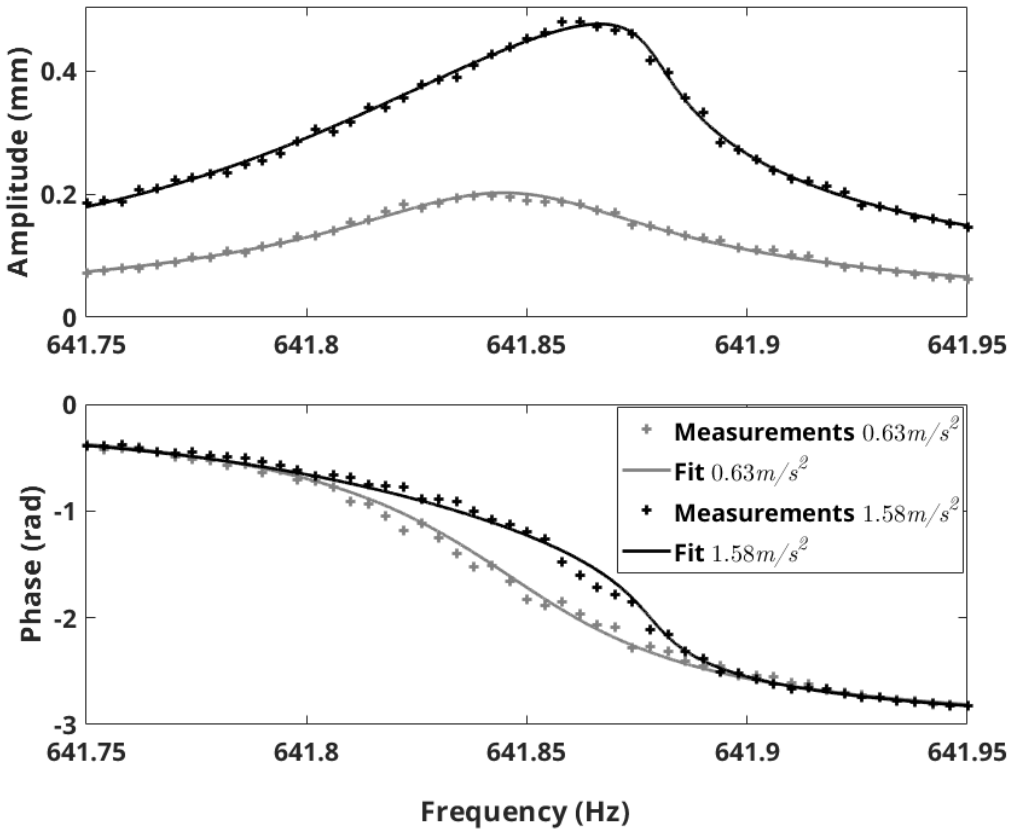

Figure 2.10 – Frequency response and fitting curve of the (2,0)-mode

from experimental frequency sweeps. Although this does not fully prove that geometric nonlinearity is the sole nonlinear mechanism, it strongly supports this interpretation.

These experimental frequency sweeps prove that the (2,0)-mode can be actuated individually and still exhibit high-Q performance. Moreover, although we aim at maintaining the plate in linear regime for the characterization of MEMS bell plates, geometric nonlinearity is expected to appear at large vibration amplitudes.

2.5 . CONCLUSION

In this section, a first quantitative characterization of macroscopic bell plates was presented. Both FEM simulations and experimental measurements demonstrate that the position of the nodal line of the (2,0)-mode plays a key role in minimizing anchor losses and achieving high Q-factors. The results confirm that appropriate geometric design, in particular the tuning of the parameter L_e, enables significant improvement of the Q-factor while maintaining the desired natural frequency. Furthermore, nonlinear behavior observed at higher vibration amplitudes is shown to be consistent with geometric nonlinearities. These findings validate the proposed design strategy and provide a solid basis for the development of high-Q MEMS bell plate resonators.

The design method inspired by modeling bell plates is still useful in MEMS scenarios,

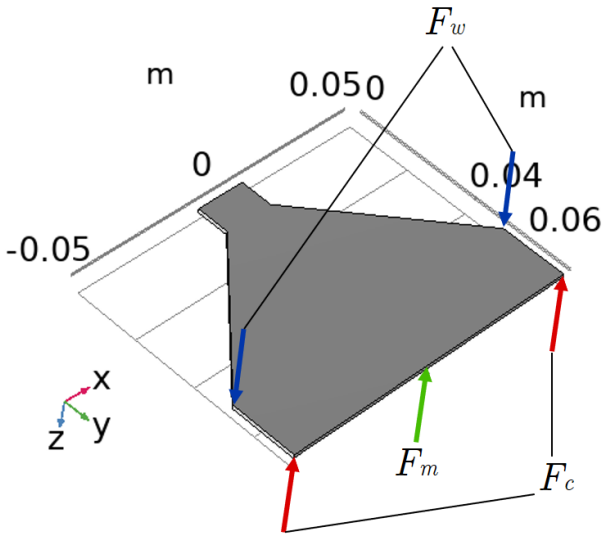

Figure 2.11 – Forces applied in static structural simulations

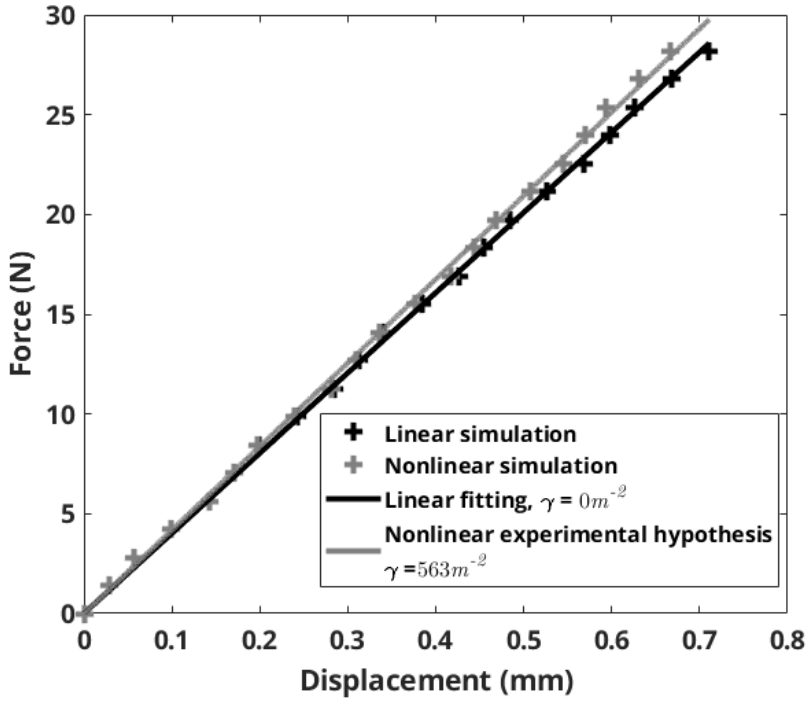

Figure 2.12 – Linear and nonlinear static FEM simulation results. The y-axis corresponds to the magnitude of F_w.

except that we need to consider the anisotropic material silicon. The behavior of silicon bell plates is expected to be similar to these metal plates, such as the ability to actuate the (2,0)-mode individually and the appearance of nonlinearity at large amplitude.

Overall, this study provides both physical insight and practical design guidelines, for-

ming a solid foundation for the subsequent development of MEMS bell plate resonators.

3 - DESIGN AND FABRICATION OF MEMS BELL PLATE ON SOI WAFERS

3.1 . INTRODUCTION

In Chapter 2, we established a set of analytical relationships that link the geometric parameters of a macroscopic bell plate to its natural frequencies. We also analyzed the Q-factor through numerical simulations and drew some conclusions about the impact of the geometric dimensions of the plate. The present chapter proposes a methodology for the design of microscopic bell plates in silicon-on-insulator (SOI) micro-fabrication. Six geometric degrees of freedom — thickness T, length of the tang L_t, width of the tang W_t,length of the triangular-section L, length of the edge L_e and width of the plate W—are optimized to satisfy the following design goals.

In this chapter, our requirements are listed at beginning. Then, in Section 3.2, a design optimization strategy is detailed (see Section 3.2.2). Finally, the complete micro-fabrication sequence is presented. The chapter concludes with scanning electron-microscope (SEM) images that check the consistency between the actual plates and the ideal geometry.

3.2 . DESIGN OF MICROSCOPIC BELL PLATE

Six dimensions are involved in the design of the bell plate : the thickness (T), the length of the tang (L_t), the width of the tang (W_t), the length of the triangular part (L), the length of the edge (L_e), and the plate width (W). This section details the design strategy and explains the rationale behind the chosen values.

REQUIREMENTS

Before starting the design, the resonator requirements must be clarified. Table 3.1 lists all the requirements for this project. Our target frequency lies in the hundreds kHz range, and we aim for a total quality factor Q_{tot} higher than 10^5. Moreover, the design complies with a standard SOI MEMS manufacturing process. The resonator can be integrated into a circuit with low actuation voltage and enables electrical detection.

Frequency	$10kHz$–$1MHz$
Quality factor	$> 10^5$
Fabrication tolerance	$2\mu m$
Technology	SOI
Working condition	Actuation voltage < 20 V DC bias + 5 V AC
	Pressure below 5×10^{-4} Pa
	Room temperature
	Electrical detection

Table 3.1 – Summary of the requirements for MEMS bell plate design in this work

EXPECTATION OF MEMS BELL PLATE ON SOI WAFER

The schematic of SOI wafer cross-section was illustrated in Figure 3.1. The top layer is the device layer, where the bell plate structure is formed. In the middle is the oxide layer, which also serves as the sacrificial layer; the oxide layer at specific locations is etched away to release the bell plate structure above it. The bottom layer is the substrate, which is also the bulk layer.

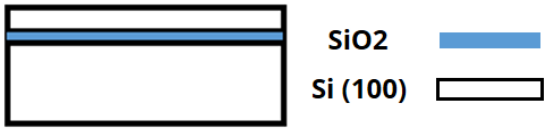

Figure 3.1 – Schematic diagram of SOI cross-section

Figure 3.2 illustrate the schematic of MEMS bell plate structure expectation on SOI wafter in 3D model. We expect the device layer and the substrate to be connected into the circuit as the anode and cathode of a capacitor, respectively, with the device driven by electrostatic forces to perform out-of-plane resonant motion.

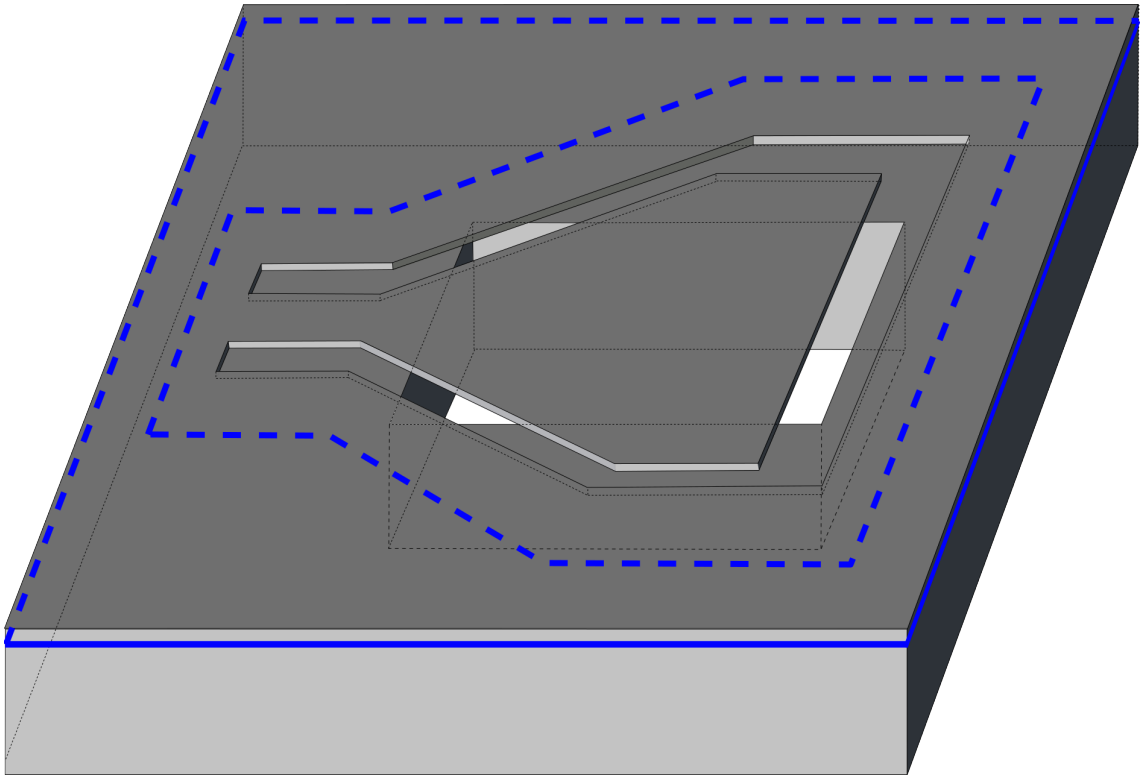

Figure 3.2 – 3D Schematic diagram of the expected MEMS bell plate. Blue line indicate the contour of silicon dioxide layer which will be etched to release the device.

3.2.1 . DESIGN STRATEGY

The design is based on SOI technology. Since silicon is an anisotropic material, the natural frequency cannot be precisely obtained directly from Equation 2.2. Instead, we rely

on FEM simulations for validation, while the qualitative conclusions from the macroscopic plate analysis remain applicable. In this subsection we present a procedure to achieve a high-Q MEMS bell plate.

All in all, the design optimization follows the following steps : (1) determine the target frequency; (2) achieve a high-Q design; (3) verify actuation feasibility; and (4) confirm compatibility with a standard SOI fabrication process. Several designs that satisfy these margins were finally obtained.

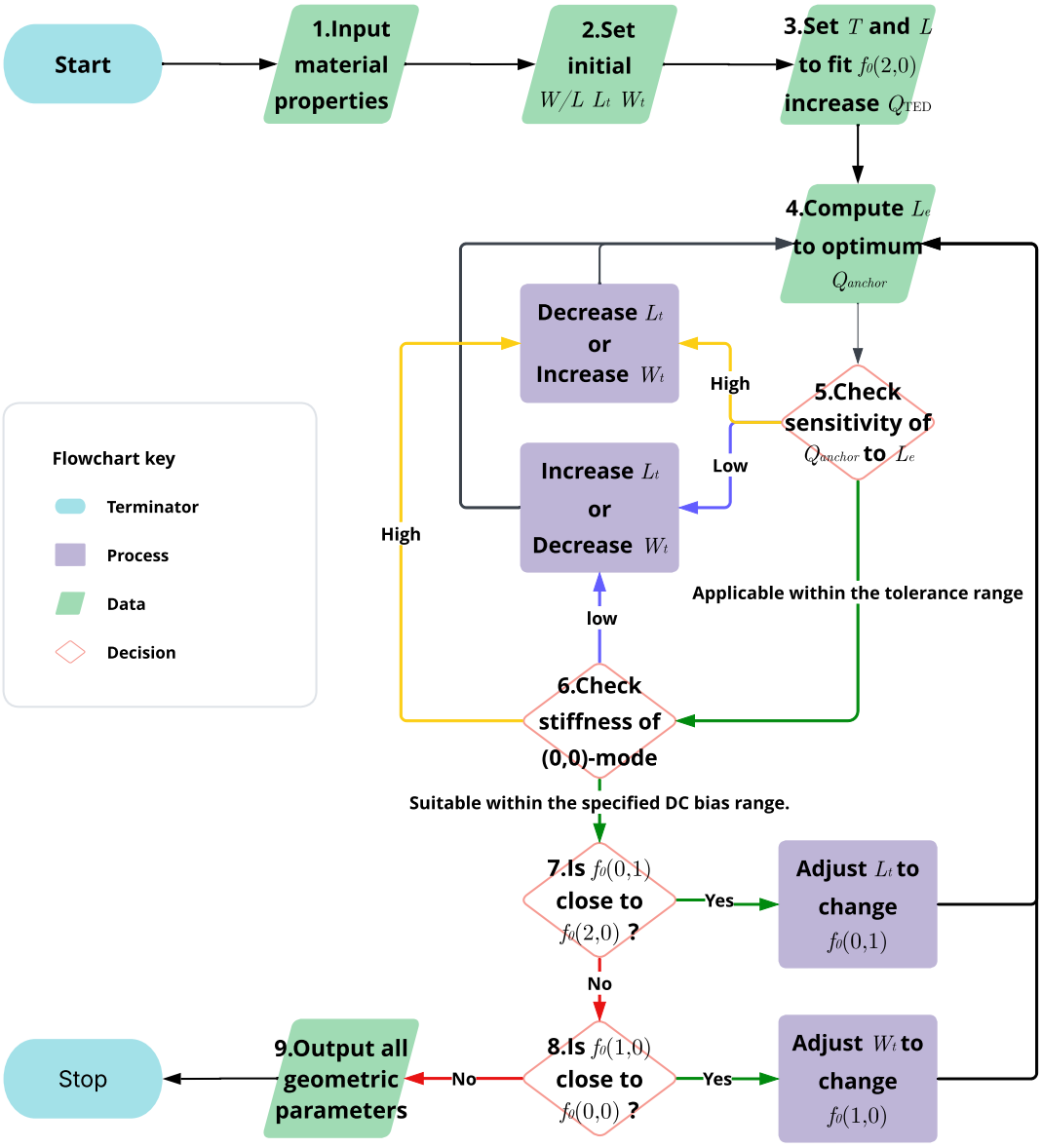

Figure 3.3 – Flowchart of the MEMS bell-plate design.

Figure 3.3 depicts the flow chart of the design optimization process. First, the material parameters are defined and an initial set of geometric parameters is assigned. The thickness T is determined at the outset, as TED is one of the primary dissipation mechanisms in MEMS bell-shaped plates; furthermore, based on the description of TED in Section 1.3.2,

TED can be estimated using the thickness via a simplified model. We wish for Q_{TED} to be significantly higher than Q_{anchor}. If this estimation is verified by FEM simulation, the value of T is fixed and is not altered again until the simulation is complete. The length L is then adjusted, via FEM simulation, until the natural frequency of the (2,0) mode falls within the target range.

We then run FEM simulations of the evolution of Q_{anchor} with respect to L_e and examined its sensitivity. To satisfy the fabrication tolerance requirement of $2\mu m$, we must verify that Q_{anchor} remains within the range of $Q > \frac{1}{2}Q_{\mathrm{anchor},max}$, when L_e varies by $2\mu m$ (the evolutions referring to the discription in Section 2.3.2). If the sensitivity is too high, we adjust the tang dimensions or increase the thickness, then repeat the loop (return to step 3 or 4).

After these iterations, we consider the operating conditions of the microscopic bell plate. Based on the available SOI wafers, the SOI oxide layer is set to $1\ \mu\mathrm{m}$. The design should allow easy actuation while keeping the structure sufficiently stiff so that the vibration amplitude reaches at least $100\ \mathrm{nm}$ under the prescribed voltage. If necessary, we readjust the tang (return to step 4) and re-validate the performance.

Finally, the eigenfrequencies of the plates should be sufficiently far from one another - and ideally far from multiples of one another - at least for the first few modes to avoid (linear or nonlinear) coupling between these modes. Since the device is supposedly very high-Q, the bandwidth of the (2,0)-mode is extremely narrow, which reduces the risk of modal cross-coupling. However, a careful design procedure must include the latter verification. As discussed in Section 2.3.1, three modes exist near the (2,0) mode. They can be grouped into bending along the lateral direction ((0,0) and (0,1) modes) and bending along the horizontal direction ((1,0) and (2,0) modes). Within each group the two modes are independent, but between groups strong coupling can occur if the resonant frequencies are too close. In practice, for moderately deformed bell plates, the (0,1) mode is the closest to (2,0), and the (0,0) mode is the closest to (1,0). Therefore, we decided to set a minimum of 10% frequency margin between each mode to account for the possible discrepancies between the expected eigenfrequencies and the ones obtained on actual devices after fabrication.

3.2.2 . FINAL DESIGNS

Following the bell-plate principles validated in Chapter 2 and the strategy described in Section 3.2.1, the microscopic bell-plate resonator designs were set. A summary of the final designs is presented below.

MATERIAL

The material of the MEMS device must be silicon. Silicon is widely used in MEMS because SOI wafers can be processed with standard micro-nanofabrication techniques. Since silicon is anisotropic, Equation 2.2 cannot be applied directly. The resonant frequencies are therefore obtained from FEM simulations using a density of $2330\ \mathrm{kg/m^3}$ and the elasticity matrix :

$$C_{100} = \begin{bmatrix} 166\ \text{GPa} & 64\ \text{GPa} & 64\ \text{GPa} & 0\ \text{GPa} & 0\ \text{GPa} & 0\ \text{GPa} \\ 64\ \text{GPa} & 166\ \text{GPa} & 64\ \text{GPa} & 0\ \text{GPa} & 0\ \text{GPa} & 0\ \text{GPa} \\ 64\ \text{GPa} & 64\ \text{GPa} & 166\ \text{GPa} & 0\ \text{GPa} & 0\ \text{GPa} & 0\ \text{GPa} \\ 0\ \text{GPa} & 0\ \text{GPa} & 0\ \text{GPa} & 80\ \text{GPa} & 0\ \text{GPa} & 0\ \text{GPa} \\ 0\ \text{GPa} & 0\ \text{GPa} & 0\ \text{GPa} & 0\ \text{GPa} & 80\ \text{GPa} & 0\ \text{GPa} \\ 0\ \text{GPa} & 0\ \text{GPa} & 0\ \text{GPa} & 0\ \text{GPa} & 0\ \text{GPa} & 80\ \text{GPa} \end{bmatrix}$$

corresponding to the anisotropic properties of (100) silicon [80].

DETERMINE THE THICKNESS

Equation (1.15) predicts that the frequency corresponding to the strongest thermoelastic dissipation strongly depends on the device-layer thickness. For a thickness of $5\ \mu m$, using the thermal diffusivity of single-crystal silicon at room temperature, $\chi \approx 9\times10^{-5}\,\mathrm{m}^2/\mathrm{s}$, the minimum TED-limited quality factor is expected near $5.6\,\mathrm{MHz}$, whereas for thicknesses of $10\ \mu$m and $20\ \mu$m, the corresponding frequencies decrease to approximately $1.4\ \mathrm{MHz}$ and $0.35\ \mathrm{MHz}$, respectively.

This analysis provides an important design guideline for thin silicon MEMS resonators. For device layers thinner than approximately $10\ \mu$m, the strongest thermoelastic dissipation is expected to occur at frequencies in the megahertz range. Consequently, resonators operating far below this frequency range are generally less affected by TED, whereas resonators operating near $f_{TED,min}$ may experience a substantial reduction in the TED-limited quality factor.

The MEMS bell plates investigated in this work employ silicon device layers with thicknesses of 5 or $10\ \mu m$ (the available SOI wafers we have) and operate in the frequency range of approximately $200\ \mathrm{kHz}$ to $450\ \mathrm{kHz}$. These frequencies remain below the estimated TED-loss peak frequencies predicted by Equation (1.15). Furthermore, based on the initial dimensions set, FEM simulations performed in this work predict TED-limited quality factors that are several orders of magnitude higher than the experimentally measured quality factors. The Q_{TED} is about 1.373×10^6 for T of $10\ \mu m$ and 1.240×10^7 for T of $5\ \mu m$ at the resonance of (2,0)-mode.

This observation suggests that thermoelastic damping is unlikely to be the dominant dissipation mechanism in the investigated devices. Instead, the discrepancy between the simulated TED limit and the measured quality factor indicates that extrinsic loss mechanisms play a major role. Among these mechanisms, anchor losses are particularly relevant because they strongly depend on the resonator geometry and on the vibration amplitude at the support region.

LENGTH OF THE TRIANGLE-LIKE PART

L is the parameter that determines the frequency. COMSOL simulations indicate that $L = 250\ \mu\mathrm{m}$ yields a natural (2,0)-mode frequency close to $200\ \mathrm{kHz}$ for a silicon device with a thickness of $5\mu m$ and $450\ \mathrm{kHz}$ with a thickness of $10\mu m$, which lie within our frequency range of interest.

RATIO OF W/L

As analysed in Chapter 2, the W/L ratio is a key parameter for the natural frequency. In our design we keep $W/L \approx 1$. First, this ratio has little influence on Q_{anchor}, which can be controlled by L_t, W_t and T. Second, the natural frequency can be tuned effectively by other parameters such as the thickness T and the plate length L. Maintaining the ratio close to unity also preserves the possibility of arranging four plates radially to form a "quadra-plate" (a radial pattern with a central anchor), which could further increase Q_{anchor} in future work.

DESIGN OF THE TANG PART AND THICKNESS

These three parameters were refined through several FEM-simulation loops (see Figure 3.3). Eventually we obtained $L_t = 85\ \mu\mathrm{m}$ and $W_t = 40\ \mu\mathrm{m}$. Simulations show that the tang provides sufficient support, the first four modes are well separated, and the resulting Q_{anchor} together with its sensitivity to L_e meets the specifications.

Finally, a set of tang geometries was added to the mask for lithography : L_t varies from $45\ \mu\mathrm{m}$ to $85\ \mu\mathrm{m}$ and W_t from $40\ \mu\mathrm{m}$ to $80\ \mu\mathrm{m}$.

LENGTH OF THE EDGE DESIGNED WITH UNCERTAINTY

To achieve a high Q, we have shown that Q_{anchor} can be tuned by L_e, while L_e has little effect on the natural frequencies of the first bending mode and the (2,0) mode. Using the same FEM method described in Section 2.3.2, the maximum Q_{anchor} occurs around $L_e \approx 90\ \mu\mathrm{m}$ (exact value depends on the other dimensions). Considering fabrication tolerances, under-etching, and possible deviations between the simulated material properties and the real ones, we defined a family of designs with L_e ranging from 80 to $100\ \mu\mathrm{m}$.

WAFER CHOSEN

The device thickness and material are fixed after the design stage ; they depend on the device-layer thickness and physical properties of the SOI wafer. We require a low actuation voltage, i.e., electrostatic excitation with a modest voltage. With a $1\ \mu\mathrm{m}$ air gap, simulations predict a pull-in voltage of about $15\ \mathrm{V}$. Consequently we selected a thin-device-layer SOI wafer consisting of a $5\ \mu\mathrm{m}$ or $10\ \mu\mathrm{m}$ device layer, a $1\ \mu\mathrm{m}$ BOX layer, and a $400\ \mu\mathrm{m}$ handle layer (illustrated in Figure 3.1). Ultimately, two batches of SOI wafers, low-doped and high-doped (material properties listed in Table 3.2), were used in this study.

OPTIMIZATION OF ELECTRODE

From the mode shape (see Figure 2.2), we can know that a plane plan parallel with the plate working as an electrode is not optimum. Because the center part moving opposite to the two sides part (separated by the nodal line), we planed to etching a rectangular hole on the electrode on the substrate (shown in Figure 3.4). This optimization approach will improve the transduction coefficient of the (2,0)-mode. The detail including calculation and simulation are demonstrated in Chapter 5.

	Low-doped wafer	High-doped wafer
Orientation	(100)	(100)
Device thickness (μm)	5 ± 0.5	10 ± 0.5
Device doping	P (B)	P (B)
Device resistivity ($\Omega \cdot \mathrm{cm}$)	1–20	0.001
BOX thickness (μm)	$1 \pm 5\%$	$1 \pm 5\%$
Handle thickness (μm)	400 ± 10	400 ± 10
Handle doping	P (B)	P (B)
Handle resistivity ($\Omega \cdot \mathrm{cm}$)	1–20	0.00001

Table 3.2 – Physical properties of the low-doped and high-doped SOI wafer.

CONCLUSION OF DESIGN

The geometric parameters are summarised in Table 3.3. Not all of them were fabricated and characterized successfully. In the next Chapters 4 and 5, the detail of each sample characterized will be shown respectively.

Parameter	Value
T	5 or 10 μm
W_t	40–80 μm
L_t	45–85 μm
W	500 μm
L	200–300 μm (so that W/L ranges from 0.8 to 1.2)
L_e	90–100 μm

Table 3.3 – Initial design parameters.

3.3 . FABRICATION OF MICROSCOPIC BELL PLATE ON SOI WAFER

In this section we present the fabrication process in detail. First, the manufacturing plan is presented in the form of a flowchart. Subsequently, the technical details of each step are elaborated upon.

3.3.1 . FABRICATION PROCESS

The main fabrication steps (Figure 3.8) follow a standard surface-micromachining SOI flow. It starts with UV lithography on the device layer using a mask ordered from Delta Mask. Afterwards, a DRIE (Bosch-like) process [87, 88] etches through the device layer and the oxide layer.

Subsequent metal deposition by electron-beam evaporation is followed by a second lithography/DRIE sequence on the backside, using a mask optimised for the electrode geometry. An isotropic silicon-etching step with $\mathrm{XeF_2}$ is then employed to enlarge the backside holes, facilitating HF access to the buried oxide in the next stage. Finally, an isotropic HF (wet or vapor) release etch frees the structure [89, 90].

3.3.2 . SPIN COATING

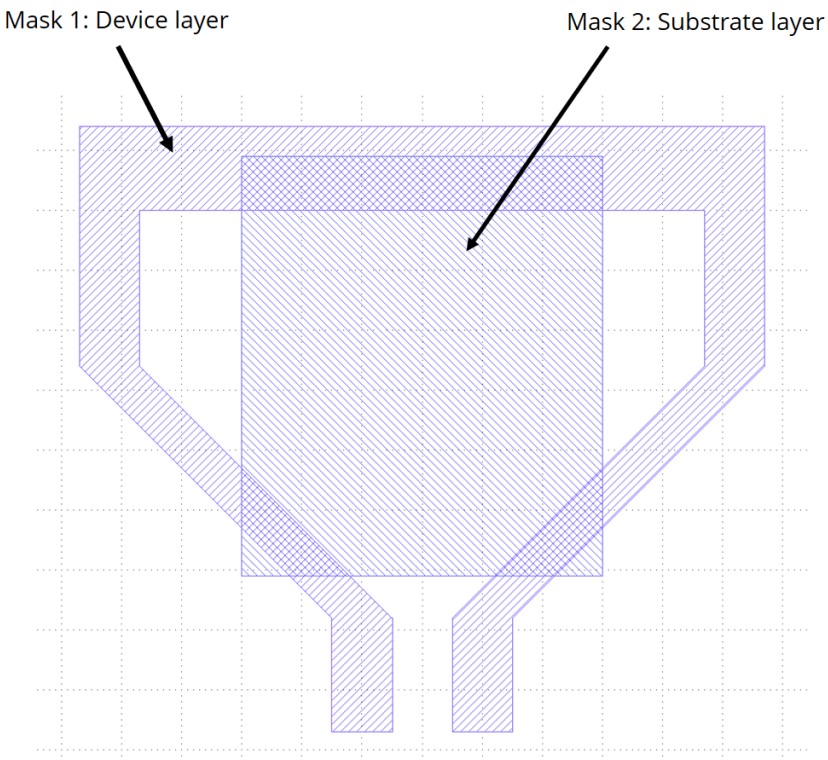

Figure 3.4 – Schematic diagram of the masks of the bell plate with holes on the substrate. Area in shadow is designed to be etched, two type of shadow correspond to different layers.

Spin coating is a widely used thin-film deposition technique in microfabrication and photolithography for producing uniform photoresist layers on planar substrates. Prior to coating, the wafer is cleaned sequentially with acetone, isopropyl alcohol (IPA), and deionised (DI) water, then baked at $120°\mathrm{C}$ for $10\ \mathrm{min}$ to remove residual moisture and improve photoresist adhesion.

A liquid photoresist is dispensed onto the wafer centre and the wafer is accelerated to a predefined rotational speed. Centrifugal force spreads the liquid uniformly; subsequently the solvent evaporates on a hot plate, leaving a thin, uniform film (see Figure 3.6).

The final film thickness is primarily determined by the spin speed, photoresist viscosity, solvent-evaporation rate, and spin duration. In general, higher speeds produce thinner layers because of the stronger radial outflow. Spin coating is especially suitable for MEMS fabrication because of its simplicity, repeatability, and the high uniformity it provides across the wafer.

After spin coating, a soft-bake removes residual solvents and enhances mechanical stability and adhesion before UV exposure and development. For thick photoresists a longer bake is required to avoid internal stress and crack formation.

Two spin-coating steps are required in this work : one for the device-layer lithography

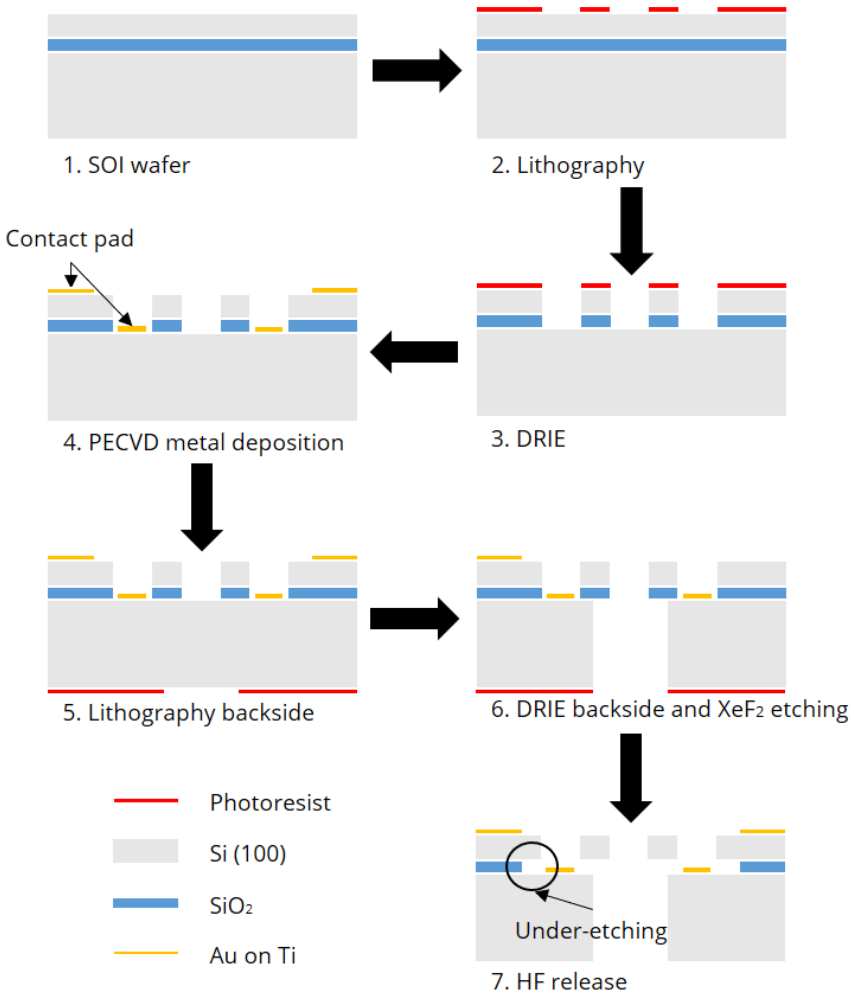

Figure 3.5 – Schematic of the device cross-section along fabrication. The circle emphasizes the lateral under-etching of the SiO_2 layer.

and one for the backside lithography. The materials and parameters are summarised in Table 3.4.

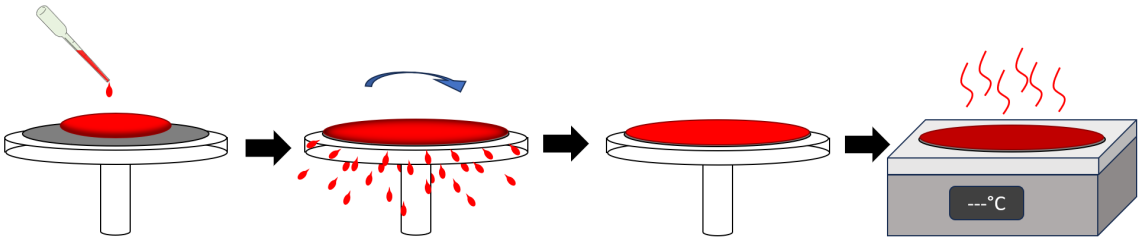

Figure 3.6 – Schematic of the spin-coating process : (i) dispense resist, (ii) spin, (iii) stop, (iv) solvent evaporation.

Step	Photoresist	Speed (rpm)	Acceleration (rpm/s)	Thickness (µm)
Device layer	S1813	4000	2000	1.3
Backside	AZ10XT	1000	500	12

Table 3.4 – Spin-coating parameters for the two lithography steps.

A positive resist (S1813) was spin-coated for the device-layer mask (target thickness $\approx 1.3\ \mu\mathrm{m}$), while a thick positive resist (AZ-10XT) was used for the backside (target thickness $\approx\ 12\ \mu\mathrm{m}$). The thick resist provides sufficient etch resistance for the subsequent deep reactive ion etching (DRIE).

3.3.3 . LITHOGRAPHY

After coating and soft-baking, photolithography was performed on an EVG620 mask-aligner. The photomask was aligned with the wafer in vacuum-contact mode to ensure accurate pattern transfer and minimise diffraction effects.

For the thin S1813 resist, an exposure dose of $\sim\ 120\ \mathrm{mJ/cm^2}$ was sufficient. For the thick AZ-10XT resist a higher dose of $\sim 900\,\mathrm{mJ/cm^2}$ was required to ensure full penetration through the $12\ \mu\mathrm{m}$ layer.

Following exposure, the wafers were developed in the appropriate developers (MF-319 for S1813, AZ-400K for AZ-10XT) until the exposed regions were completely removed, then rinsed with DI water and dried with nitrogen. Optical microscopy confirmed successful pattern transfer and good uniformity across the wafer.

3.3.4 . DRIE

The patterned photoresist served as the mask for the subsequent inductively coupled plasma/deep reactive ion etching (ICP/DRIE) of silicon. A Bosch-like cyclic process [91, 92] was used, alternating between an $\mathrm{SF_6}$ etch step (isotropic silicon removal) and a $\mathrm{C_4F_8}$ passivation step (fluorocarbon deposition). During each cycle the passivation layer at the trench bottom is removed by ion bombardment, suppressing lateral etching and yielding highly anisotropic profiles (see Figure 3.7).

Typical settings : ICP source power $2500\ \mathrm{W}$, bias power 50–$100\ \mathrm{W}$, pressure $50\ \mathrm{mTorr}$, and substrate temperature $0^{\circ}\mathrm{C}$ (helium backside cooling). These parameters give a high

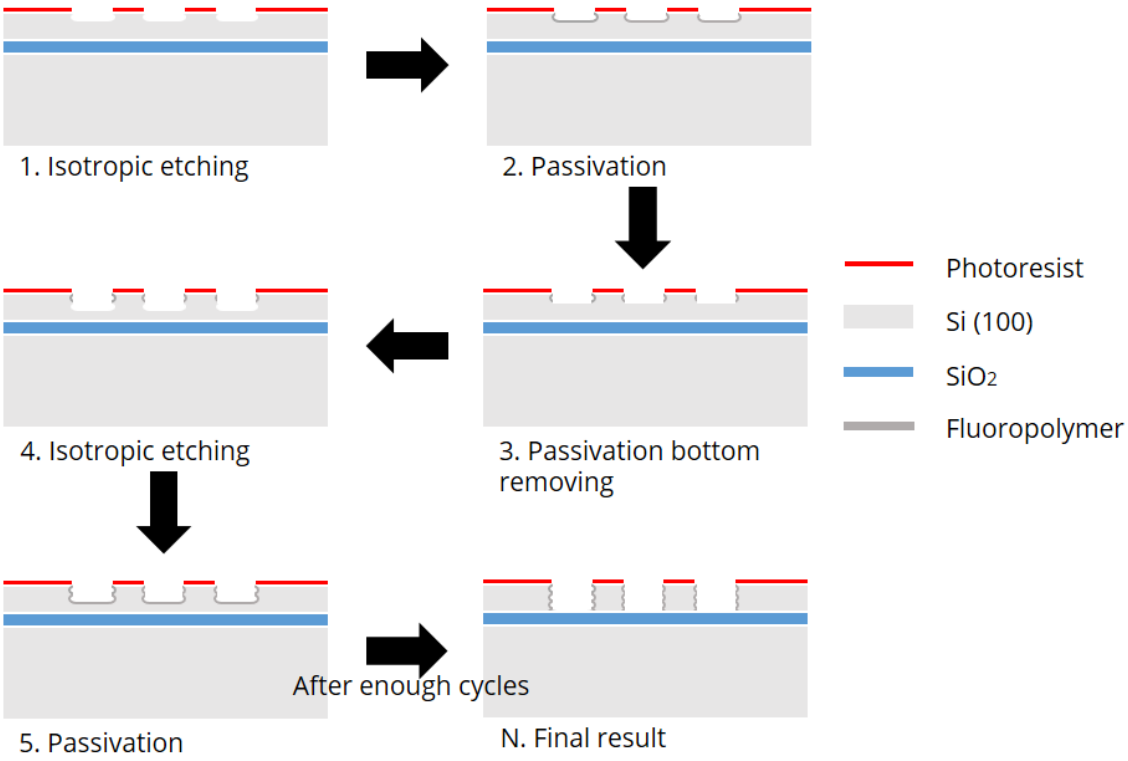

Figure 3.7 – Schematic of the ICP/DRIE process. A sufficient number of cycles is applied to etch silicon through til the SiO_2 layer.

silicon etch rate while maintaining vertical sidewalls and low surface roughness. After etching, the remaining photoresist was stripped with acetone and an oxygen plasma clean. The resulting structures exhibit nearly vertical sidewalls and high aspect ratios (up to $1:100$).

3.3.5 . XeF_2 ETCHING

Xenon difluoride (XeF_2) provides a dry, highly selective, isotropic etch of crystalline silicon. At room temperature the reaction :

$$\mathrm{Si\,(s)} + 2\,\mathrm{XeF_2\,(g)} \rightarrow \mathrm{SiF_4\,(g)} + 2\,\mathrm{Xe\,(g)} \tag{3.1}$$

proceeds spontaneously, producing volatile SiF_4 and elemental xenon. The silicon etch rate ($\approx\ 1\ \mu\mathrm{m/min}$) exceeds that of SiO_2 by two–three orders of magnitude, which is advantageous for improving HF access to the buried oxide without damaging the device layer.

We use pulsed XeF_2 cycles (10 s pulse followed by an N_2 purge) to obtain precise depth control. Each cycle removes a few micrometres; repeated cycles achieve the required tens-of-micrometres under-etch while preserving feature fidelity.

3.3.6 . METAL DEPOSITION

Metal layers were deposited to form the electrical interconnections and electrodes required for device operation. Physical vapour deposition (PVD) was carried out in an e-beam evaporator using a shadow mask fabricated from a double-side-polished silicon wafer (lithography + DRIE). After alignment, the mask and the sample wafer were temporarily bonded with a removable oil.

First, a $10\ \mathrm{nm}$ titanium adhesion layer was deposited, followed by a $100\ \mathrm{nm}$ gold layer to provide low-resistance, chemically stable electrodes. Deposition was performed under high vacuum; the rate was carefully controlled to minimise internal stress and ensure uniform film thickness. The resulting electrodes exhibit good adhesion, uniform coverage and well-defined geometry, suitable for subsequent electrical characterisation.

3.3.7 . CLEANING

A thorough cleaning is required before the HF release, because the narrow gaps must remain free of contaminants to allow HF to reach the buried oxide. A hydrophilic surface promotes the HF reaction (see Equation (3.2)).

We employ a piranha solution ($3:1\,H_2SO_4:\,H_2O_2$) to remove organic residues. Wafers are immersed at an elevated temperature for $\sim 5\ \mathrm{min}$, then thoroughly rinsed in DI water and dried with nitrogen. Although piranha leaves a thin native oxide, this oxide is later removed during the HF release step.

3.3.8 . HF RELEASE ETCHING

The MEMS structures are released by selectively etching the buried oxide (BOX) layer with hydrofluoric acid (HF). Because HF attacks SiO_2 much faster than silicon, the device layer remains intact while the BOX is removed.

$$\mathrm{SiO_2} + 6\,\mathrm{HF} \rightarrow \mathrm{H_2SiF_6} + 2\,\mathrm{H_2O} \tag{3.2}$$

Two release methods were employed : wet HF and vapor HF.

WET HF

Wafers were immersed in a 50% HF solution for $\sim 30\ \mathrm{min}$. Lateral etching proceeds from the exposed BOX regions, achieving an under-etch distance of roughly $30\ \mu\mathrm{m}$. After etching, the wafers are rinsed in DI water and IPA, then dried with nitrogen. Special care is taken during drying to avoid stiction caused by capillary forces.

VAPOR HF (VHF)

To further reduce stiction, a vapor-phase HF process was performed at $\sim 40^{\circ}\mathrm{C}$ for $\sim 2\ \mathrm{h}$ [93]. The vapor etch provides lateral under-etch depths of 30–$50\ \mu\mathrm{m}$. Although the etch rate is slower and less stable than the wet process, VHF eliminates liquid-phase capillary forces, dramatically decreasing the risk of structure collapse for high-aspect-ratio devices.

3.3.9 . SIMPLIFIED FABRICATION PROCESS

Before implementing the full device structure, a simplified process was developed to verify the feasibility of fabricating the MEMS bell plate on an SOI substrate. The goal of this preliminary device was to demonstrate mechanical functionality (structural integrity, vibration capability, and release) without the added complexity of electrical detection.

To minimise process steps, backside etching was omitted. In the final design, backside etching is used to optimise the electrode layout, but for the initial mechanical tests it is unnecessary. The simplified flow is shown in Figure 3.8.

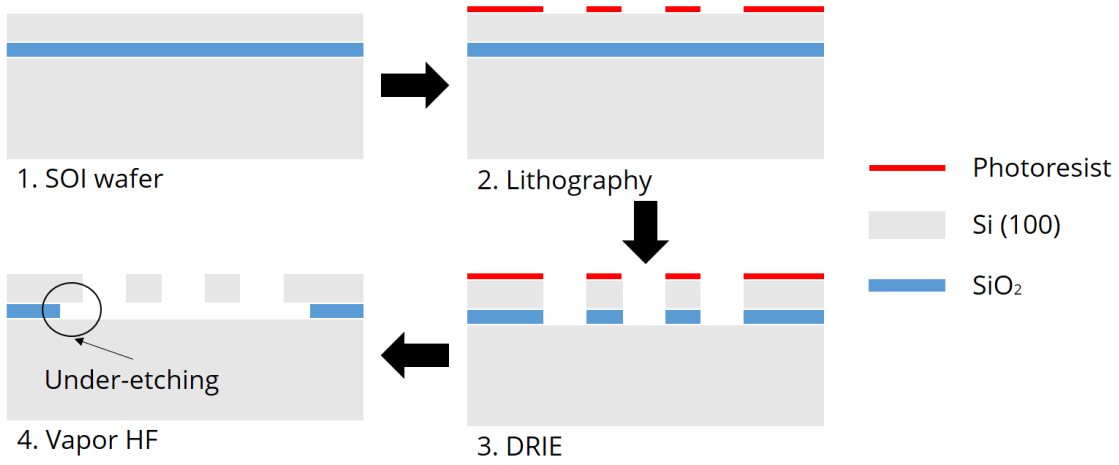

Figure 3.8 – Simplified fabrication flow (no backside etching).

A major challenge in the release step is the long lateral under-etch distance required to free the suspended structure. To guarantee complete release, the under-etch should be at least $200\ \mu\mathrm{m}$ (the radius of the inner circle of the bell plate). To reduce this distance, a set of release holes was added (see Figure 3.9). The holes (radius $33\ \mu\mathrm{m}$, centre-to-centre spacing $80\ \mu\mathrm{m}$) allow HF to access the buried oxide more efficiently, decreasing the required under-etch depth to roughly $40\ \mu\mathrm{m}$.

Including these release holes markedly lowers the probability of incomplete release and improves overall yield. Using this simplified flow, suspended MEMS bell plates were

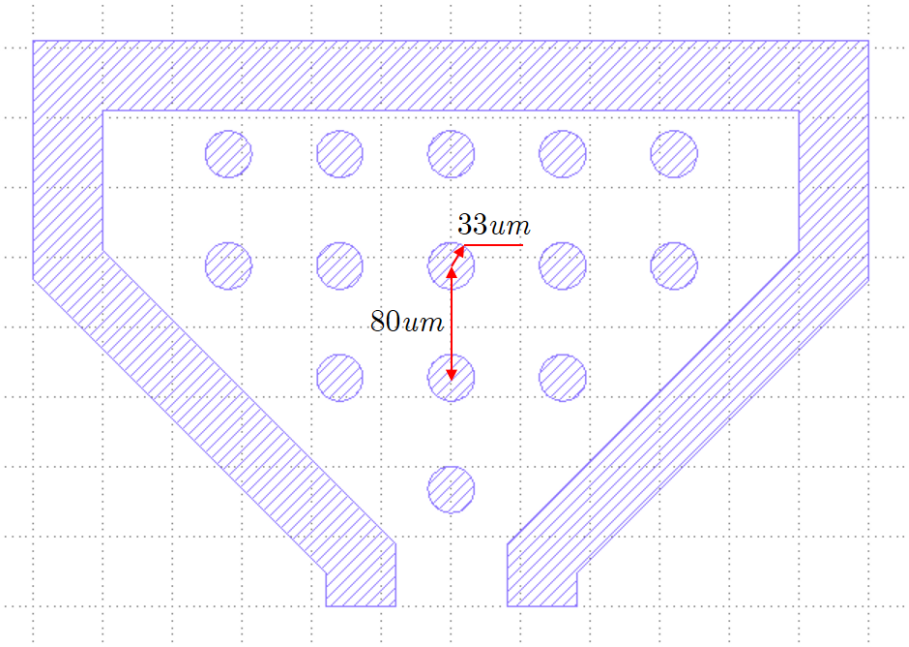

Figure 3.9 – Mask layout of the bell plate with release holes (shaded area to be etched).

successfully fabricated on the SOI wafer, confirming the viability of the structural design and process.

3.4 . SCANNING ELECTRON MICROSCOPE (SEM) PHOTOS

After fabrication, samples from the two processes were examined with a scanning electron microscope. This section presents representative SEM images to assess fabrication quality.

Figure 3.10 shows a sample fabricated by the simplified process (Figure 3.8) on a low-doped SOI wafer. Figure 3.11 displays a sample fabricated by the full process (Figure 3.5) on the same wafer type. High-doped wafers exhibit a rougher surface (see Figure 3.12) and a noticeable colour change (Figure 3.13), which suggests a lower Q compared with low-doped wafers.

The defect may due to galvanic corrosion which is an electrochemical process that oxidized than then corroded by HF. We still need further more experiment to validate our hypothesis. Nevertheless, high-doped wafers are required to validate electrical detection because low-doped material suffers from high resistance and strong Schottky-contact rectification, which impede current flow. Consequently, both wafer types are studied : the low-doped samples for mechanical performance (Chapter 4) and the high-doped samples for electrical detection (Chapter 5). More detailed SEM photos are illustrated in Appendix A.

3.5 . CONCLUSION

A self-consistent design-fabrication methodology for microscopic silicon bell plates has been demonstrated. By fixing the aspect-ratio W/L and iteratively tuning the tang

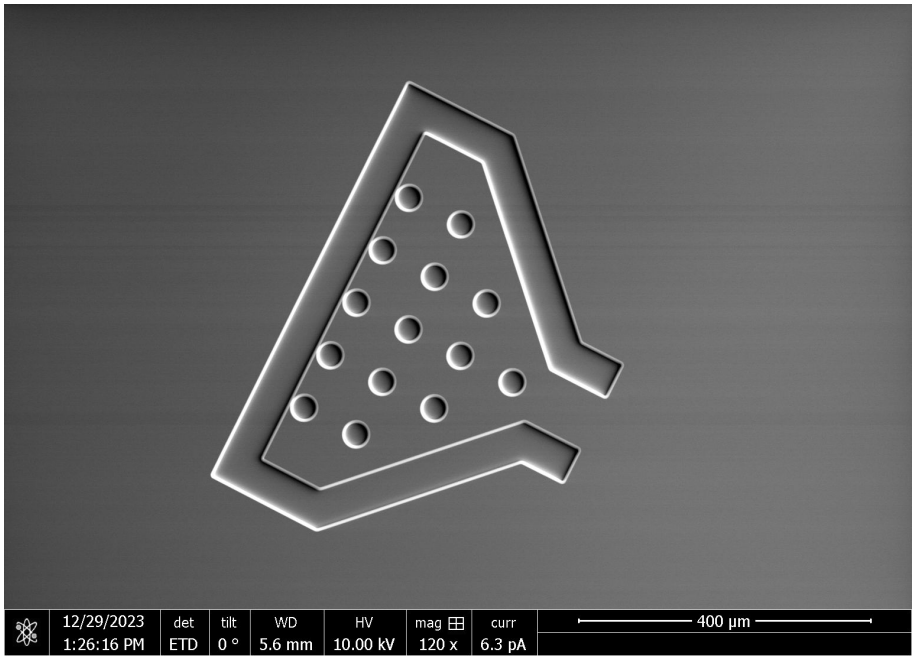

Figure 3.10 – SEM micrograph of a sample fabricated by the simplified process.

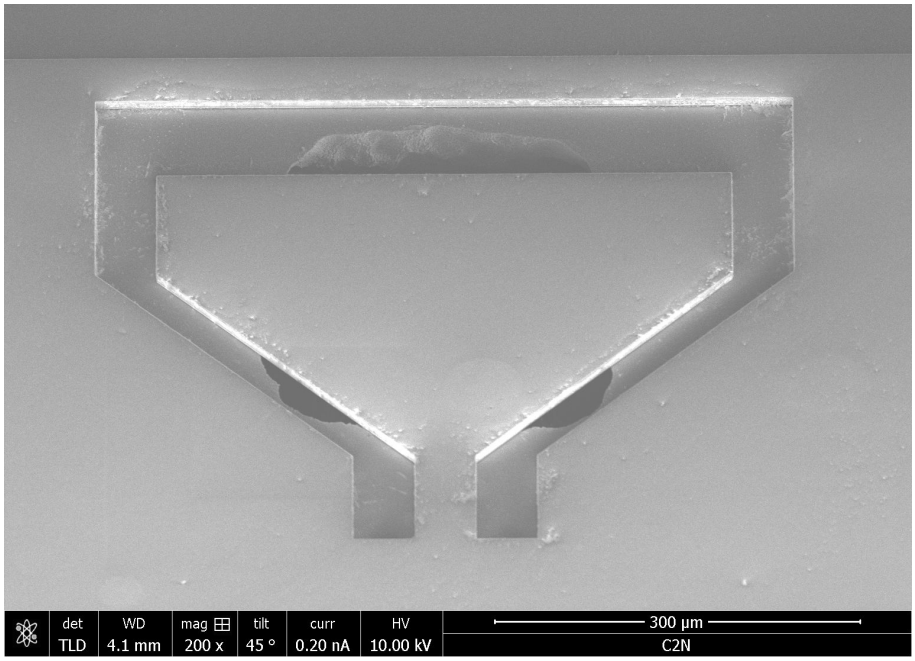

Figure 3.11 – SEM micrograph of a sample fabricated by the optimized process (with back-side release hole).

(a)

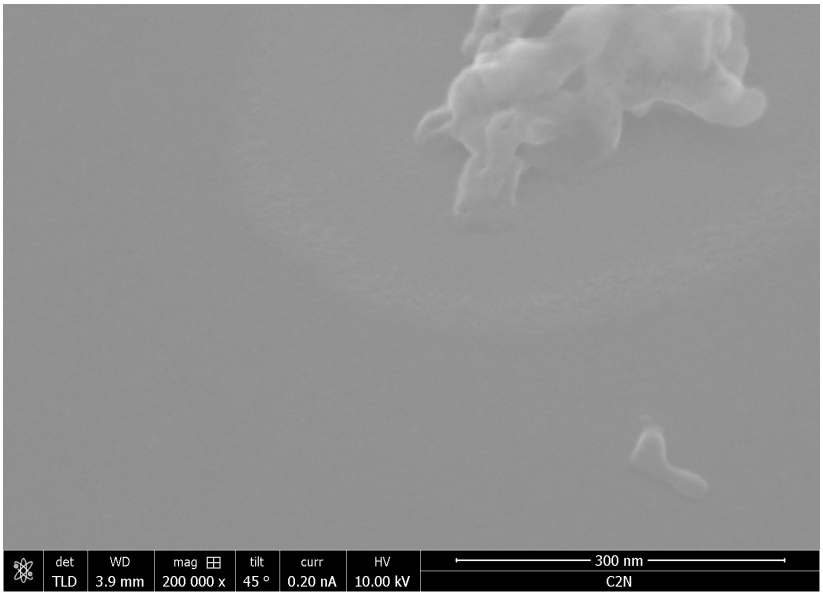

(b)

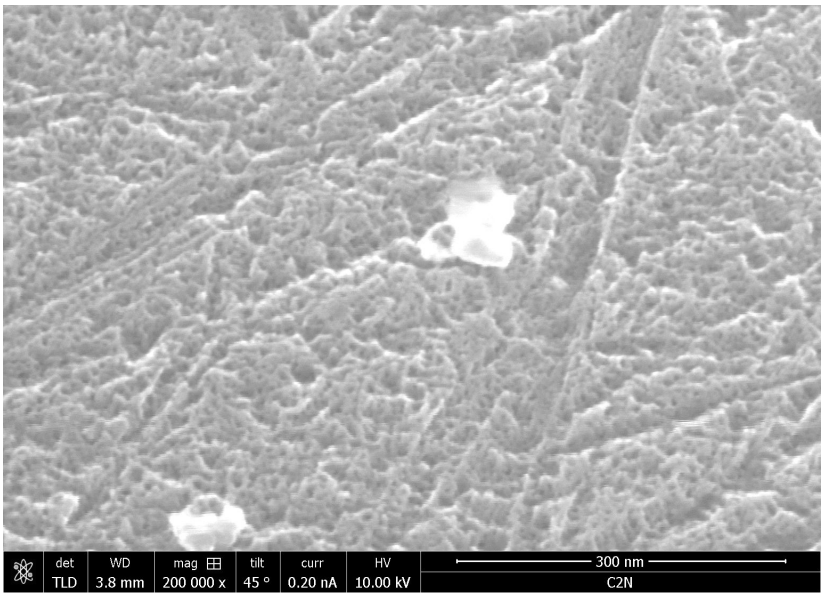

Figure 3.12 – SEM micrographs comparing the surface of device after fabrication : (a) low-doped wafer, and (b) high-doped wafer.

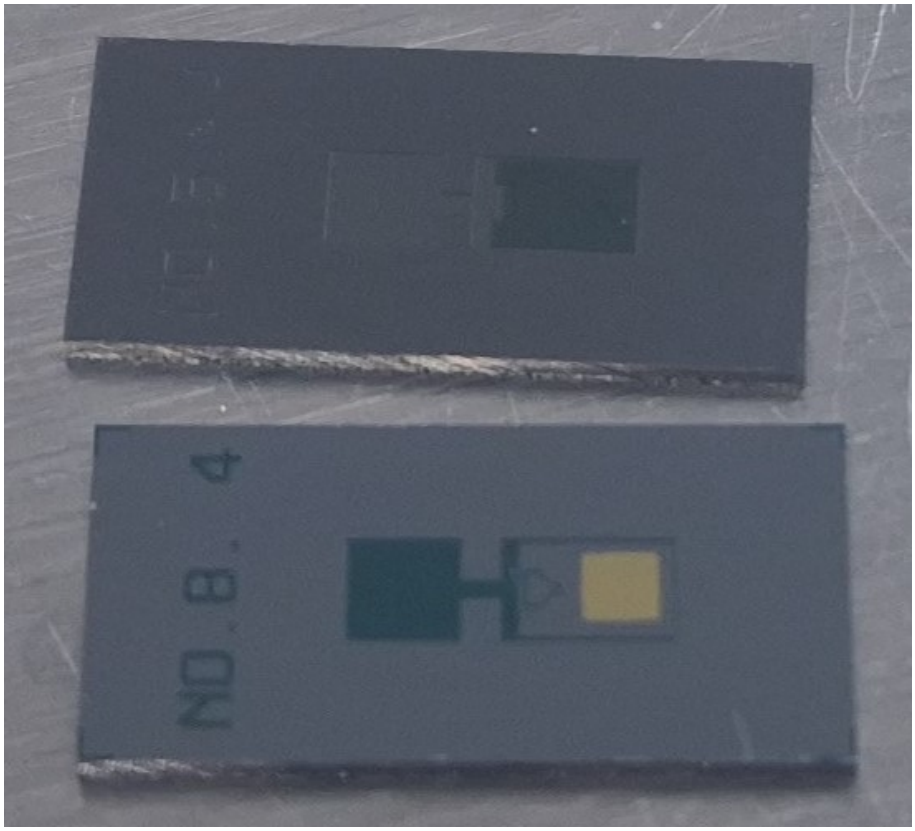

Figure 3.13 – Optical comparison of two samples before and after HF release. Both come from the same wafer. Upper : after release (silicon appears darker); Bottom : before release (silicon-oxide layer appears darker).

dimensions, plate thickness, and edge length L_e, we obtained a family of devices that simultaneously satisfy the targeted resonant frequency ($\approx 200kHz$), a high anchor-loss limited quality factor ($Q_{anchor} > 10^5$), and the stringent dimensional tolerances required by SOI MEMS processing.

The complete micro-fabrication flow—UV lithography, Bosch-type DRIE, isotropic $\mathrm{XeF_2}$ under-etching, and HF release—proved compatible with SOI wafers. A simplified process introducing release holes dramatically reduced the lateral under-etch distance, enabling reliable release of large-area plates without backside etching step and avoid stiction. SEM inspection confirmed that the designed geometries were faithfully reproduced, while the comparison between low- and high-doped wafers highlighted our notice on the impacts of Q for high-doped device.

Overall, the work bridges the gap between macroscopic analytical models and real micro-fabricated MEMS resonators, providing a practical guideline for engineers aiming to implement high-Q bell-plate devices in integrated SOI platforms. The mechanical characterisation presented in Chapter 4 and the electrical detection experiments in Chapter 5 further demonstrate that the fabricated resonators meet the original specifications, thereby validating the proposed design strategy.

4 - CHARACTERIZATION OF MEMS BELL PLATE SYSTEM

4.1 . INTRODUCTION

As demonstrated in previous chapter 3, a simple fabrication process was applied to obtained devices with various geometric design by using low-doped SOI wafer (material properties listed in Figure 3.2). A variety of samples can achieve a high quality factor in simulations. Hence, the dimensions presented in Table 4.1 were therefore selected from a broader set of feasible configurations, specifically those compatible with our fabrication process and successfully realized experimentally.

Some defects were expected during the manufacturing process such as a variable lateral under-etching of the silicon oxide layer which varies according to the duration of the HF release. An image of a MEMS bell plate under optical microscope is given in Figure 4.1. The exact geometric parameters were slightly different from the desired value. The clamping position deviates by approximately $40\mu m$ to $65\mu m$ from its intended position, affecting anchor losses. These defects were included in the simulations presented in section 4.2. Samples 2.1 and 2.2 were intentionally designed with identical nominal dimensions ; however, fabrication-induced variations resulted in sufficiently distinct structures to enable a meaningful comparative analysis.

This chapter presents a comprehensive characterisation of the microscopic silicon bell-plate resonators. First, finite-element simulations are used to evaluate the modal frequencies and the anchor-loss limited quality factors (Q_{anchor}). The influence of geometric parameters (tang length, plate length, edge length) and of modelling choices (under-etch depth, PML thickness) is discussed.

Next, the static properties of the fabricated devices are examined. White-light interferometry provides the three-dimensional surface profile, allowing us to quantify the slight upward tilt that appears at room temperature. Mechanical probing is then employed to extract the stiffness of the first bending mode, which is compared with FEM predictions.

The dynamic behaviour is investigated in several stages. The experimental set-up (electrostatic actuation, differential laser-Doppler vibrometry, vacuum environment) is described, followed by the extraction of resonant frequencies and quality factors from Lorentzian fits of the frequency-response curves. The temperature coefficient of frequency (TCF), the dependence of resonance on DC bias, and the effect of ambient pressure on Q are all reported.

Overall, the chapter combines numerical modelling with a series of static and dynamic measurements in order to validate the design methodology, identify the dominant loss mechanisms, and assess the practical limitation of the bell-plate resonators.

4.2 . SIMULATION OF MEMS BELL PLATE

To improve the accuracy of the energy-dissipation model at the clamped end, a perfectly-matched layer (PML) boundary condition was applied. The PML absorbs outgoing waves and eliminates any energy reflection. Table 4.2 summarises the modal-simulation results, including the resonant frequencies and the anchor-loss quality factors Q_{anchor}.

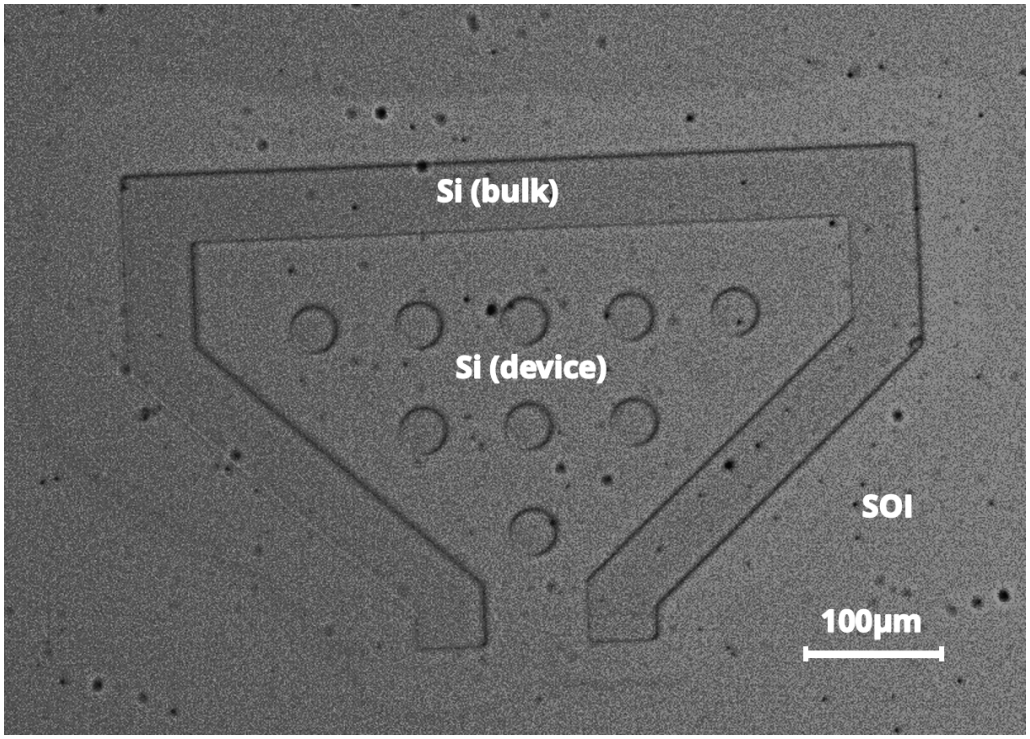

Figure 4.1 – Optical microscopy image of a MEMS sample. The under-etching area is brighter than its surrounding area.

Sample	Wt	W	Lt	L	Le
1	40 (40)	498 (500)	45 (45)	230 (230)	97 (100)
2.1	40 (40)	499 (500)	45 (45)	230 (230)	84 (84)
2.2	40 (40)	501 (500)	46 (45)	230 (230)	86 (84)
3	40 (40)	498 (500)	64 (65)	250 (250)	87 (90)

Table 4.1 – Geometric parameters of the samples after fabrication measured by optical microscopy and comparison with design expectations written in parenthesis. Dimensions are in microns.

The first bending mode resonates at roughly 20 kHz, whereas the (2,0)-mode is centred around 190 kHz. The simulated Q_{anchor} for the (2,0)-mode (see Figure 4.2) exceeds 2.2×10^5 and is consistently higher than that of the first bending mode. Although the three samples have very similar dimensions, their quality factors differ markedly, especially for the (2,0)-mode. This underlines the strong sensitivity of that mode to the tang length (L_t), plate length (L) and edge length (L_e). The two best samples (2.2 and 3) exhibit Q_{anchor} values of 186 k and 224 k, respectively.

The Q-factor obtained from FEM simulations is highly sensitive to the amount of under-etching and to the thickness of the PML. To enable a fair comparison, all three samples were simulated with the same under-etch depth of $45\ \mu$m, which matches the observation under the microscope (see Section 4.3.1). The PML thickness was set to $30\ \mu$m because this value gave the best agreement with the experimental results for Sample 1, despite the difficulty of estimating the reflection ratio *ab initio*.

Additional FEM simulations performed with a dedicated thermo-elastic-damping mo-

Sample	First mode		(2,0)-mode	
	f (kHz)	Q_{anchor} ($\times 10^3$)	f (kHz)	Q_{anchor} ($\times 10^3$)
1	19.8	61.1	188.8	110
2.1	20.3	60.1	193.4	101
2.2	19.1	59.3	189.5	186
3	18.8	65.8	192.4	224

Table 4.2 – Simulation results for the actual dimensions of the samples given in Table 4.1.

dule (CoventorWare) predict a thermo-elastic quality factor Q_{TED} ranging from 150 k to 400 k, depending on the exact mode frequency, material parameters and plate geometry.

The resonant frequency of the first bending mode follows the expected trend with plate length L : like a rectangular cantilever beam, its frequency decreases as L increases. In contrast, the (2,0)-mode frequency stays within $\pm 5\%$ of 191 kHz and shows no clear monotonic dependence on L. FEM results indicate that the (2,0)-mode frequency is governed primarily by the plate width rather than its length, which is consistent with the mode shape.

4.3 . STATIC MEASUREMENTS

4.3.1 . SURFACE PROFILE

The geometry of the MEMS devices was first characterised by white-light interferometry [94] using a Fogale Nanotech™ M3D profilometer. Figure 4.2a shows a three-dimensional view of a bell-plate sample ; the corresponding cross-section taken along the plate bisector is displayed in Figure 4.2b. The measured shape agrees well with the design, except for a slight upward tilt of about 0.1°. This tilt is observed on all samples at 25°C.

To explain the phenomenon, we performed coupled thermal–mechanical FEM simulations of the entire 5 mm $\times\, 5$ mm die. The results (Figure 4.3) reveal that the tilt originates from thermal stress caused by the mismatch in the coefficient of thermal expansion (CTE) between the silicon device layer and the buried oxide. Experiments show that the tilt diminishes at lower temperatures and nearly vanishes at 0°C ; at still lower temperatures the plate tilts downwards.

4.3.2 . STIFFNESS

The stiffness was measured with a FemtoTools mechanical probe. The probe, positioned at the plate edge, was approached under computer control while the applied force was recorded. A linear fit of the force–displacement curve (Figure 4.4) yields a stiffness of approximately 10 N/m for the first bending mode. This experimental value is close to the FEM prediction of about 12 N/m, confirming that the plate has been fully released and that the measured stiffness is slightly lower than the simulated one, which explains the modestly lower resonant frequency observed experimentally.

4.4 . DYNAMIC MEASUREMENTS

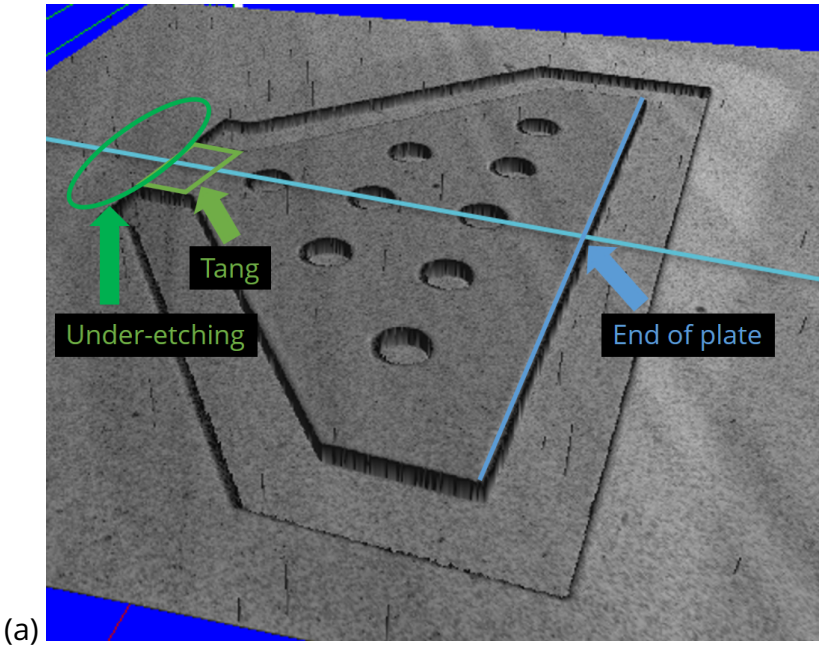

(a)

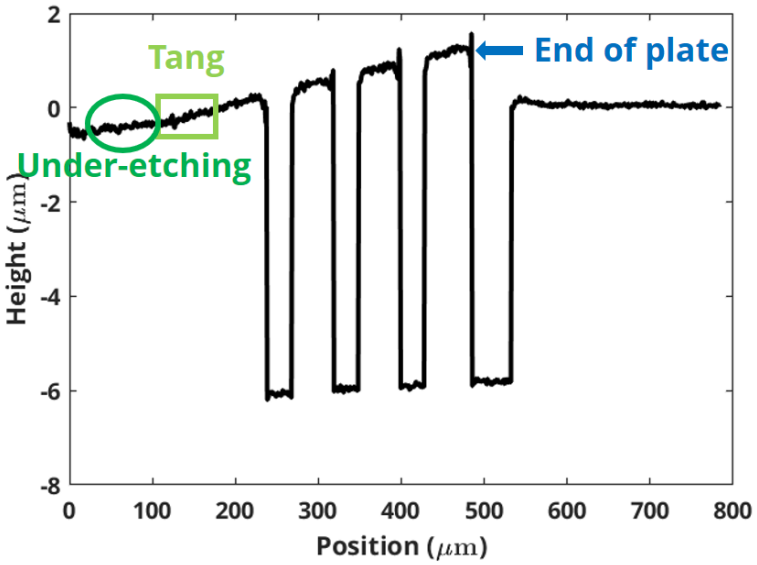

(b)

Figure 4.2 – Profile of a sample at $25°$C. (a) 3D profilometry of the MEMS bell plate (the blue line indicates the cross-section position). (b) 2D height profile taken along the bisector.

4.4.1 . INSTRUMENTS AND SETUP CONFIGURATION

Figure 4.5 depicts the experimental arrangement for dynamic testing. The devices were driven electrostatically, and their motion was detected with a Polytec™ OFV-552 differential fibre-laser Doppler vibrometer mounted on an Olympus BXFM microscope equipped with a $20\times$ variable-compensation objective. To maximise the air-quality factor Q_{air} by minimising viscous damping, the samples were placed in a micro-probe vacuum chamber (co-designed with Nextron™) and pumped by a vibration-isolated HiCube Eco 80 system. Pressures as low as 5×10^{-3} Pa were achieved. Unless otherwise stated, all measurements were performed at $25°$C.

According to the simulated mode shape shown in Figure 2.2, the (2,0)-mode exhibits

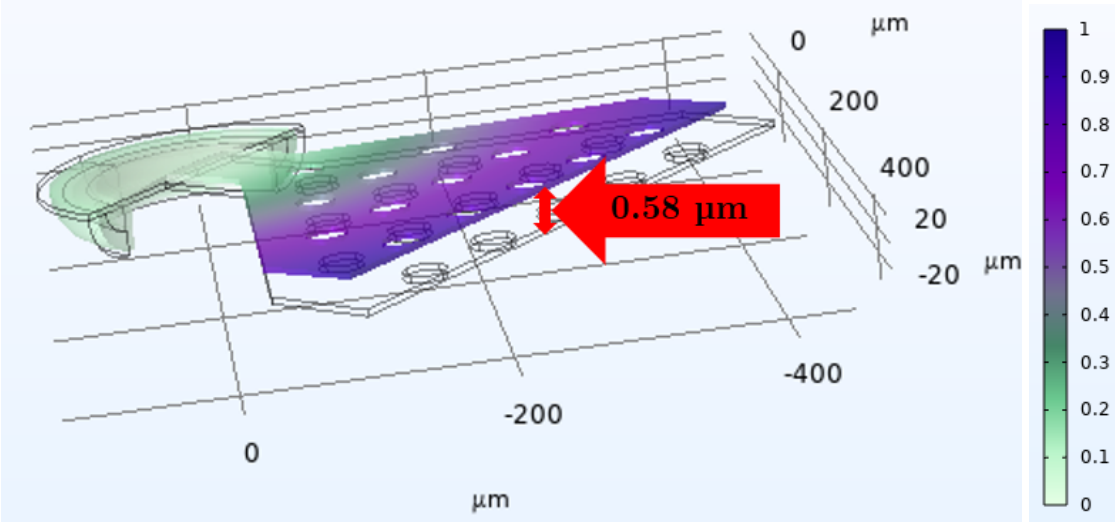

Figure 4.3 – Thermo-mechanical static simulation of a bell plate heated by $25°$C (reference temperature $0°$C). The colour bar indicates the normalised displacement amplitude.

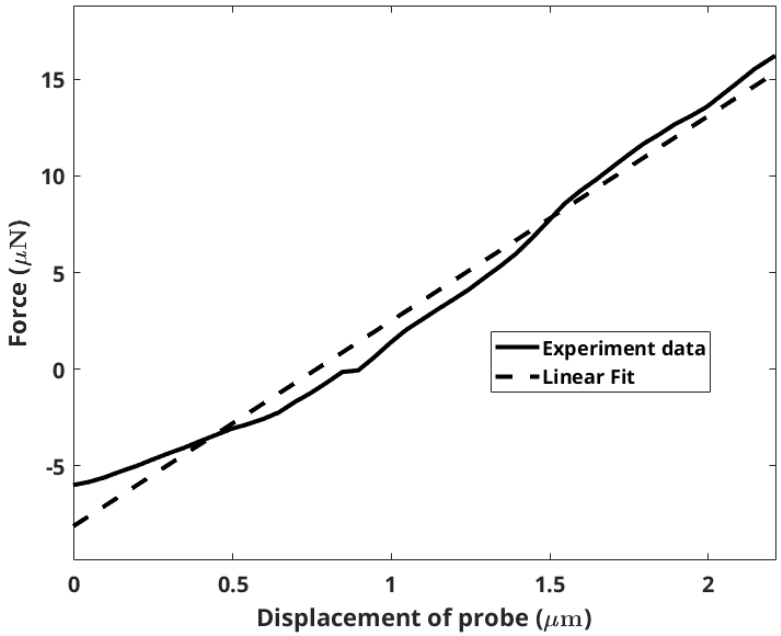

Figure 4.4 – Static force-displacement characteristic recorded using FemtoTools test bench, along with a linear fit with slope of $10.621 N/m$.

its largest amplitude at the plate corners. Consequently, the measurement laser spot was focused on a corner while the reference spot was placed on the surrounding SOI wafer. A differential velocity measurement was performed between the two spots. The device was excited with a sine-wave voltage (superimposed on a DC bias) close to its resonance. First, a phase-locked loop (PLL) implemented on a Liquid Instruments™ Moku :pro was used to drive the resonator at resonance; subsequently, the open-loop frequency response was recorded. Because the upward tilt described in Section 4.3.1 varies slightly from sample to sample, the AC drive amplitude was adjusted for each device while keeping the DC

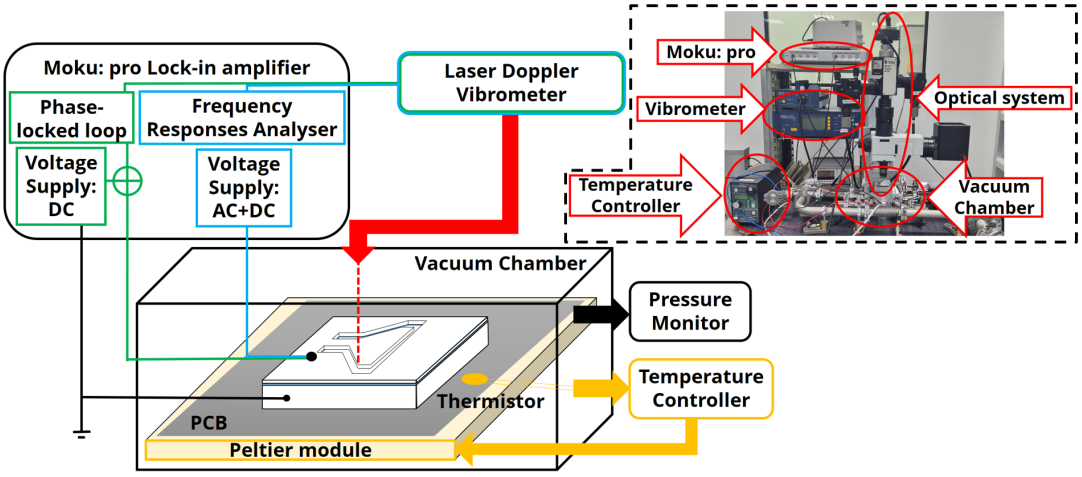

Figure 4.5 – Schematic of the experimental setup. Green lines : closed-loop control ; blue lines : open-loop excitation ; yellow line : temperature-control system ; red line : laser beam from the vibrometer.

Sample	First mode			(2,0)-mode		
	f (kHz)	Q ($\times 10^3$)	$f \times Q$ (GHz)	f (kHz)	Q ($\times 10^3$)	$f \times Q$ (GHz)
1	19.9 (19.8)	63.0 (61.1)	1.25 (1.21)	184.5 (188.8)	100 (110)	18.4 (20.8)
2.1	20.6 (20.3)	68.4 (60.1)	1.41 (1.22)	192.2 (193.4)	103 (101)	19.8 (19.5)
2.2	17.1 (19.1)	56.8 (59.3)	0.97 (1.13)	178.8 (189.5)	132 (186)	23.6 (35.2)
3	16.6 (18.8)	71.6 (65.8)	1.18 (1.24)	180.6 (192.4)	140 (224)	25.3 (43.1)

Table 4.3 – Resonant frequency, quality factor and $f \times Q$ extracted from measurements at $25°$C on the four samples (values from FEM simulations are shown in parentheses).

bias constant at 750 mV. The AC amplitude never exceeded 250 mV, which is well below the static pull-in voltage (estimated at 7 V from electromechanical FEM simulations in the absence of tilt).

4.4.2 . FREQUENCY RESPONSE

Both the (2,0)-mode and the first bending mode were characterised. Representative frequency-response curves are shown in Figure 4.6. Each response follows a classic Lorentzian shape. The quality factor Q can be extracted by fitting the curve with the second-order resonator model

$$A^2 = \frac{G^2}{\left[(\omega/\omega_0)^2 - 1\right]^2 + (\omega/(\omega_0 Q))^2} \tag{4.1}$$

where A is the vibration amplitude, G the overall gain, ω_0 the resonant angular frequency and ω the excitation frequency [95]. Eight frequency responses (two modes for four samples) measured at ambient temperature were fitted, yielding the resonant frequencies and quality factors listed in Table 4.3. The complete data set of dimension is provided in Table 4.1.

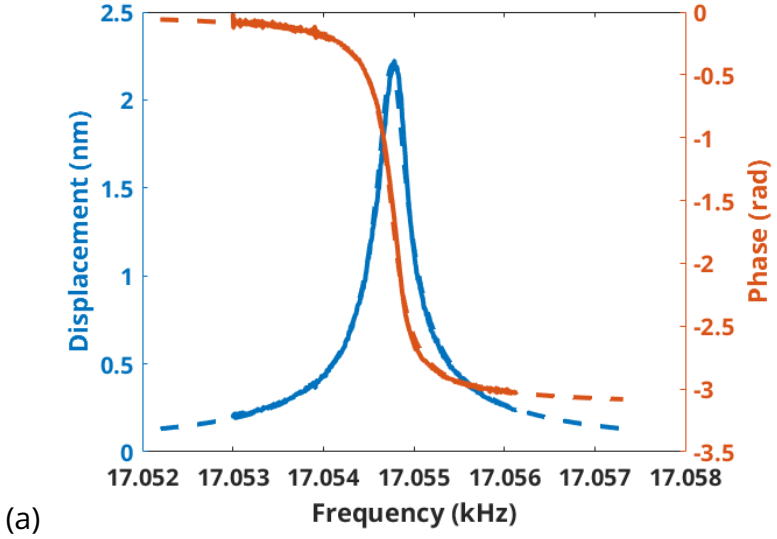

(a)

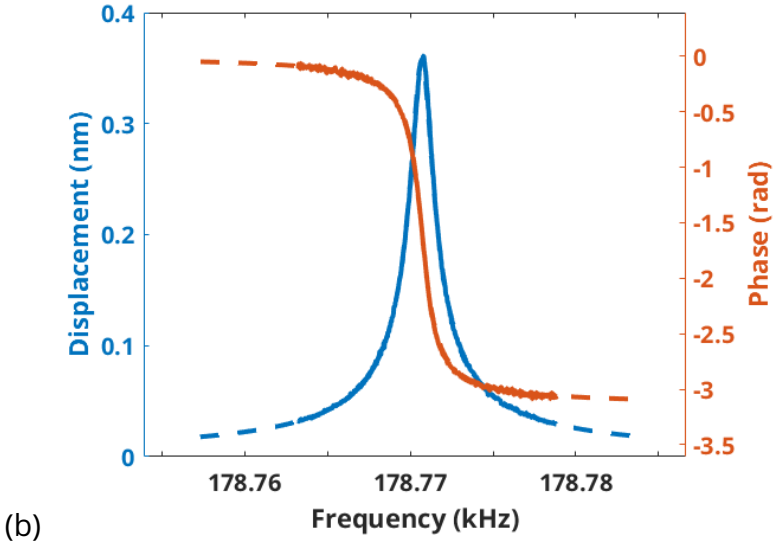

(b)

Figure 4.6 – Experimental frequency responses of Sample 2.2 (solid line : measured data ; dashed line : fitted Lorentzian). (a) First bending mode ; (b) (2,0)-mode.

For the first bending mode the measured Q is $68k \pm 7\%$ at a frequency near 20 kHz. Both resonant frequencies are in good agreement with the FEM predictions ; the discrepancies (ranging from 0.1% to 13%) can be attributed to uncertainties in silicon material properties, the exact amount of lateral oxide under-etch, thermal stress, and, to a lesser extent, the applied DC bias.

All Q-values for the (2,0)-mode are significantly larger than those of the first bending mode, confirming that the former is better suited for high-Q resonator applications. As predicted by the simulations, Samples 2.2 and 3 exhibit the highest Q, although the experimental values are roughly 40% lower than the anchor-loss Q predicted by FEM. The (2,0)-mode Q is extremely sensitive not only to the under-etch depth but also to the exact values of L_t and L_e. For example, changing L_e from $87\,\mu$m to $86\,\mu$m in Sample 3 reduces the simulated Q_{anchor} from 140 k to 127 k. Variations of the tang length on the order of $\pm 1\,\mu$m can cause Q_{anchor} to change by 10%–50%. Larger deviations without compensa-

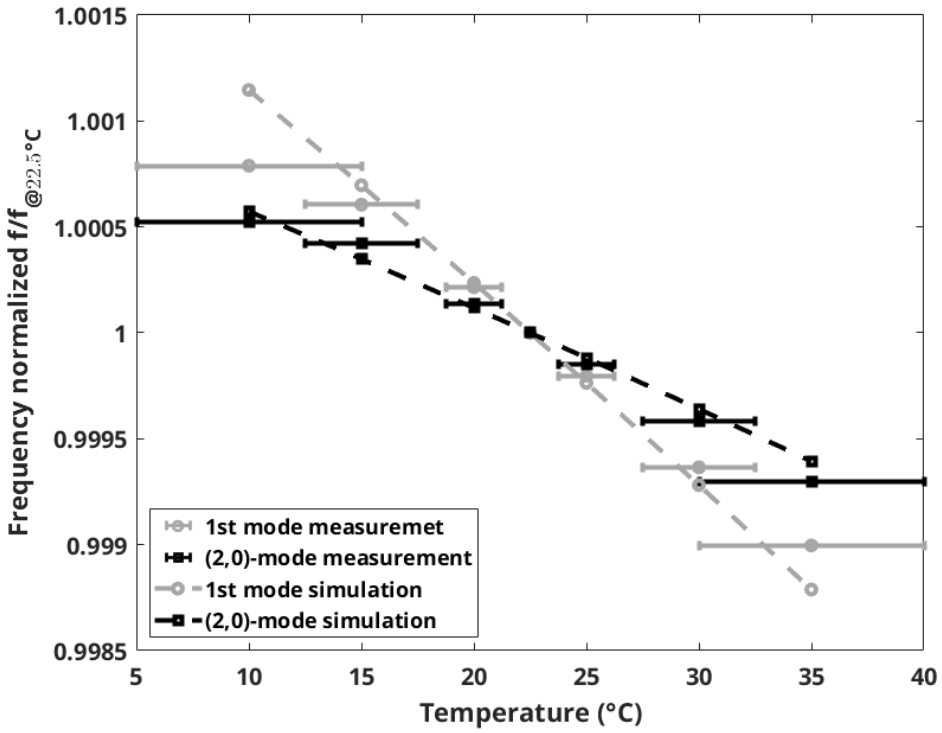

Figure 4.7 – Measured and simulated resonant frequencies of Sample 2.2 as a function of temperature (10–35°C).

ting adjustments to other dimensions would alter the mode shape dramatically and could lead to a severe reduction in Q_{anchor}. Consequently, precise control of L_t and L_e is essential for achieving high quality factors. Considering the thermo-elastic damping estimated from simulation, the measured Q may also be marginally limited by this mechanism.

4.4.3 . TEMPERATURE COEFFICIENT OF FREQUENCY (TCF)

The temperature coefficient of frequency (TCF) quantifies the thermal stability of a resonator. By operating the resonator in a closed-loop, we tracked the resonant frequencies of both modes while the temperature was varied from $10°$C to $35°$C. The normalised frequency versus temperature curves are shown in Figure 4.7. Because no on-die temperature sensor is available, the temperature was measured both with an external probe on the printed-circuit-board (PCB) surface and with the temperature controller that monitors the sample holder (see Figure 4.5). The actual die temperature is therefore bounded by these two measurements, which appear as error bars in the plot.

From the data we obtain a TCF of -48 ppm/°C$\pm 10\%$ for the (2,0)-mode and -85 ppm/°C$\pm$ 10% for the first bending mode.

Thermal expansion also modifies the plate tilt. As the temperature rises the upward tilt becomes more pronounced than the profile shown in Section 4.3.1. Simultaneously, the quality factor of the (2,0)-mode varies with temperature. FEM simulations (Figure 4.8) predict an optimal temperature at which Q reaches a maximum. The experimental data corroborate this prediction, with the highest Q observed near $15°$C for Sample 2.2, while Sample 3 exhibits its peak Q around $25°$C. The temperature dependence of Q stems from

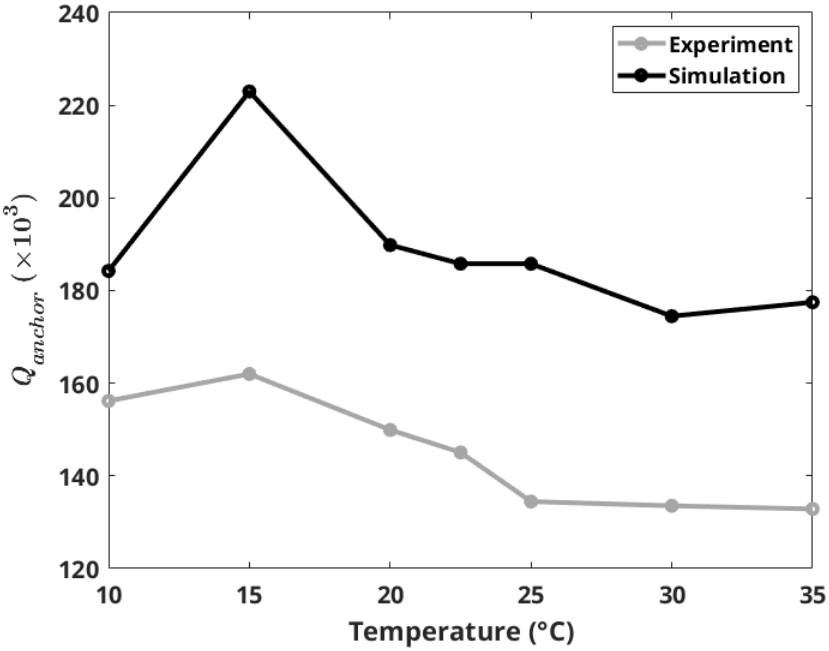

Figure 4.8 – Experimental (markers) and simulated (solid line) evolution of the (2,0)-mode Q versus temperature for Sample 2.2.

several mechanisms : geometric changes due to thermal expansion, tilt induced by CTE mismatch between silicon and silicon oxide, and possible material softening. All these effects alter the mode shape and, consequently, the quality factor.

4.4.4 . EVOLUTION OF RESONANT FREQUENCY AND Q WITH DC BIAS

When a DC bias is applied, electrostatic forces modify the effective stiffness of each mode according to :

$$k_{\text{eq}} = k + k_e \tag{4.2}$$

where $k_e < 0$ is the electrical stiffness, which scales with the square of the bias voltage V_b^2 and a mode-specific transduction coefficient η_i [95]. Consequently, the resonant frequency follows :

$$f^2 = f_0^2\left(1 - \eta_i V_b^2\right) \tag{4.3}$$

as illustrated in Figure 4.9. By fitting the measured frequency-bias curves, we extracted η values of $0.05\ \text{V}^{-2}$ for the first bending mode and $1.7 \times 10^{-4}\ \text{V}^{-2}$ for the (2,0)-mode. The upward tilt described in Section 4.3 slightly alters these coefficients, leading to a relatively low tunability of the (2,0)-mode frequency—a drawback for embedded-clock applications. This limited tunability originates from the current electrode geometry, which is optimised for the first bending mode but not for the (2,0)-mode. Redesigning the actuation electrodes (e.g., placing them near the plate corners) could increase the transduction coefficient of the (2,0)-mode while reducing the risk of pull-in.

The quality factor also depends on the bias voltage (Figure 4.10). For the first bending mode, Q drops sharply at low bias and then decays more gradually, reaching only

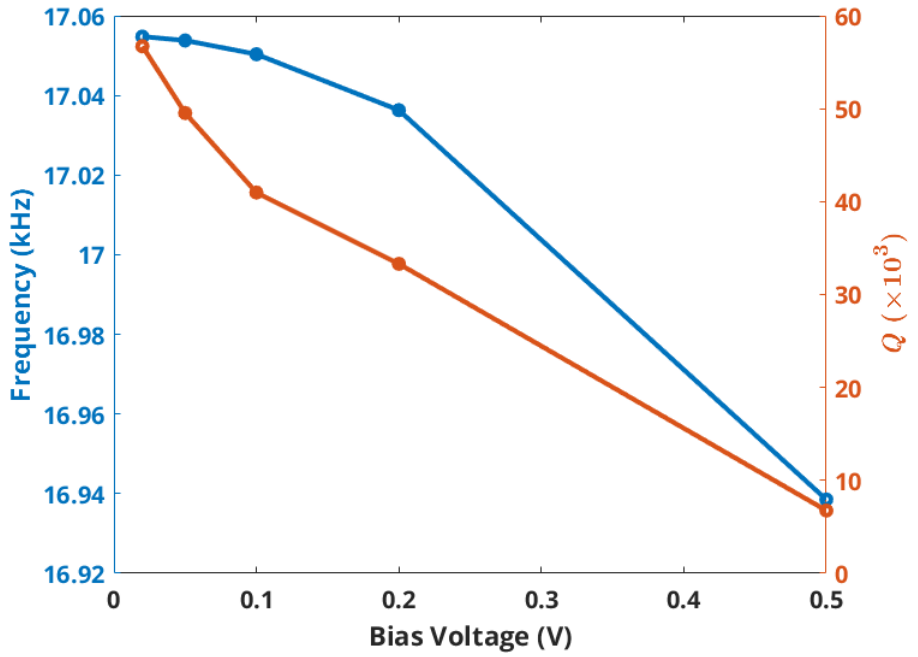

(a)

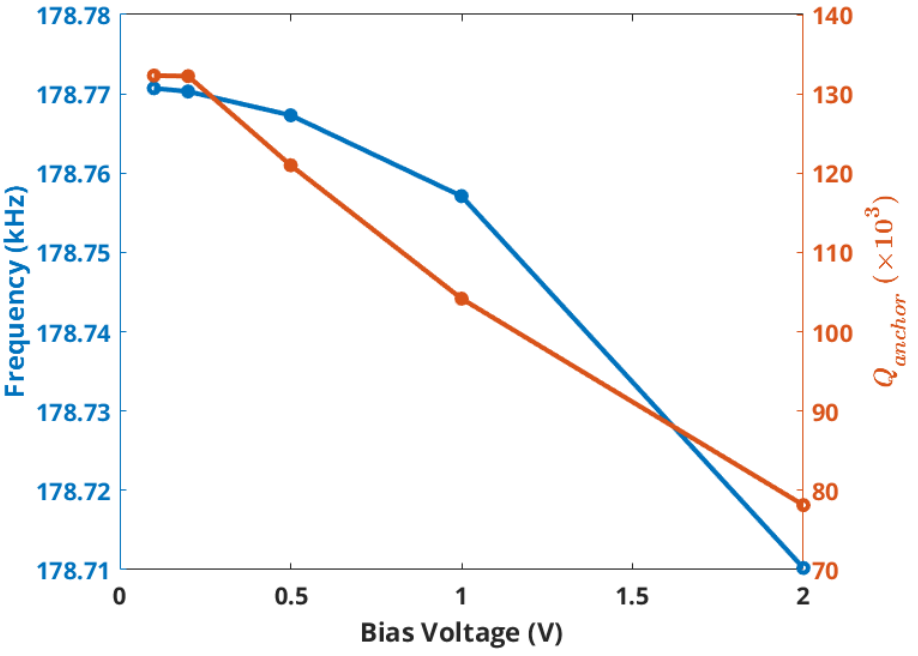

(b)

Figure 4.9 – Experimental evolution of resonant frequency and Q for Sample 2.2 as a function of DC bias voltage. (a) First bending mode; (b) (2,0)-mode.

about 20% of its zero-bias value at 0.5 V. By contrast, the (2,0)-mode retains a Q above 120 k up to 0.5 V. Bias-induced Q degradation has been reported for other MEMS resonators and is attributed to several mechanisms [95, 96, 97]. Determining the dominant cause—especially the differing behaviour of the two modes—remains an open question that warrants further investigation.

4.4.5 . EVOLUTION OF Q WITH AMBIENT PRESSURE

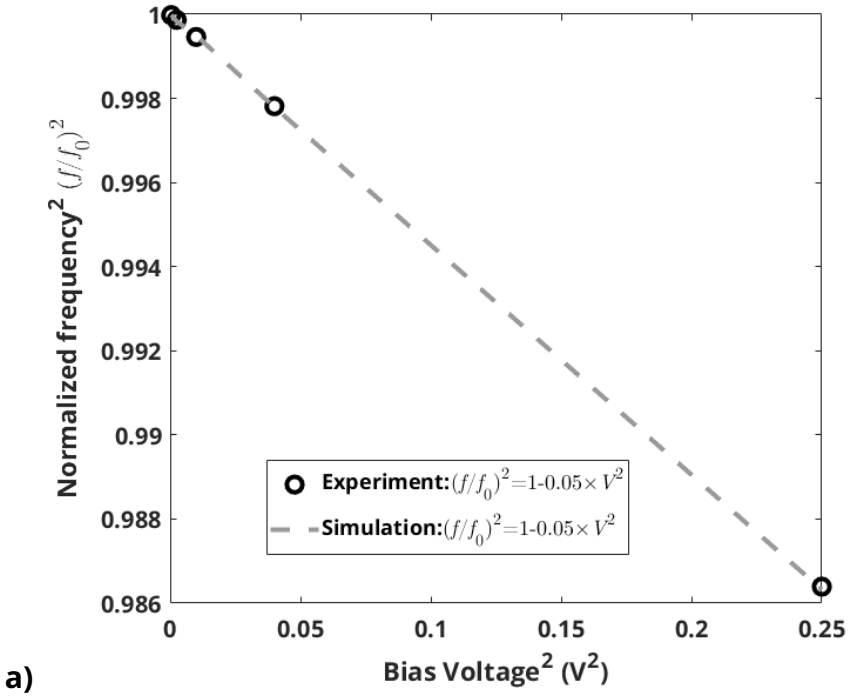

a)

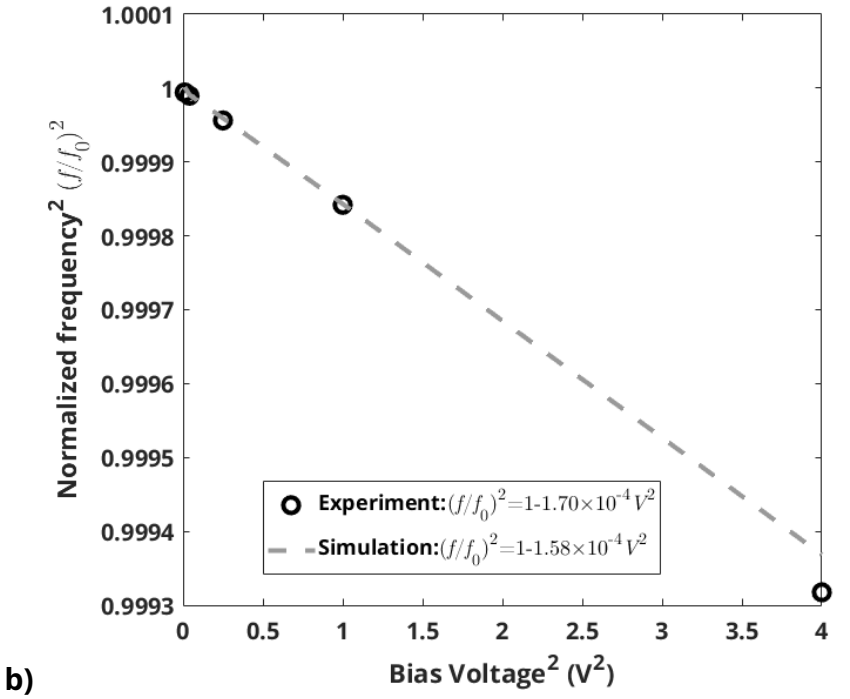

b)

Figure 4.10 – Normalized resonant frequency (solid symbols) and quality factor (open symbols) versus DC bias for Sample 2.2 at $25°$C.

Sample 2.2 was also characterised under different pressures. Nitrogen was gradually introduced into the vacuum chamber to raise the pressure while the DC bias was kept constant and the AC drive adjusted to maintain a constant vibration amplitude at resonance. The quality factor was extracted from Lorentzian fits of the open-loop responses

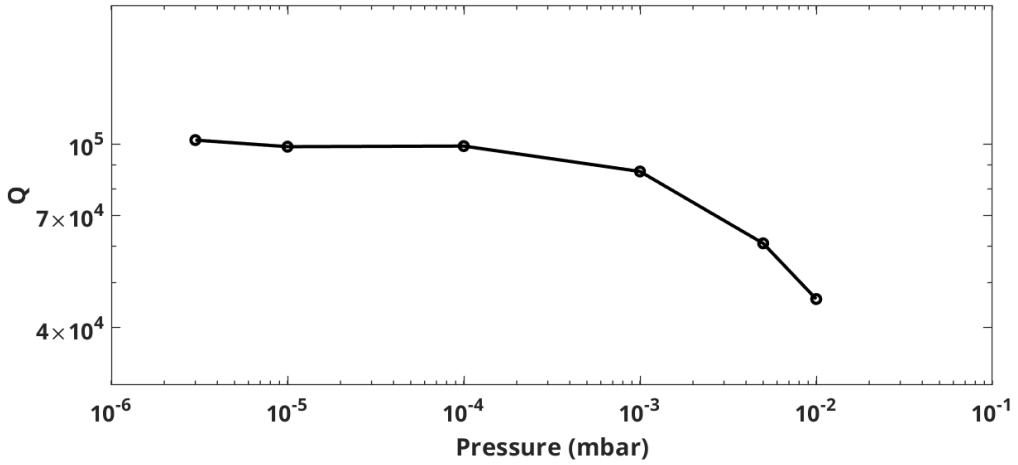

Figure 4.11 – Measured Q of the (2,0)-mode as a function of nitrogen pressure.

(Figure 4.11).

Q remains essentially unchanged up to about 10^{-2} Pa, then decreases slightly in the 10^{-2}–10^{-1} Pa range and drops more rapidly at higher pressures. This behaviour can be explained by a combination of viscous damping and squeeze-film damping. Given the small $1\ \mu$m gap and the relatively large plate area, squeeze-film effects are expected to become dominant beyond a certain pressure threshold [98, 99]. Because our measurements were performed in the linear regime, we cannot unambiguously separate the contributions of viscous damping from those of squeeze-film damping.

4.5 . CONCLUSION

Table 4.4 compares our work with other timing elements operating below 1 MHz. The comparison highlights that our MEMS resonator exhibits a high figure of merit, particularly among devices with resonant frequencies below 500 kHz. In addition, our resonator requires a lower supply voltage, suggesting potential for reduced power consumption and improved overall performance. These results demonstrate the promise of developing this novel MEMS resonator into a fully integrated timing system.

The combined simulation-experiment investigation confirms that the (2,0)-mode of the silicon bell-plate offers a substantially higher anchor-loss limited quality factor than the first bending mode, reaching measured values up to $224\,$k (simulated $> 220\,$k). FEM analyses reveal that this mode is highly sensitive to the tang length L_t and edge length L_e; variations of only $\pm 1\ \mu$m in these dimensions can modify Q_{anchor} by 10%–50%. Accurate control of these geometric parameters, together with a well-defined under-etch depth, is therefore essential for achieving the targeted Q performance.

Static profilometry showed a reproducible upward tilt of about 0.1° at 25°C, which originates from thermal stress caused by CTE mismatch between silicon and the buried oxide. The tilt almost disappear at lower temperatures and reverses sign below 0°C, confirming the thermomechanical origin. Stiffness measurements ($\approx 10N/m$) are in good agreement with FEM predictions, indicating successful release of the structures.

Dynamic measurements demonstrated that the resonant frequencies of both modes

are within a few percent of the simulated values, while the quality factors of the (2,0)-mode remain an order of magnitude larger than those of the first bending mode. The temperature coefficient of frequency was measured as -48 ppm/°C for the (2,0)-mode and -85 ppm/°C for the first mode. Both the resonant frequency and Q exhibit a clear dependence on DC bias; the (2,0)-mode retains a high Q ($\approx 120k$) up to 0.5V, whereas the first mode degrades sharply with bias. Pressure sweeps showed that Q is essentially constant down to 10^{-2} Pa and then drops at higher pressures, consistent with the onset of viscous and squeeze-film damping.

In summary, the experimental results validate the FEM-based design strategy, identify the critical geometric tolerances required for ultra-high Q, and provide a realistic performance benchmark for future MEMS clock or sensor implementations based on the silicon bell-plate resonator. Further optimisation of the electrode geometry and tighter control of the under-etch process are expected to bridge the remaining gap between measured and simulated Q_{anchor} values.

Reference	Structure	Figure of merit $f \times Q$	Bias voltage	Dimension mm^2	Material	Frequency	Q-factor	Year
This work	Bell plate	$28GHz$	$0.5V$	0.5×0.3	Silicon	$190kHz$	$140k$	
[100]	lateral extensional mode	$116GHz$	$1V$	2.7×0.75	Silicon	$966kHz$	$120k$	2010
[101]	Fork	$27GHz$	$2.4V$	N/A	Silicon	$524kHz$	$52k$	2014
[102]	Double-clamped beam	$22GHz$	$3.6V$	0.4×0.2	Epitaxial polysilicon	$541kHz$	$42k$	2019
[103]	Double-Ended Tuning Fork	$7GHz$	$10V$	0.36×0.01	AlN on silicon	$600kHz$	$12k$	2015
[104]	BAW XTAL	$6GHz$	$3.6V$	0.6×1	Quartz	$131kHz$	$51k$	2013
[105]	Flexural plate	$1.6GHz$	$3.6V$	0.25×0.25	AlN on silicon	$32kHz$	$5k$	2012

Table 4.4 – State-of-the-art of high-Q resonators for timing references with resonant frequency below 1MHz

5 - ELECTRODE OPTIMIZED MEMS BELL PLATE

5.1 . INTRODUCTION

In the previous Chapter 4, we did characterization on the first fabrication patch of MEMS bell plate. The experiment verified the theory and function of bell plate (2,0)-mode of increasing the Q factor, especially compared to first bending mode. In consequence, it verified the possibility of MEMS bell plate fabrication. However, the method of detection can be optimized. A optical detection system is complex to integrate in the die of MEMS. If we optimize the electrode to compliant the vibration motion of bell plate, we can realise the detection by electrical method.[5, 106] And that brings more possibility of application based on this type of resonator.

In this chapter, a characterization of a the MEMS bell plate will be performed. Different with the SOI used in previous Chapter 4, we use here high-doped (both device and substrate layer) SOI wafer. It was selected to reduce the electrical resistance of the resonator and ensure efficient electrostatic actuation and capacitive readout. The low resistivity enables the resonator to maintain a nearly uniform potential under bias, whilst reducing series resistance, electrical losses and thermal noise, thereby also preventing severe Schottky rectification. These advantages motivated our work and Table **??** indicates the properties of the high-doped wafer we chosen. The geometric parameters designed and measured are indicated in Table 5.1. The photos of the die of the MEMS bell plate under microscope are illustrated in Figure 5.1. The influence of the optimized electrode geometry is investigated through both optical and electrical measurements. Finally, a feedthrough compensation circuit is introduced to suppress the large parasitic capacitive current inherent to gap-closing resonators, enabling the resonance to be directly detected by purely electrical means.[107] The results presented in this chapter demonstrate that electrode optimization, together with feedthrough cancellation, provides an effective route towards fully integrated electrical operation of high-Q MEMS bell-plate resonators.

Sample	Wt	W	Lt	L	Le
elec1	51 (50)	499 (500)	94 (95)	250 (250)	115 (115)

Table 5.1 – Geometric parameters of the electrode optimized sample after fabrication measured by optical microscopy and comparised with design expectations written in parenthesis. Dimensions are in microns.

5.2 . THEORETICAL CALCULATION OF ELECTRODE OPTIMIZATION

Unlike the first-order mode exhibits a nearly uniform out-of-plane motion, the resonator considered in this work displays a complex (2,0)-mode shape, in which the displacement field $\phi_m(\mathbf{r})$ varies in sign and magnitude across the electrode area. Consequently, portions of the electrode that overlap regions where ϕ_m is opposite to the dominant motion contribute a negative electrostatic coupling, reducing the overall transduction efficiency.

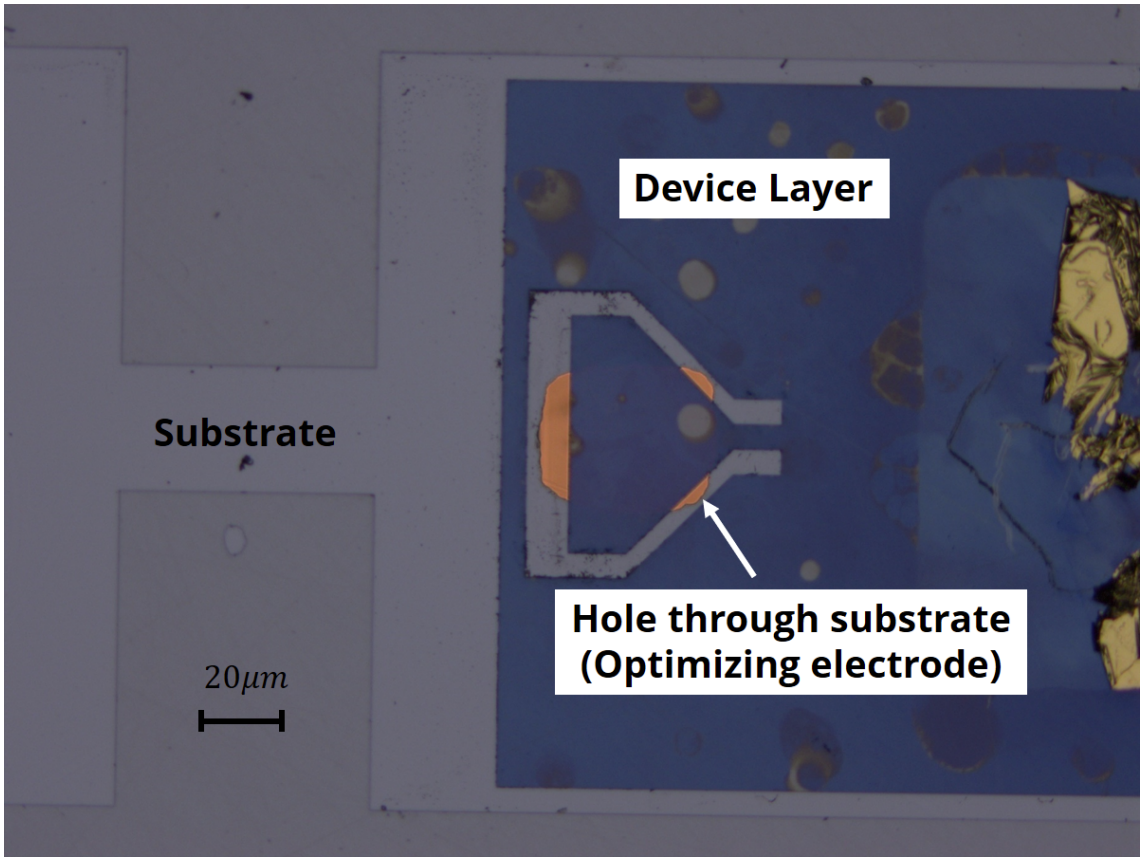

Figure 5.1 – Photo of the sample under microscope. Light from back indicates excellent alignment of optimized hole etched below the bell plate.

In our case, the bell plate is considered as vibrating with a static deformation. As a gap-closing MEMS resonators, Expanding the total displacement $w(\mathbf{r},t)$ in modal coordinates x[108] :

$$w(\mathbf{r},t) \cong \phi_0(\mathbf{r})\, x_0 + \phi_m(\mathbf{r})\, x_m(t) \tag{5.1}$$

The first term represent the static displacement, so that x_0 is a constant and the second term represent the motion of (2,0)-mode in this situation where $x_m(t)$ varies with time t.

With the static gap g and vacuum permittivity ε_0, the local capacitance $C(x_m(t))$ can be expressed as :

$$\begin{aligned} C(x_m(t)) &= \iint_S \frac{\varepsilon_0}{g - w(\mathbf{r},t)}\,\mathrm{d}S \\ &= \iint_S \frac{\varepsilon_0}{g - x_0\phi_0(\mathbf{r}) - x_m(t)\phi_m(\mathbf{r})}\,\mathrm{d}S \\ &= \iint_S \frac{\varepsilon_0}{(g - x_0\phi_0(\mathbf{r}))(1 - \frac{x_m(t)\phi_m(\mathbf{r})}{g - x_0\phi_0(\mathbf{r})})}\,\mathrm{d}S \end{aligned} \tag{5.2}$$

If we considered the motion of vibration is far lower then the gap remained after static deformation, $x_m\phi_m \ll g - x_0\phi_0$, the equation can be simplified as :

$$C(x_m(t)) \approx \iint_S \frac{\varepsilon_0}{g - x_0\phi_0(\mathbf{r})}(1 + \frac{x_m(t)\phi_m(\mathbf{r})}{g - x_0\phi_0(\mathbf{r})})\,\mathrm{d}S \tag{5.3}$$

$$C(x_m(t)) = C_0 + C_m(x_m(t)) \tag{5.4}$$

$$C_0 = \iint_S \frac{\varepsilon_0}{g - x_0\phi_0}\,\mathrm{d}S \approx \frac{\varepsilon_0 S}{g} + \frac{\varepsilon_0 x_0}{g^2}\iint_S \phi_0\,\mathbf{d}S \tag{5.5}$$

$$C_m(x_m(t)) = \iint_S \frac{\varepsilon_0 x_m \phi_m}{(g - x_0\phi_0)^2}\,\mathrm{d}S = x_m(t)\eta, \qquad \eta \equiv \varepsilon_0 \iint_S \frac{\phi_m}{(g - x_0\phi_0)^2}\,\mathrm{d}S \tag{5.6}$$

where η is the electrostatic coupling coefficient. When a DC bias voltage V_b and an AC drive voltage $v_{ac} = V_{ac}cos(\omega t)$ are applied, the instantaneous electrostatic force $F(x,t)$ acting on a differential element of the gap-closing capacitor is [109, 110] :

$$F(x,t) = \tfrac{1}{2}\frac{\partial C(x_m(t))}{\partial x_m(t)}\big[V_b + v_{ac}(t)\big]^2 \tag{5.7}$$

$$= \frac{1}{2}\eta\big[(V_b^2 + \frac{V_{ac}^2}{2}) + 2V_bV_{ac}cos(\omega t) + \frac{1}{2}V_{ac}^2cos(2\omega t)\big] \tag{5.8}$$

After linearising Equation (5.8) (retaining only the mixed term V_bV_{ac}), the effective drive force on the (2,0)-mode becomes :

$$F_m(t) = V_bV_{ac}\,\eta\,\cos(\omega t) \tag{5.9}$$

It depends directly on the spatial overlap between the electrode and the mode shape ϕ_m. If the electrode spans regions where $\phi_m < 0$, the integral in Equation (5.9) suffers partial cancellation, degrading the drive efficiency.

The sensed current originates from the time-varying capacitance. Differentiating Equation (5.2) and multiplying by the bias voltage yields the motional current :

$$i_m(t) = V_b\frac{\mathrm{d}C(t)}{\mathrm{d}t} \simeq V_b\,\eta\,\dot{x}_m(t) \tag{5.10}$$

which is likewise attenuated when the electrode covers portions of the resonator that move out of phase with the dominant motion.

Combining the quality factor Q and the stiffness k_m, the maximum displacement $x_{m,max}$ and maximum motional current $i_{m,max}$ are expressed respectively :

$$x_{m,max} = \frac{QF_{m,max}}{k_m} = \frac{QV_bV_{ac}\,\eta}{k_m}, \qquad i_{m,max} = \frac{QV_b^2V_{ac}\,\eta^2\omega}{k_m} \tag{5.11}$$

Motivated by the expressions above, we introduce a strategy : after computing the target mode shape $\phi_m(\mathbf{r})$ via finite-element analysis, most part of electrode sections coinciding with $\phi_m(\mathbf{r}) < 0$ are removed. This geometric modification eliminates the negative contributions in Equations (5.9), (5.10) and (5.11), thereby increasing the overall transduction coefficient. The electrode-optimized design and photos after fabrication were presented in Chapter 3. In next section, a FEM simulation were performed to verify the calculation of optimization.

Sample	First mode		(2,0)-mode	
	f (kHz)	Q_{anchor} ($\times 10^3$)	f (kHz)	Q_{anchor} ($\times 10^3$)
elec1	24.2	63.7	425.3	115

Table 5.2 – Simulated natural frequency and Q_{anchor} for the actual dimensions of the sample fabricated with electrode optimized design.

5.3 . SIMULATION OF ELECTRODE OPTIMIZATION

A FEM simulation was performed under the same assumptions as previous Chapters 2 and 4. The doping level slightly modifies the elastic constants, typically reducing the Young's modulus by only $1-3\%$, and this effect is usually neglected in mechanical design [111]. In this section, the discussions focus on the electrical behavior since mechanical aspects have already been widely discussed in Section 4.2. Since the plate does not include holes anymore (compared to the first design), the optimization procedure described in Chapter 3 has been performed again, leading to the dimension given in Table 5.1. Table 5.2 provides the corresponding simulated natural frequency and Q_{anchor}.

To simulate the electrical behavior, we modeled the overall behavior including the $1\ m$ vacuum gap and the $400\ m$ bulk silicon layer and applied an electric field between the two layers (see Figure 5.2). The bell plate device is actuated by a DC and AC voltage and the bulk is electrically grounded. An example of electrical and mechanical responses simulated by FEM under $0.2\ V$ AC voltage and under a bias voltage of $0.2\ V$ is given in Figure 5.3. The plotted displacement corresponds to the point of the plate with maximum deflection. This simulation estimates the overall static capacitance of the plate (without connection pads) to be around $0.4\,pF$. Based on the parallel-plate assumption and neglecting fringing fields, the capacitance of a full SOI square dice with $0.5\ mm$ side and $1\ m$ gap is $1.1\ pF$. Accounting for the presence of the hole in the bulk layer, this estimation is thus consistent with expectations.

Figure 5.3 illustrates that, due to the static capacitance of the plate itself, the parasitic current is too large for the motional signal to be realistically measurable. Even without accounting for additional parasitics (like electrical pad capacitance), measuring the electrical response of the MEMS bell plate requires an electrical interface with parasitic current suppression scheme and a high-sensitivity current detection (typically a lock-in amplifier connected after a current amplifier with $1\ nA/V$ gain) . To anticipate the results of such an optimized detection scheme, we plot in Figure 5.4(b) the current obtained in FEM simulation after suppression of the parasitic current (including both amplitude and phase aspects).

The improvement of the electrode optimization is estimated about $+800\%$ on the overall current response. To analyze this result further, the corresponding mechanical motion is plotted in Figure 5.4(a), highlighting a $+300\%$ increase of the motion. According to the theoretical equation we derived in Equation (5.11), the increase in current is approximately proportional to the square of the increase in displacement. Comparing these two results shows that the optimized electrode generates larger deformations, but that this gain is not fully captured by a rectangular electrode. Further optimizations could focus on adjusting the geometry of the hole but alternatives are limited by the practical fabrication constraints, such as lithography alignment, the sidewall slope achieved by DRIE and the

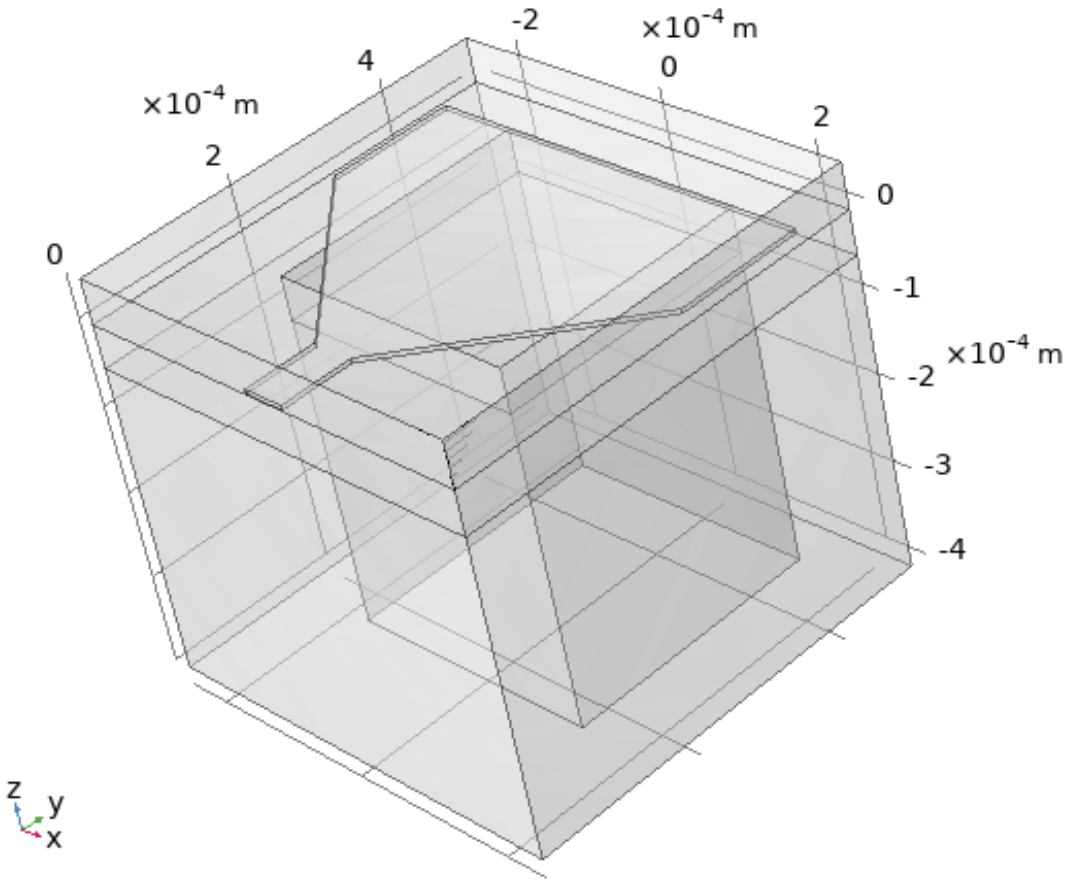

Figure 5.2 – New model set in COMSOL for electrical simulation.

Sample	First mode		(2,0)-mode	
	f (kHz)	Q ($\times 10^3$)	f (kHz)	Q ($\times 10^3$)
elec1	21.5	3.97	421.9	13.10

Table 5.3 – Characterization results for the actual dimensions of the sample fabricated with electrode optimized design.

non-uniform of $\mathrm{XeF_2}$. In particular, top and bottom alignment precision of the lithograph marks in the order of $10\ \mu m$; a DRIE deviation for thickness about $400\ \mu m$ is about $20\ \mu m$; and the discrepancy caused by $\mathrm{XeF_2}$ etching nonuniformity is on the order of a few micrometers. According to the simulation, we can expect to have a variance about $100mV$ with current amplifier of $1\ nA/V$ to obtain a detectable electrical resonant signal under vibration amplitude of the highest motion mode of at least $2\ \mu m$.

5.4 . OPTICAL DETECTION

Before testing the mechanical motion around the resonant by the approach describing in the previous Chapter 4. Figure 5.5 shows the frequency sweep to estimate the fabrication. Table 5.3 summarizes the key characterization results.

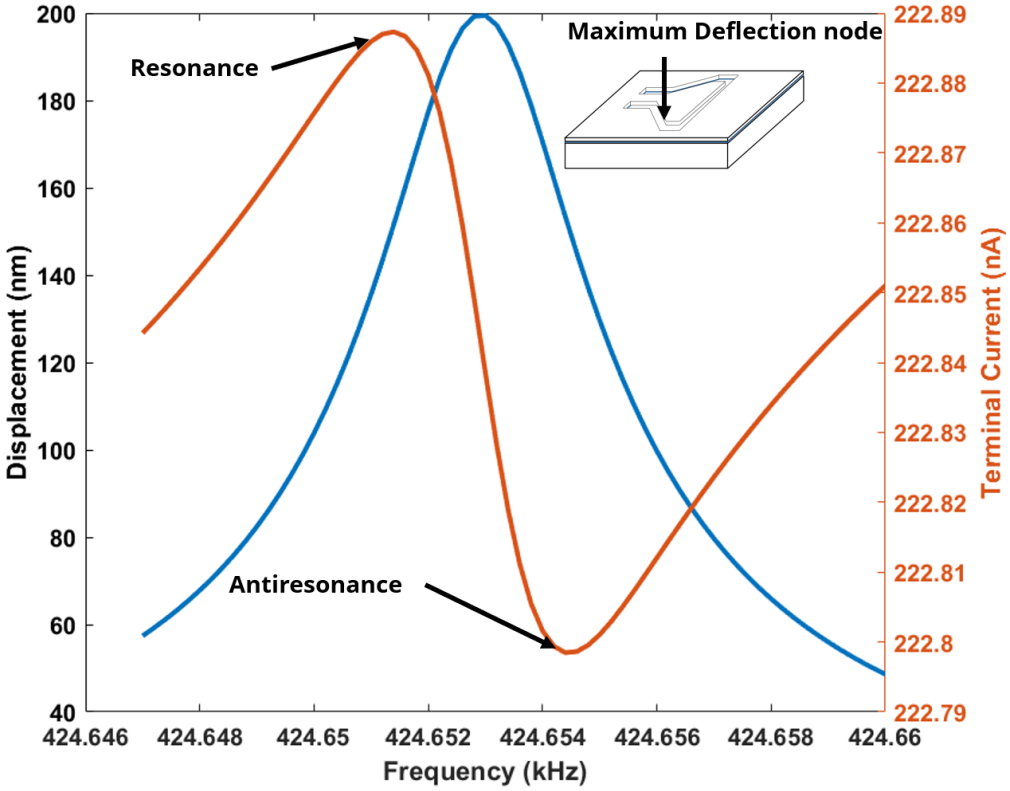

Figure 5.3 – FEM simulation of frequency sweep by two detection approaches.

The result of a manufacturing problem has emerged. The Q was much lower than expected, including that of the first bending mode. This is most likely due to the rough surface of the newly manufactured, highly doped silicon caused by HF etching. At the same time, we cannot rule out the following possibility : increased electrical losses due to higher conductivity, etched electrodes, and more complex electrical signal test circuits. It is even possible that the sample's design itself was not optimized to minimize anchoring losses. Therefore, the original simulation results are still used as reference values in the table.

Meanwhile, through this sample, we can still attempt to verify whether the electrical detection method will yield a measurable signal when the Q-factor is significantly lower than expected (i.e. when the vibration amplitude is much smaller than expected).

5.5 . ELECTRICAL DETECTION

5.5.1 . ELECTRICAL CIRCUIT CONFIGURATION

To suppress the electrical feedthrough arising from the parasitic capacitance of the MEMS bell-plate resonator, a capacitive compensation circuit was implemented, as shown in Figure 5.6. The resonator was excited by an AC voltage superimposed on a DC bias voltage, while a second AC voltage with independently adjustable amplitude and phase was applied to an external compensation capacitor C_{comp}. The output currents from the resonator and the compensation branch were combined at the input node of a transimpe-

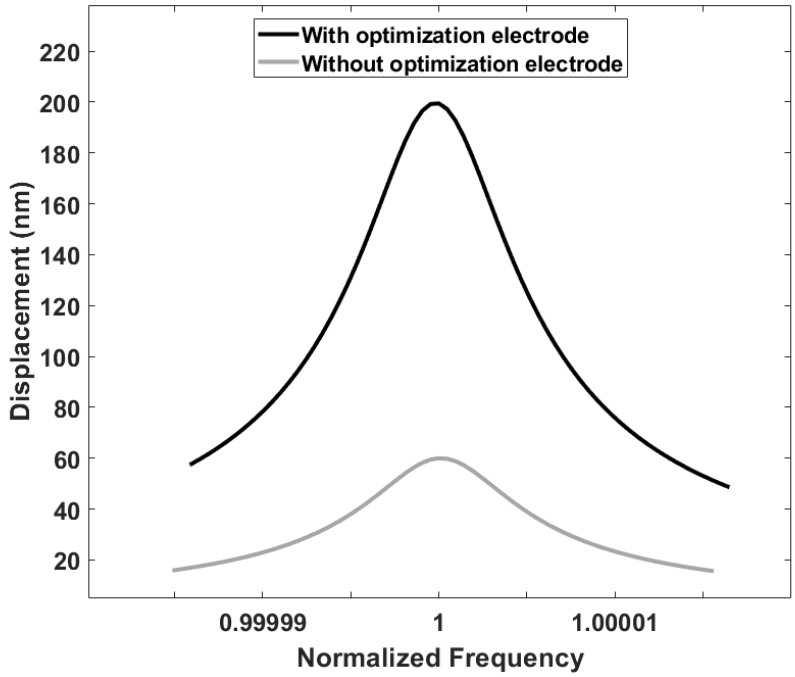

(a) Comparison of displacement

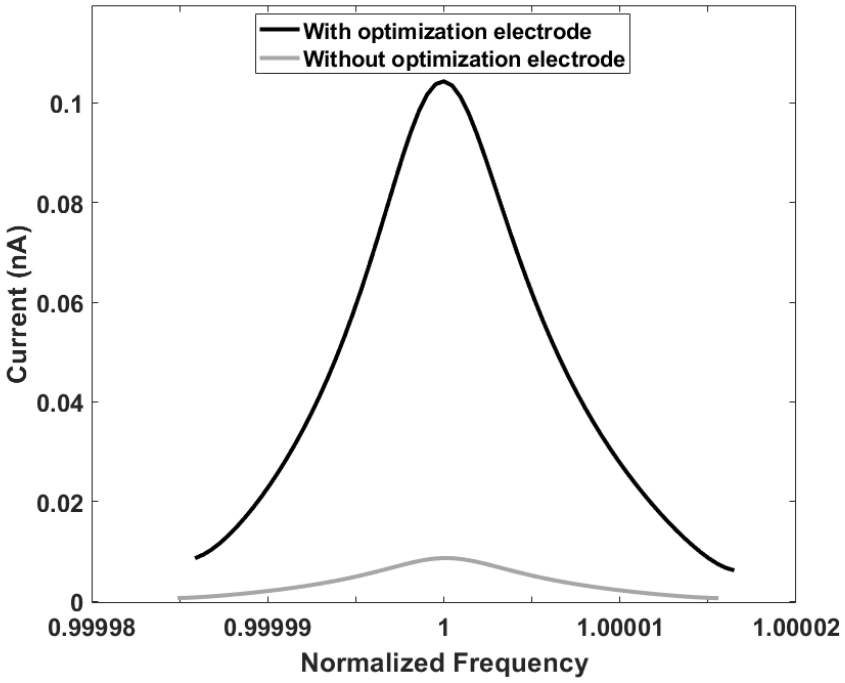

(b) Comparison of motional current

Figure 5.4 – Comparison of frequency responses by two method (mechanical and electrical) with the electrode before and after optimization.

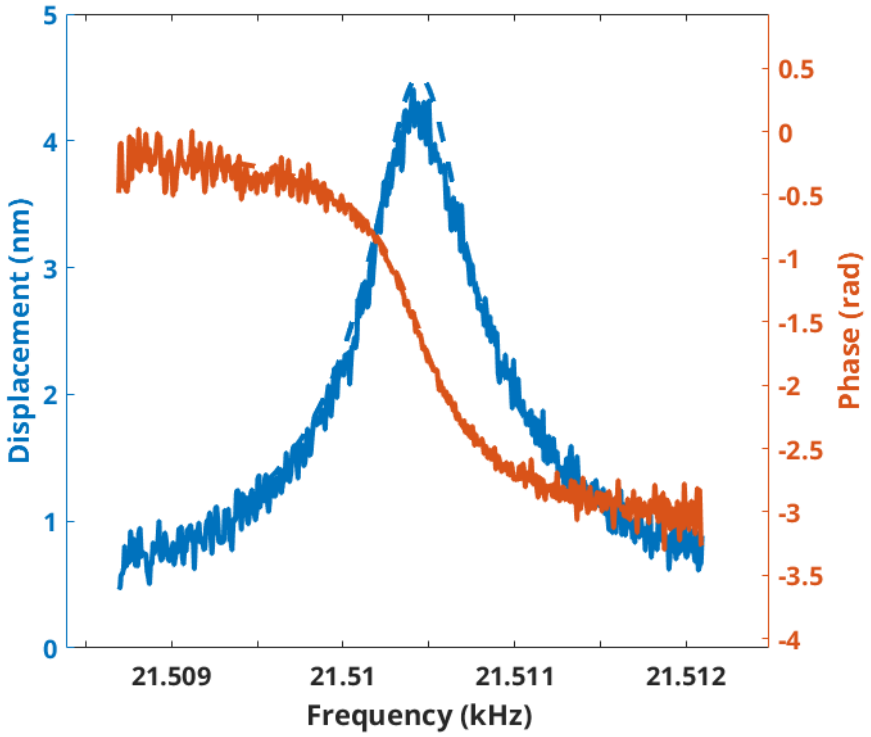

a)

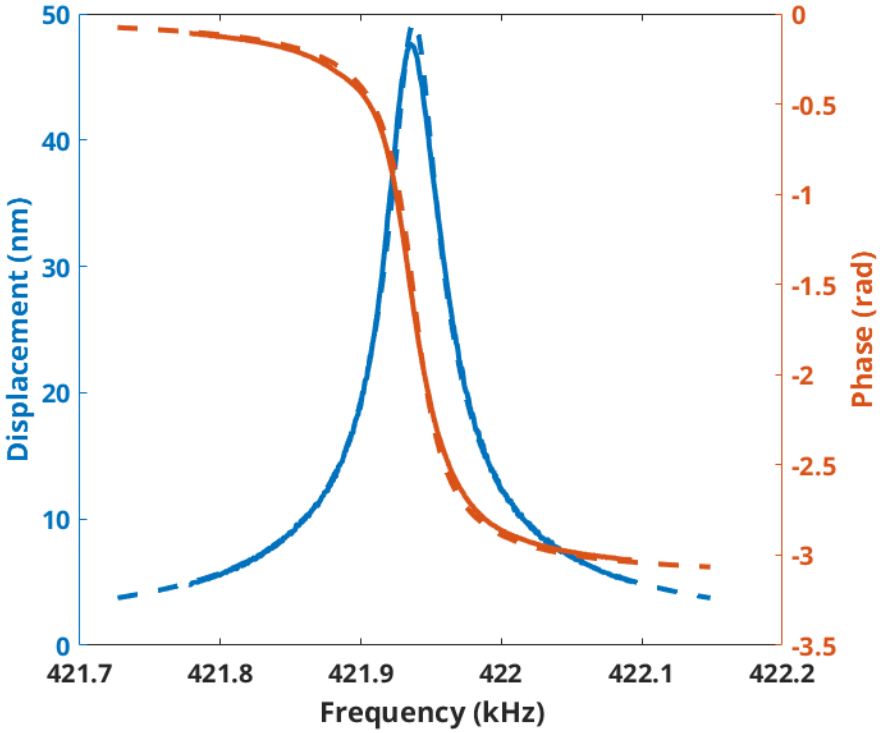

b)

Figure 5.5 – Experimental frequency responses of Sample 2.2 (solid line : measured data ; dashed line : fitted Lorentzian). a) First bending mode ; b) (2,0)-mode.

dance amplifier (1st amplifier) used as a charge amplifier. Figure 5.7 shows the theoretical bode diagram of the circuit from the input current into the first amplifier to the end vol-

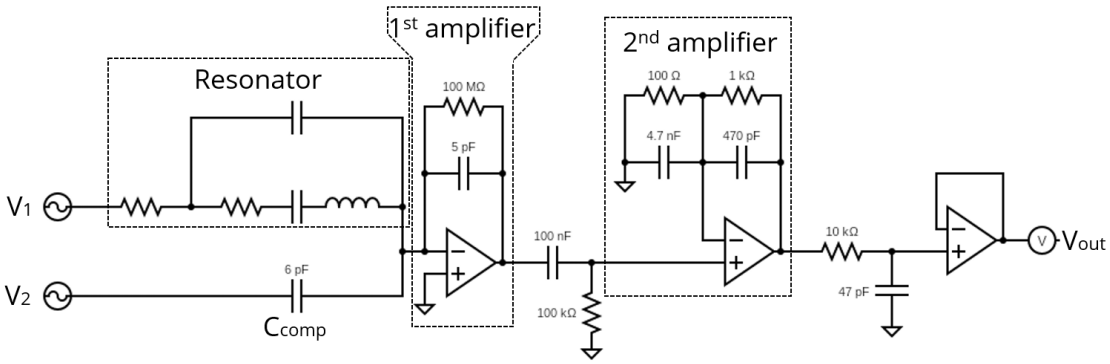

Figure 5.6 – Supplement ircuit with compensation line and current amplifier to release electrical detection. Our resonator device is shown schematically by electrical equivalent Butterworth-Van Dyke resonator model.

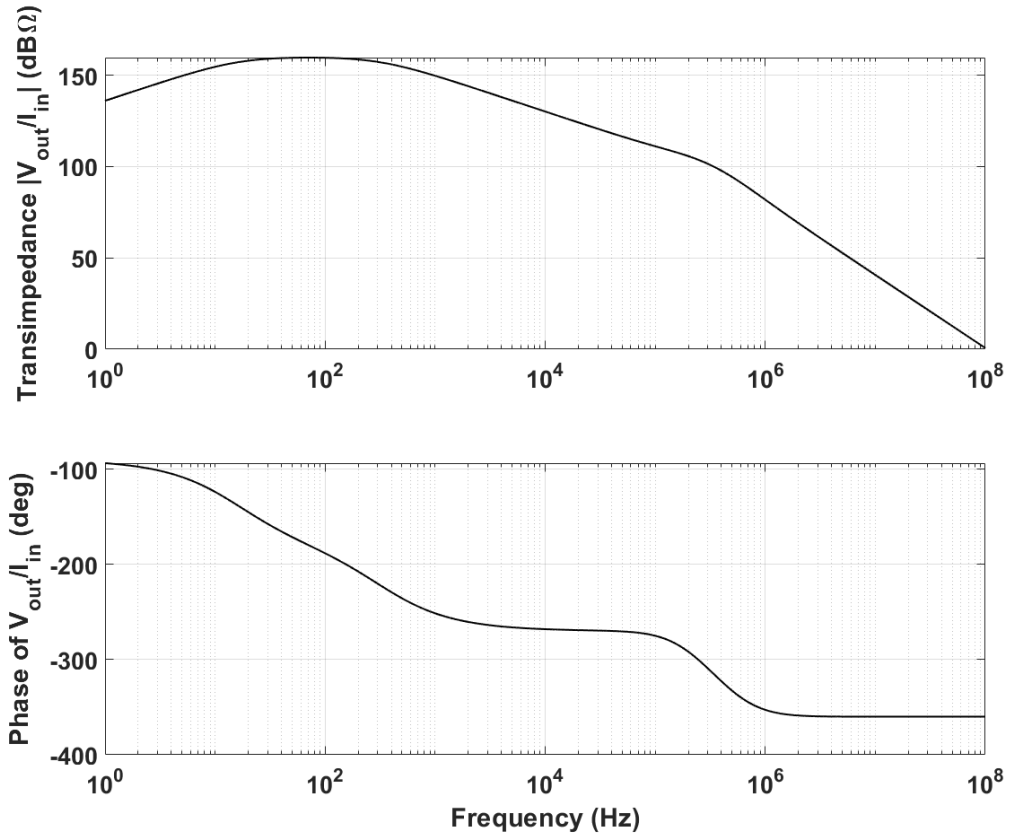

Figure 5.7 – Bode diagram of the circuit shown in Figure 5.6 from input node of the 1st amplifier I_{in} to V_{out}.

tage output. It is a custom-made general purpose amplifier circuit that is not necessarily fully-optimized for the bell plate. Thus, from the bode diagram, the MEMS resonator freqquency of my work didn't locate at the highest amplification frequency. However, it still work under our condition.

The measured current at the sensing node consists of two components,

$$I_{\mathrm{out}} = I_{\mathrm{mot}} + I_{\mathrm{ft}} \tag{5.12}$$

where I_{mot} denotes the motional current generated by the mechanical vibration of the resonator and I_{ft} represents the electrical feedthrough current caused by the parasitic capacitance between the drive and sensing electrodes. Since the parasitic capacitance is typically much larger than the dynamic capacitance variation associated with mechanical motion, the feedthrough current can dominate the measured signal and obscure the resonance response. The feedthrough current generated by the resonator parasitic capacitance is cancelled by the current flowing through a compensation capacitor. In practice, the exact value of the parasitic capacitance is generally unknown and additional phase shifts may be introduced by cables, connectors, and electronic components. Consequently, the compensation condition cannot be determined a priori. Instead, the amplitude and phase of the compensation voltage $\tilde{V}_{\mathrm{comp}}$ are adjusted experimentally while monitoring the off-resonance output signal. The compensation is considered optimal when the background feedthrough level reaches a minimum, indicating that the capacitive currents generated by parasitic capacitance C_par and compensation capacitance C_{comp} are nearly equal in magnitude and opposite in phase.

After feedthrough cancellation, the output signal is dominated by the motional current of the MEMS resonator. The electrical charge is converted into a voltage by the transimpedance amplifier and subsequently measured by the voltage detection system. By sweeping the excitation frequency around the resonant frequency, the frequency response of the resonator can be obtained with significantly improved signal-to-background ratio, enabling accurate extraction of the resonance characteristics.

5.5.2 . ELECTRICAL SIGNAL

Figure 5.8 shows the electrically-measured frequency response of the MEMS bell-plate resonator after the feedthrough compensation procedure. This measurement highlights that some parasitic current remains even after this procedure. This is due to the combination of two differents problems. One relates to the output voltage resolution of our setup (including Moku :Pro lock-in amplifier that is unable to provide an actuation voltage with lower than 1mV resolution). If it were possible to implement a compensation capacitor that is exactly at the same capacitance than the MEMS line (including MEMS intrinsic capacitance and connections), this would not be an issue. Unfortunately, this is unrealistic. The best implementation we could reach is based on a compensation capacitor of $6\ pF \pm 0.1\ pF$.

A clear resonance peak is observed around 421.9 kHz, demonstrating that the capacitive compensation scheme effectively suppresses the background feedthrough signal and enables the motional response of the resonator to be extracted from the electrical measurement.

The measured response was fitted using a complex Lorentzian model that accounts for both the resonator motional current and the residual feedthrough background. The fitted resonance frequency was found to be approximately 421.9 kHz, which is in excellent agreement with the resonance frequency obtained independently from optical measurements. This agreement confirms that the electrical readout successfully captures the targeted mechanical mode of the MEMS bell-plate resonator.

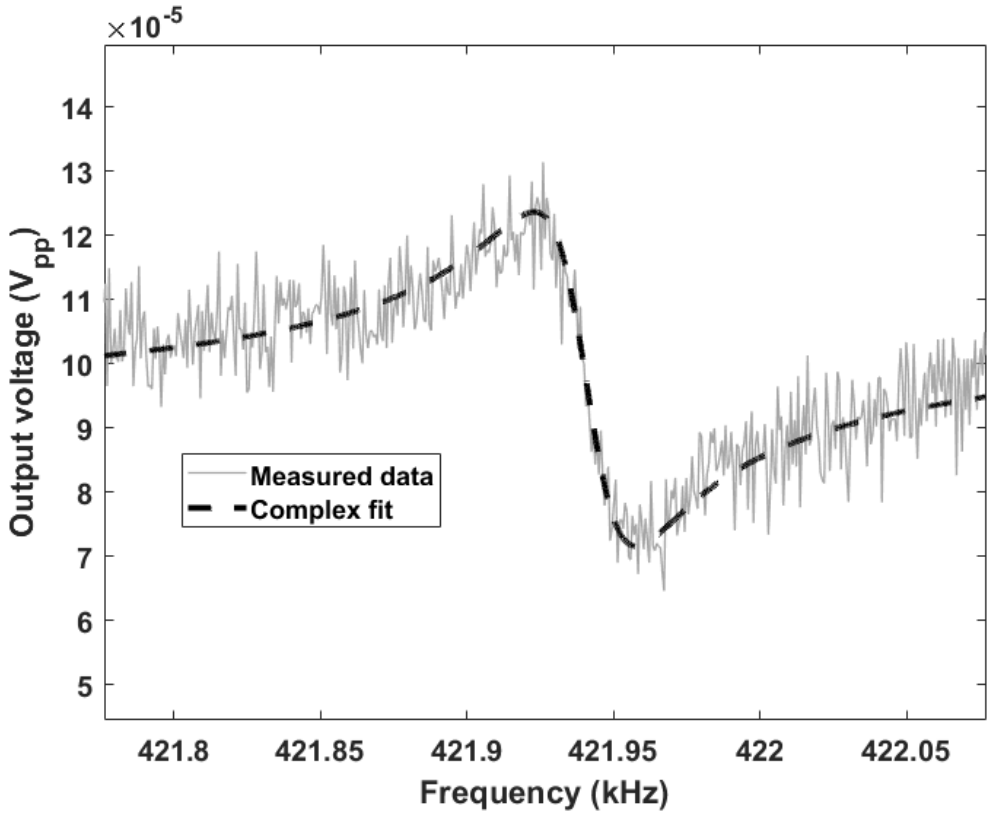

Figure 5.8 – Electrical detection with fitting of Lorentzian signal+feedthrough remained. Using complex fitting, the estimated resonant frequency is $421.938kHz$, and the Q-factor is $11,982$.

The quality factor extracted from the electrical measurement is of the order of 10^4, which is close to the value of $Q \approx 1.3 \times 10^4$ obtained from optical characterization. The small discrepancy between the two measurements may arise from residual electrical feedthrough, fitting uncertainty, and the different transduction mechanisms involved in the optical and electrical measurements. Nevertheless, the agreement remains within an acceptable range and demonstrates the validity of the electrical detection scheme.

It is worth noting that the resonance peak emerges from a relatively flat background level after optimization of the compensation signal amplitude and phase. This indicates that the residual feedthrough current has been significantly reduced and that the measured response is dominated by the motional current generated by the resonator vibration. Consequently, the proposed compensation approach provides an effective means of characterizing high-Q gap-closing MEMS resonators using purely electrical measurements.

5.6 . CONCLUSION

This chapter presented the design, theoretical analysis and experimental validation of an electrode-optimized MEMS bell-plate resonator intended for purely electrical actuation and detection. A theoretical model was first established to describe the electromechanical coupling of the (2,0) mode, showing that the transduction efficiency is governed by the spatial overlap between the electrode and the vibration mode. The analysis demons-

trated that electrode regions located above out-of-phase motion contribute negatively to the overall coupling coefficient and should therefore be removed to maximize both the driving force and the generated motional current.

Finite-element simulations confirmed the effectiveness of the proposed optimization strategy. By modifying the electrode geometry according to the calculated mode shape, both the vibration amplitude and the motional current were significantly enhanced, leading to an estimated increase of approximately 300% in displacement and nearly 800% in electrical current response compared with the original electrode configuration.

The fabricated resonator was subsequently characterized by both optical and electrical measurements. Although the measured quality factor was considerably lower than predicted because of fabrication-related imperfections and additional loss mechanisms, the optimized device still exhibited a clear resonance around 421.9 kHz. More importantly, the resonance frequency and quality factor extracted from the electrical measurement were in close agreement with those obtained optically, confirming the validity of the proposed capacitive readout approach.

A feedthrough compensation circuit was finally implemented to suppress the large parasitic capacitive current that masks the motional signal in gap-closing resonators. After optimization of the compensation amplitude and phase, a distinct resonance peak was successfully recovered using purely electrical measurements. These results demonstrate that, even under non-ideal fabrication conditions, the combination of mode-shape-based electrode optimization and feedthrough cancellation enables reliable electrical characterization of MEMS bell-plate resonators. This work therefore establishes an important step towards fully integrated high-Q MEMS resonators employing electrical excitation and detection without the need for external optical instrumentation.

6 - CONCLUSION AND FUTURE PERSPECTIVES

6.1 . SUMMARY OF THIS WORK

The objective of this thesis was to investigate a new approach for the design of high-quality-factor MEMS resonators inspired by the vibration mechanism of bell plates. The proposed resonator exploits the controllable nodal line of the (2,0)-ringing-mode to reduce anchor losses while remaining compatible with standard planar MEMS fabrication processes.

The main scientific contribution of this work is not only the introduction of a new resonator geometry, but also the establishment of a complete design methodology for bell-inspired MEMS resonators. Throughout this thesis, analytical modeling, finite-element simulations, microfabrication and experimental characterization have been combined to demonstrate that the quality factor can be systematically optimized by engineering the modal shape of the resonator. This methodology establishes a direct relationship between the geometric parameters, the nodal-line position, the anchor-loss mechanism and the resulting quality factor, providing a clear physical guideline for the design of future bell-inspired resonators.

The first part of this work focused on understanding the physical origin of high-Q bell plates. After reviewing the dominant dissipation mechanisms of MEMS resonators, anchor losses were identified as the principal limitation targeted in this work. The bell plate structure was shown to possess a unique property : the position of the U-shaped nodal line associated with the (2,0)-mode can be continuously adjusted through geometric design. Since the vibration amplitude at the support directly determines the amount of elastic energy transmitted into the substrate, controlling the nodal-line position provides an intuitive and efficient strategy for minimizing anchor losses.

To validate this concept, a comprehensive investigation was first carried out on macroscopic bell plates. Analytical models describing the resonance frequency of the (2,0)-mode were established and verified by finite-element simulations. Parametric studies revealed that the edge length L_e plays a dominant role in controlling the nodal-line position while only weakly influencing the resonance frequency. This observation considerably simplifies the design process because the quality factor and resonance frequency can be optimized almost independently. Stainless-steel bell plates were subsequently fabricated and experimentally characterized using both ring-down and frequency-response measurements.It exhibit a high-Q resonance of 8769 at about $640Hz$, which is about 50 times larger than the Q of the first bending mode at around $60Hz$ of the plates themselves. The measured results showed excellent agreement with the theoretical predictions and confirmed that proper tuning of the nodal-line position significantly improves the quality factor.

Building upon the understanding obtained from macroscopic structures, the proposed methodology was transferred to silicon MEMS resonators. A complete design rules for MEMS bell plate resonators were established by considering both mechanical performance and fabrication constraints. A fabrication process compatible with SOI technology was developed, including lithography, deep reactive ion etching, metallization and release processes. the experimental results obtained using a laser Doppler vibrometer was then presented. Comprehensive characterization of the initial batch of MEMS bell-

shaped plates was conducted, including the determination of key performance indicators and a comparative analysis of different designs. We characterized 4 samples that exhibited experimentally a high-Q resonance of their (2,0)-mode close to $180\ kHz$. The best-performing sample achieved a quality factor of $160\ k$ at $15\ C$. This is more than twice that of the first bending mode (which resonated at $17\ kHz$). This design is thus capable of achieving an $f \times Q$ product over $28\ GHz$. A comprehensive analysis and explanation of the measurements were included in this investigation. For the (2,0)-mode of one of the samples, the variation of the resonant frequency and quality factor with temperature, DC bias voltage and pressure were measured. According to the measurements, a pressure below $10^{-2}\ Pa$ was required for the air damping (e.g. squeeze-film damping and/or viscous damping) to be negligible compared to the clamping losses even for motion amplitudes as small as $1\ nm$ where losses can be linearized. In addition, for low-doped silicon, the TCF of the (2,0)-mode was measured at $-48\ ppm/C$, which was lower than that of the first mode ($-85\ ppm/C$). These results highlight the relevance of bell plates for MEMS applications.

Unlike conventional flexural beam resonators, the bell plate operates in a higher-order vibration mode exhibiting distributed regions vibrating with opposite displacement direction. Consequently, conventional lumped transduction models become insufficient. To address this issue, an electromechanical model describing the interaction between the distributed mode shape and gap-closing electrostatic transduction was developed. This model explains how the spatial distribution of the vibration mode influences both the effective electrostatic driving force and the generated motional current, providing a theoretical basis for the design of higher-order electrostatic MEMS resonators operating in higher vibration modes.

Experimental electrical characterization demonstrated successful electrostatic actuation and capacitive detection of the fabricated resonators. With a mechanical vibration deflection of approximately $50\ nm$, we obtained a detection signal of about $0.04\ mV$ (using a current amplifier circuit). Although the present devices remain proof-of-concept prototypes, the measured resonance characteristics demonstrate the feasibility of the proposed bell-inspired structure.

Overall, this thesis establishes a complete research framework extending from the physical understanding of bell-plate vibration mechanisms to the realization of MEMS devices. More importantly, it demonstrates that nodal-line engineering provides an effective alternative to conventional high-Q design strategies. Rather than relying on highly symmetric geometries or complicated acoustic isolation structures, high quality factors may be achieved through careful control of the modal shape itself. The methodology proposed in this work therefore provides not only a new resonator structure but also a new design philosophy that can potentially be extended to many other higher-order MEMS resonators.

6.2 . FUTURE PERSPECTIVES

Although the feasibility of bell-inspired MEMS resonators has been demonstrated throughout this work, several important aspects remain to be investigated before the full potential of this structure can be exploited.

The first direction concerns frequency stability. The present work has mainly focused

on improving the quality factor through structural optimization and reduction of anchor losses. While a high quality factor constitutes a fundamental requirement for resonant devices, the ultimate performance of MEMS oscillators is determined by their frequency stability. Future studies should therefore include a complete evaluation of oscillator performance, including phase noise, frequency noise and Allan deviation. Such investigations will allow the intrinsic advantages of bell-inspired resonators to be quantified and compared with existing high-performance MEMS resonators.

The second direction involves further optimization of the fabrication process. During the final stage of this work, bell plate resonators fabricated on highly doped silicon wafers successfully demonstrated electrostatic actuation and electrical detection. However, the fabrication process remains at an early stage of development. Several imperfections, including etching non-uniformity, dimensional deviations and release-related defects, still affect the consistency of the fabricated devices. Further optimization of DRIE, release processes, metallization and electrode fabrication is expected to improve both fabrication yield and device performance. In addition, optimization of the electrode geometry with more precision could further enhance the electromechanical coupling efficiency while reducing parasitic feedthrough.

Finally, the bell-inspired resonator structure proposed in this thesis offers promising opportunities for future MEMS applications. Owing to its combination of relatively low operating frequency, high quality factor and compatibility with electrostatic transduction, it represents an attractive candidate for low-phase-noise MEMS oscillators and timing references. Furthermore, its high mechanical sensitivity makes it suitable for resonant sensing applications, including force, mass and inertial sensors. Beyond the bell plate itself, the design methodology established in this thesis may also be extended to other MEMS structures employing higher-order vibration modes, where modal-shape engineering can be exploited to reduce anchor losses and improve overall resonator performance.

In conclusion, this thesis demonstrates that bell-inspired resonators constitute a promising new structure for high-Q MEMS devices. By establishing both the physical principles governing their operation and a complete design methodology from macroscopic validation to MEMS realization, this work provides a solid foundation for future research on bell-inspired resonators and their integration into innovative sensing and timing systems.

APPENDIX

A . EVOLUTION OF NATURAL FREQUENCY TO L_e

The evolution of natural frequency with L_e is not so conclusive as the influence of other geometric parameters. internal stress distribution changes a lot with different L_e. This makes it difficult for us to use simplified formulas to predict its changes. This appendix shows how evolves of L_e affect the natural frequencies of the two corresponding modes, first bending mode and (2,0)-mode.

A.1 . FIRST BENDING MODE

For the first model, the changes in the internal stress distribution within the material remain similar. Thus, All evolution exhibits a similar trend, with its natural frequency being proportional to the reciprocal of L_e. Although the ratio varies, this trend is consistent with the basic theory of plate mode.

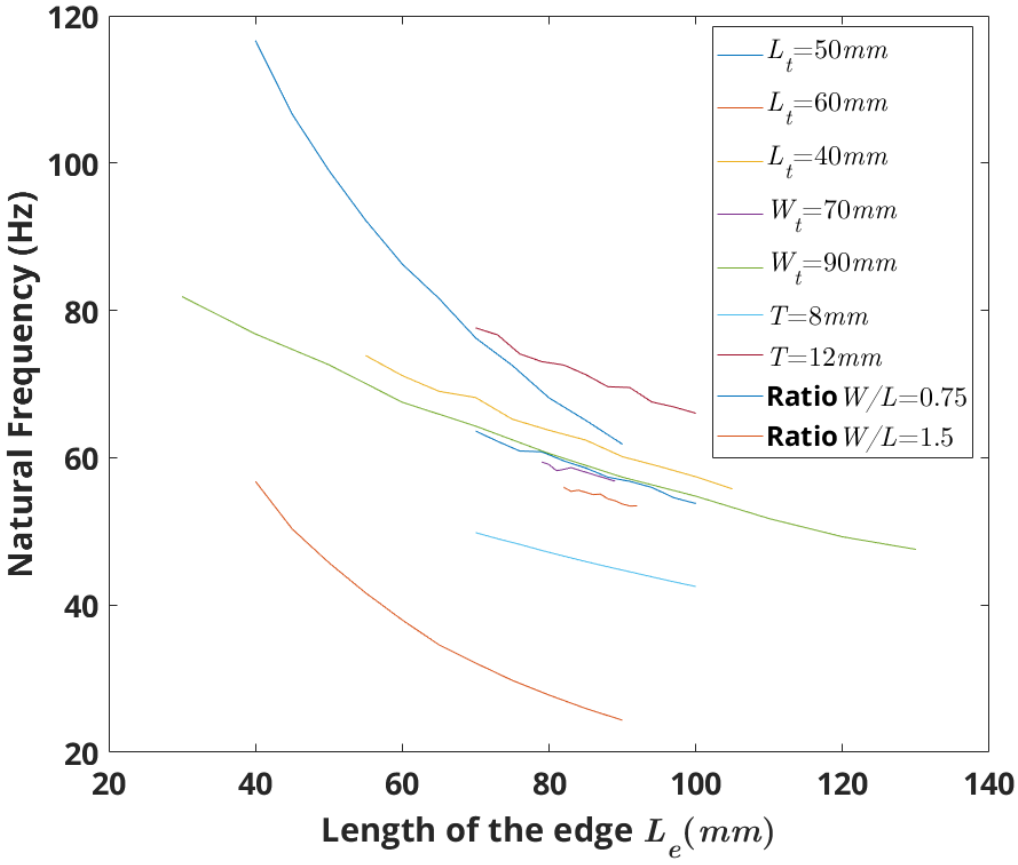

Figure 1 – Variation of natural frequency of the first mode with L_e by FEM simulation with other different geometric parameters.

A.2 . (2,0)-MODE

Compared to the first bending mode shown above, each of the (2,0)-mode evolutions exhibits a distinct inflection point. Furthermore, this inflection point occurs near the optimal L_e, indicating that the mode shape evolution follows two distinct patterns on either side of this L_e.

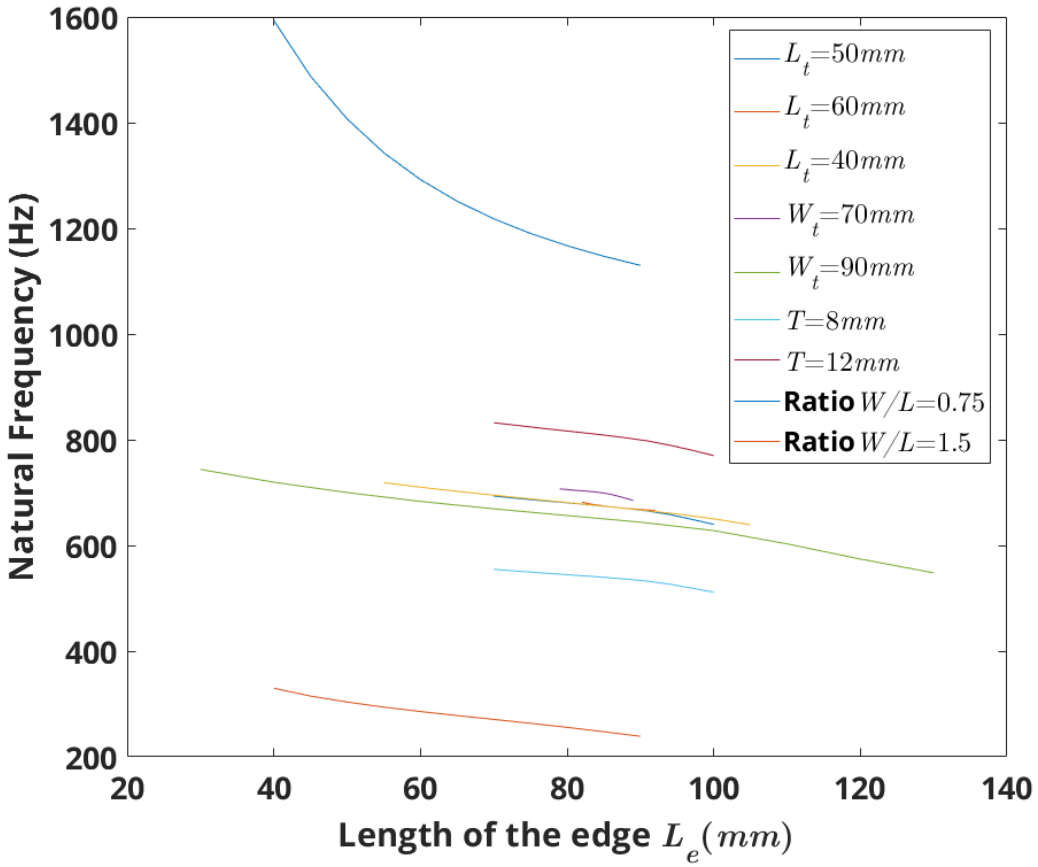

Figure 2 – Variation of natural frequency of the (2,0)-mode with L_e by FEM simulation with other different geometric parameters.

A.3 . CONCLUSION

Based on our analysis of the FEM simulation results, we have determined that the change in L_e corresponding to the change in the natural frequency of the (2,0)-mode cannot be calculated using simplified formulas. However, we do not need to calculate this precisely, because the optimal L_e corresponding to each different geometric parameter is unique, and the effect of L_e on frequency is negligible compared to that of other geometric parameters. This allows us to simplify our design approach : we can adjust other parameters to approach our target frequency and then use L_e to optimize the quality factor.

B . SUPPLEMENTARY SEM PHOTOS

Figure 3 shows a scanning electron microscope (SEM) image of a bell-shaped plate featuring an array of holes on its top surface, while Figure 4 presents a high-magnification view of the same specimen. This design entails a certain risk, as the proximity of the hole array to the plate's edge (only $5\mu m$ in design) makes it susceptible to breakage during fabrication, especially when we release the device with HF. Damaged plate cannot meet our requirements for a high Q-factor. However, it also demonstrates that the manufacturing process possesses sufficient precision to realize such a design.

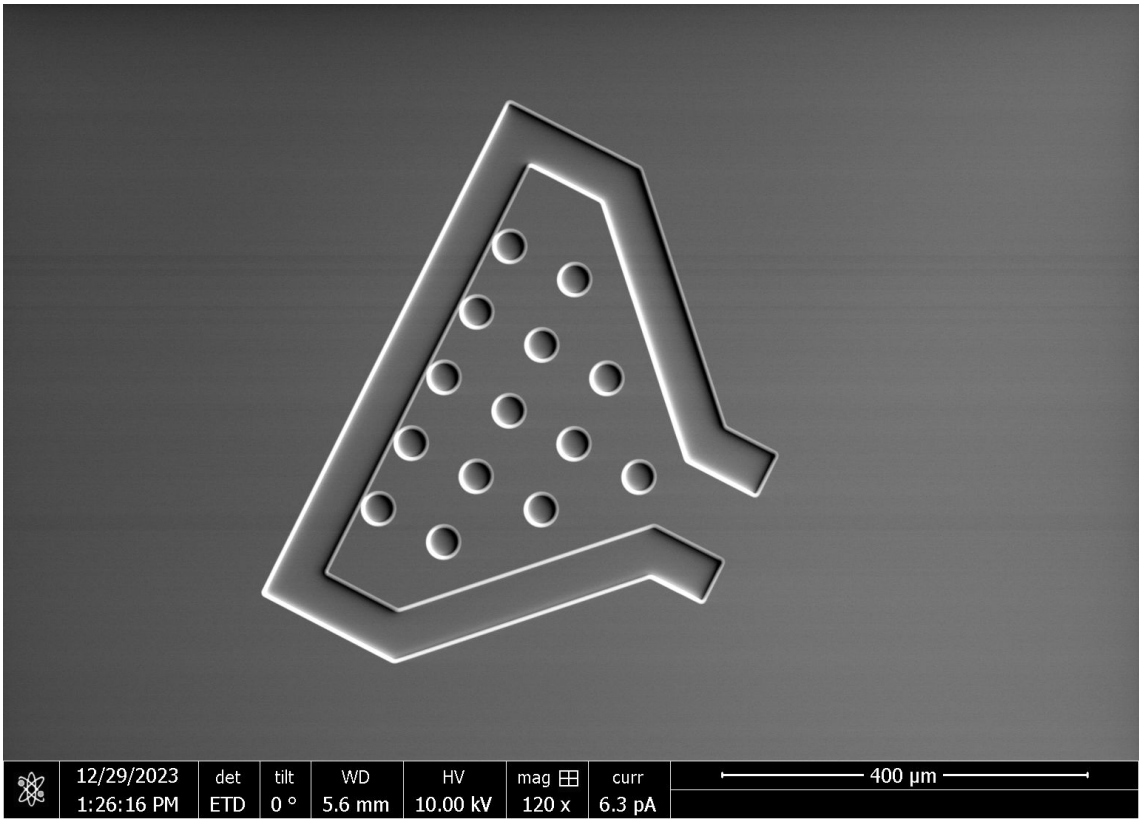

Figure 3 – SEM photo of one sample with holes on the plate layer, fabricated using the simplified process.

Figure 5 is the sample fabricated with optimized electrode. The subfigure with the blue border clearly illustrates the DRIE process. The irregular edges it ultimately produces result from the alternating cycles of isotropic and non-isotropic etching in the Bosch-like process. Additionally, for this sample, the surface underwent three consecutive DRIE processes, which is reflected in the results : the etching ratio shows distinct variations from top to bottom.

The subfigure with the orange border shows the edge of silicon etched with XeF_2, which differs significantly from the results obtained with DRIE. Furthermore, it is difficult to precisely control the etching process with this method; therefore, it is typically used to remove the sacrificial layer. For this sample, the bottom hole is intended to optimize the electrode, and high precision is not required for it. Moreover, this hole was created using a two-step process—first DRIE, then XeF_2—so the etching result is acceptable.

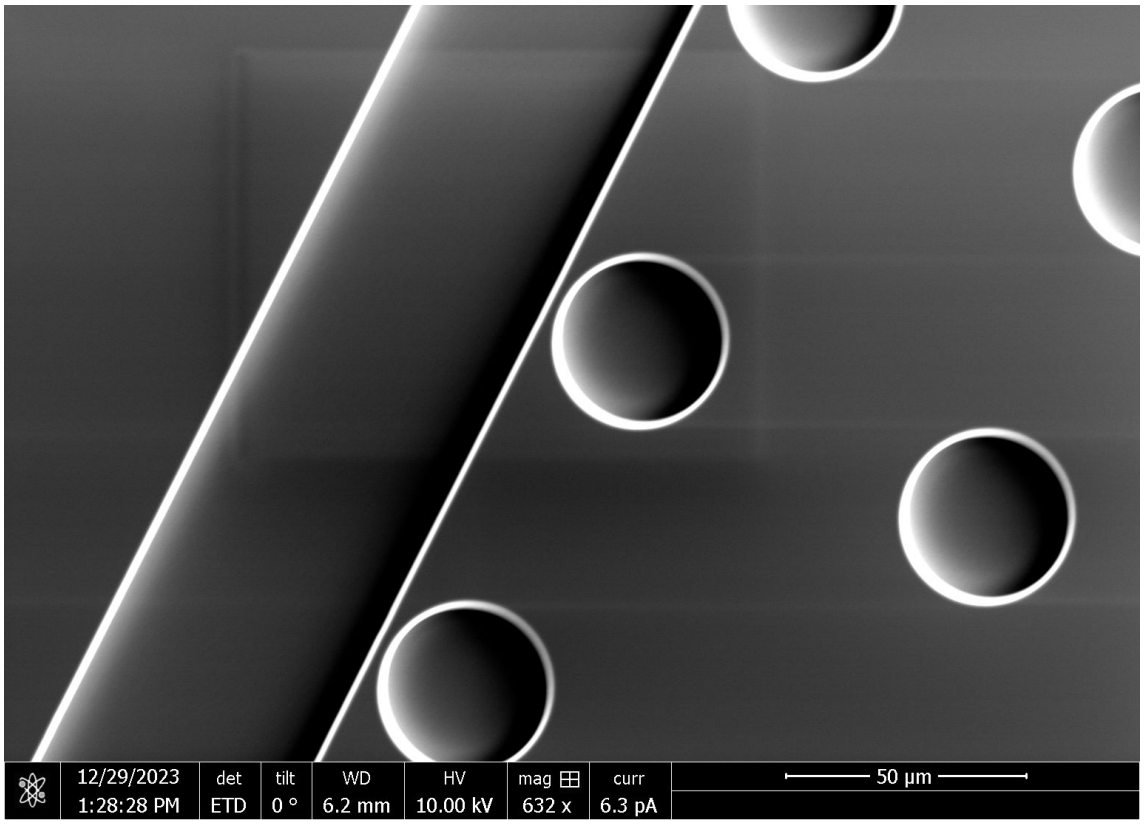

Figure 4 – Detailed SEM photo of the sample shown in Figure 3.

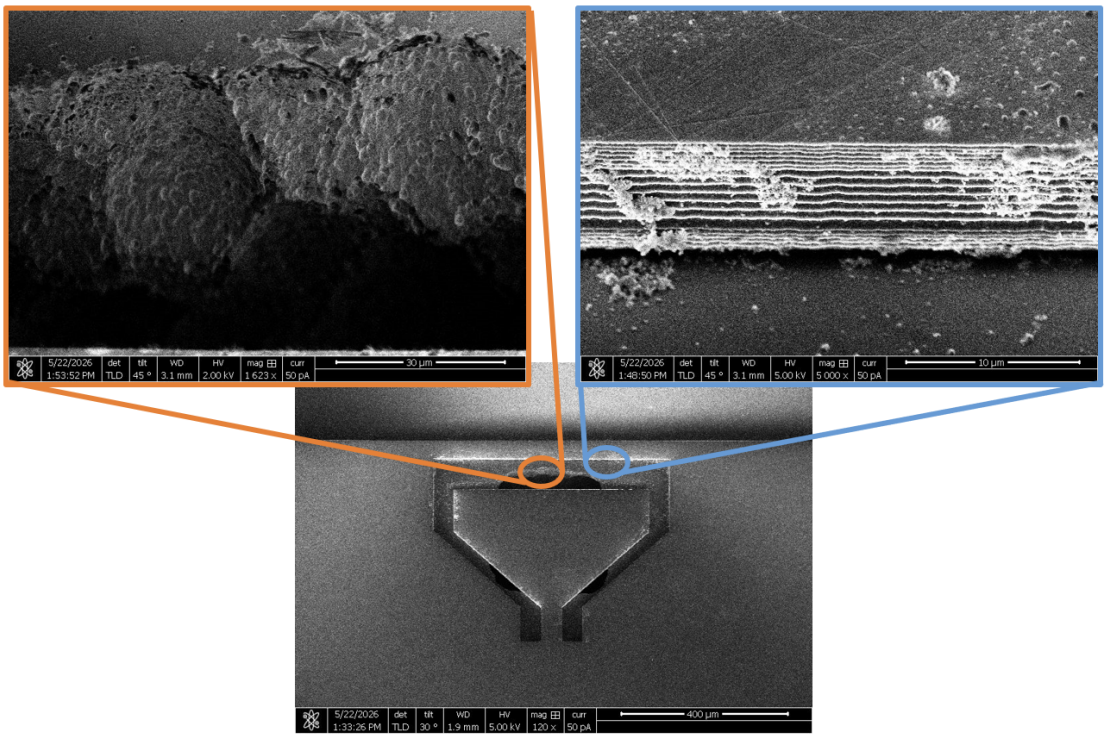

Figure 5 – SEM photo focusing on the edge of silicon. Each sub-figure corresponds to the silicon etched by different methods : Blue : DRIE ; Orange : XeF_2.

LIST OF FIGURES

1 Photo d'une cloche plate en métal fabriquée dans l'atelier de notre laboratoire. . . . 16
2 Simulation par éléments finis de la déformée du mode (2,0) d'une cloche plate. . . . 16
3 Prototype MEMS réalisé sur substrat SOI, photo et image MEB. . . . 17
4 Schéma du dispositif de caractérisation et de la configuration du MEMS pour une caractérisation complète. . . . 18
5 un circuit de détection électrique permettant de réduire la capacité parasite, accompagné d'une photo d'un échantillon de cloche plate à électrode optimisée. . . . 19

1.1 Estimated evolution of Q_{SFD} with the thickness and air pressure of the plate gap. . . . 27
1.2 Limit on resonator quality factor posed by thermoelastic dissipation for $1\mu m$- and $10\mu m$-wide single crystal silicon (SCS) beams [39]. . . . 28
1.3 (a) Structure of decoupling MEMS tuning fork gyroscope, (b) Driving mode, (c) Sensing mode [16]. . . . 33
1.4 SEM view of a clamped–clamped single crystal silicon beam resonators fabricated through the HARPSS process [61]. . . . 34
1.5 (a) Structure, (b) SEM view, and (c) simulated width-extensional mode shape of the Silicon Bulk Acoustic resonator (SiBAR) device in ANSYS (t=10 µm) [19]. 35
1.6 (a) Unit cell model of the resonator based on LN/SiC. (b) SEM image of the C-band SH-SAW resonator proposed in this study [64]. . . . 35
1.7 Simulated mode shape of the SH-SAW resonator [19]. . . . 36
1.8 Strain-engineered 1D phononic crystals. (A) Scanning electron microscopy (SEM) image of a tapered PnC nanobeam, vertically scaled for perspective. (B) Width/stress profile and defect mode shape of a device with 60 unit cells [67]. . . . 36
1.9 (a) Hemispherical shell , (b) Second mode of vibration (n = 2) of a wineglass (hemisphere)-shaped resonator [69]. . . . 37
1.10 A ringing tocsin of a church (Photo from internet). . . . 37
1.11 Scanning electron micrographs of the bell resonator [78]. . . . 38
1.12 Commercial bell plate musical instrument. Left : rectangular bell plate © Acolyte Instruments. Right : trapezoidal bell plate © Belleplates. . . . 38
1.13 Nodal patterns for isosceles triangular plates with same triangle height and different ratio of height to length [79]. . . . 39
1.14 Evolution of Chladni patterns of bell plate. (iv) is the ringing mode of bell plate (called (2,0)-mode) when the bell plated designed properly [10]. . . . 39

2.1 Schematic of the bell plate. . . . 44
2.2 Mode shapes of the first four modes under clamped-free condition (clamped on the edge of the tang) for the design of Table 2.1. . . . 45

2.3 Evolution of simulated natural frequency of the (2,0)-mode with $\frac{W}{L}$ for five plates of different geometries. Parameters not listed in the legend are identical to example parameters (dark dots, see Table.2.1). The discrepancies between theory and simulation are lower than 1%, so that crosses and dots appear superimposed. 46
2.4 Normalized mode shape simulations of (2,0)-mode under two boundary conditions. Green indicates the nodal line. Left : free-free condition ; right : clamped-free condition. Top : high Q_{anchor} plate ; bottom : high Q_{anchor} plate. 47
2.5 Evolution of Q_{anchor} of the (2,0)-mode with L_e by FEM simulation under tang variations. 49
2.6 Evolution of Q_{anchor} of the (2,0)-mode with L_e by FEM simulation for different thicknesses and widths of the plates (maintaining the ratio $\frac{W}{L}$). The grey line corresponds to changing T and L at the same time while maintaining the natural frequency of the reference (dark line). 50
2.7 Evolution of Q_{anchor} of the (2,0)-mode with L_e by FEM simulation with different ratio $\frac{w}{L}$ 51
2.8 Ring-down response and fitting curve including two modes for each macroscopic bell plate. 52
2.9 Experimental setup for macroscopic bell plate 53
2.10 Frequency response and fitting curve of the (2,0)-mode 54
2.11 Forces applied in static structural simulations 55
2.12 Linear and nonlinear static FEM simulation results. The y-axis corresponds to the magnitude of F_w. 55

3.1 Schematic diagram of SOI cross-section 58
3.2 3D Schematic diagram of the expected MEMS bell plate. Blue line indicate the contour of silicon dioxide layer which will be etched to release the device. 58
3.3 Flowchart of the MEMS bell-plate design. 59
3.4 Schematic diagram of the masks of the bell plate with holes on the substrate. Area in shadow is designed to be etched, two type of shadow correspond to different layers. 64
3.5 Schematic of the device cross-section along fabrication. The circle emphasizes the lateral under-etching of the SiO_2 layer. 65
3.6 Schematic of the spin-coating process : (i) dispense resist, (ii) spin, (iii) stop, (iv) solvent evaporation. 66
3.7 Schematic of the ICP/DRIE process. A sufficient number of cycles is applied to etch silicon through til the $\mathrm{SiO_2}$ layer. 67
3.8 Simplified fabrication flow (no backside etching). 69
3.9 Mask layout of the bell plate with release holes (shaded area to be etched). 70
3.10 SEM micrograph of a sample fabricated by the simplified process. 71
3.11 SEM micrograph of a sample fabricated by the optimized process (with backside release hole). 71
3.12 SEM micrographs comparing the surface of device after fabrication : (a) low-doped wafer, and (b) high-doped wafer. 72

3.13 Optical comparison of two samples before and after HF release. Both come from the same wafer. Upper : after release (silicon appears darker) ; Bottom : before release (silicon-oxide layer appears darker). 73

4.1 Optical microscopy image of a MEMS sample. The under-etching area is brighter than its surrounding area. 76
4.2 Profile of a sample at $25°$C. (a) 3D profilometry of the MEMS bell plate (the blue line indicates the cross-section position). (b) 2D height profile taken along the bisector. 78
4.3 Thermo-mechanical static simulation of a bell plate heated by $25°$C (reference temperature $0°$C). The colour bar indicates the normalised displacement amplitude. 79
4.4 Static force-displacement characteristic recorded using FemtoTools test bench, along with a linear fit with slope of $10.621N/m$. 79
4.5 Schematic of the experimental setup. Green lines : closed-loop control ; blue lines : open-loop excitation ; yellow line : temperature-control system ; red line : laser beam from the vibrometer. 80
4.6 Experimental frequency responses of Sample 2.2 (solid line : measured data ; dashed line : fitted Lorentzian). (a) First bending mode ; (b) (2,0)-mode. . . . 81
4.7 Measured and simulated resonant frequencies of Sample 2.2 as a function of temperature (10–35°C). 82
4.8 Experimental (markers) and simulated (solid line) evolution of the (2,0)-mode Q versus temperature for Sample 2.2. 83
4.9 Experimental evolution of resonant frequency and Q for Sample 2.2 as a function of DC bias voltage. (a) First bending mode ; (b) (2,0)-mode. 84
4.10 Normalized resonant frequency (solid symbols) and quality factor (open symbols) versus DC bias for Sample 2.2 at $25°$C. 85
4.11 Measured Q of the (2,0)-mode as a function of nitrogen pressure. 86

5.1 Photo of the sample under microscope. Light from back indicates excellent alignment of optimized hole etched below the bell plate. 90
5.2 New model set in COMSOL for electrical simulation. 93
5.3 FEM simulation of frequency sweep by two detection approaches. 94
5.4 Comparison of frequency responses by two method (mechanical and electrical) with the electrode before and after optimization. 95
5.5 Experimental frequency responses of Sample 2.2 (solid line : measured data ; dashed line : fitted Lorentzian). a) First bending mode ; b) (2,0)-mode. 96
5.6 Supplement ircuit with compensation line and current amplifier to release electrical detection. Our resonator device is shown schematically by electrical equivalent Butterworth-Van Dyke resonator model. 97
5.7 Bode diagram of the circuit shown in Figure 5.6 from input node of the 1st amplifier I_{in} to V_{out}. 97
5.8 Electrical detection with fitting of Lorentzian signal+feedthrough remained. Using complex fitting, the estimated resonant frequency is $421.938kHz$, and the Q-factor is $11,982$. 99

1 Variation of natural frequency of the first mode with L_e by FEM simulation with other different geometric parameters. 105
2 Variation of natural frequency of the (2,0)-mode with L_e by FEM simulation with other different geometric parameters. 106
3 SEM photo of one sample with holes on the plate layer, fabricated using the simplified process. 107
4 Detailed SEM photo of the sample shown in Figure 3. 108
5 SEM photo focusing on the edge of silicon. Each sub-figure corresponds to the silicon etched by different methods : Blue : DRIE ; Orange : XeF_2. 108

LIST OF TABLES

1.1 Representative quality-factor limits associated with the main dissipation mechanisms in room-temperature silicon MEMS resonators. 32
1.2 Comparison of MEMS resonator families and dominant dissipation mechanisms. 41

2.1 Dimensions (in mm) of a macroscopic bell plate example. L_{tot} is $70\ mm$ (see 2.1). 44
2.2 Eigenvalue λ of the (2,0)-mode for bell plates in different value of $\frac{W}{L}$. 46
2.3 Dimensions (in mm) of the fabricated macroscopic bell plates. L_{tot} of Plate 1 and Plate 2 are $68.3mm$ and $70.3mm$ respectively. 49
2.4 Simulation results of the two plates under clamped-free conditions and estimation of the air damping after comparison with ring-down measurements. 50
2.5 Summary of ring-down responses of two plates under clamped-free conditions 51

3.1 Summary of the requirements for MEMS bell plate design in this work . . . 57
3.2 Physical properties of the low-doped and high-doped SOI wafer. 63
3.3 Initial design parameters. 63
3.4 Spin-coating parameters for the two lithography steps. 66

4.1 Geometric parameters of the samples after fabrication measured by optical microscopy and comparison with design expectations written in parenthesis. Dimensions are in microns. 76
4.2 Simulation results for the actual dimensions of the samples given in Table 4.1. 77
4.3 Resonant frequency, quality factor and $f \times Q$ extracted from measurements at $25°$C on the four samples (values from FEM simulations are shown in parentheses). 80
4.4 State-of-the-art of high-Q resonators for timing references with resonant frequency below 1MHz 88

5.1 Geometric parameters of the electrode optimized sample after fabrication measured by optical microscopy and comparised with design expectations written in parenthesis. Dimensions are in microns. 89
5.2 Simulated natural frequency and Q_{anchor} for the actual dimensions of the sample fabricated with electrode optimized design. 92
5.3 Characterization results for the actual dimensions of the sample fabricated with electrode optimized design. 93

LIST OF PUBLICATIONS

JOURNAL PAPER

1. T. Zhu et al., "Novel Low-Voltage Silicon MEMS Resonators With High f×Q Product Inspired From Bell Plates," *IEEE Transactions on Ultrasonics, Ferroelectrics, and Frequency Control*, vol. 72, no. 11, pp. 1533-1542, Nov. 2025.

CONFERENCE PAPERS

1. T. Zhu, A. Poizat, E. Lefeuvre, A. Brenes, "Frequency response measurements and analysis of a bell plate's ringing mode", *European Nonlinear Dynamics Conference (ENOC 2024)*, Delft, Netherland, July. 22-26, 2024.

2. T. Zhu, E. Lefeuvre, E. Herth, D. Bouville and A. Brenes, "Novel design of SOI-based MEMS bell plates for resonant applications," *2024 Symposium on Design, Test, Integration and Packaging of MEMS/MOEMS (DTIP)*, Dresden, Germany, 2024, pp. 1-5.

3. T. Zhu, E. Lefeuvre, E. Herth, D. Bouville and A. Brenes, "A Novel MEMS Structure with Multiple High-Q Resonances for Low-Voltage 20kHz to 600kHz Oscillators," *2025 Joint Conference of the European Frequency and Time Forum and IEEE International Frequency Control Symposium (EFTF/IFCS)*, Querétaro, Mexico, 2025, pp. 1-2.

REFERENCES

[1] Tianren Feng et al. “Concepts and Key Technologies of Microelectromechanical Systems Resonators”. In : *Micromachines* 13.12 (2022). issn : 2072-666X. doi : 10.3390/mi13122195. url : https://www.mdpi.com/2072-666X/13/12/2195.

[2] Lei Wei et al. “The Recent Progress of MEMS/NEMS Resonators”. In : *Micromachines* 12.6 (2021). issn : 2072-666X. doi : 10.3390/mi12060724. url : https://www.mdpi.com/2072-666X/12/6/724.

[3] Joydeep Basu et Tarun Bhattacharyya. “Microelectromechanical Resonators for Radio Frequency Communication Applications”. In : *Microsystem Technologies* 17 (oct. 2011), p. 1557-1580. doi : 10.1007/s00542-011-1332-9.

[4] K.Y. Yasumura et al. “Quality factors in micron- and submicron-thick cantilevers”. In : *Journal of Microelectromechanical Systems* 9.1 (2000), p. 117-125. doi : 10.1109/84.825786.

[5] Clark T.-c. Nguyen. “MEMS technology for timing and frequency control”. In : *IEEE Transactions on Ultrasonics, Ferroelectrics, and Frequency Control* 54.2 (2007), p. 251-270. doi : 10.1109/TUFFC.2007.240.

[6] Matthias Imboden et Pritiraj Mohanty. “Dissipation in nanoelectromechanical systems”. In : *Physics Reports* 534.3 (2014). Dissipation in nano-electromechanical systems, p. 89-146. issn : 0370-1573. doi : https://doi.org/10.1016/j.physrep.2013.09.003. url : https://www.sciencedirect.com/science/article/pii/S0370157313003475.

[7] Sergei A. Zotov et al. “Quality Factor Maximization Through Dynamic Balancing of Tuning Fork Resonator”. In : *IEEE Sensors Journal* 14.8 (2014), p. 2706-2714. doi : 10.1109/JSEN.2014.2314614.

[8] J.R. Clark et al. “High-Q UHF micromechanical radial-contour mode disk resonators”. In : *Journal of Microelectromechanical Systems* 14.6 (2005), p. 1298-1310. doi : 10.1109/JMEMS.2005.856675.

[9] J.E.-Y. Lee et A.A. Seshia. “5.4-MHz single-crystal silicon wine glass mode disk resonator with quality factor of 2 million”. In : *Sensors and Actuators A : Physical* 156.1 (2009). EUROSENSORS XXII, 2008, p. 28-35. issn : 0924-4247. doi : https://doi.org/10.1016/j.sna.2009.02.007. url : https://www.sciencedirect.com/science/article/pii/S0924424709000417.

[10] D Lavan, S Hogg et Joe Wolfe. “Why do Bell Plates Ring?” In : *Acoustics Australia August* 31 (août 2003).

[11] *Vibratory and Acoustic Behavior of Orchestral Bell Plates*. T. Design Engineering. ASME International Mechanical Engineering Congress and Exposition. Nov. 2004, p. 503-508. doi : 10.1115/IMECE2004-60087. eprint : https://asmedigitalcollection.asme.org/IMECE/proceedings-pdf/IMECE2004/47055/503/2619258/503_1.pdf. url : https://doi.org/10.1115/IMECE2004-60087.

[12] C.T.-C. Nguyen. “Micromechanical resonators for oscillators and filters”. In : *1995 IEEE Ultrasonics Symposium. Proceedings. An International Symposium*. T. 1. 1995, 489-499 vol.1. doi : 10.1109/ULTSYM.1995.495626.

[13] Cornelis A. Van Eysden et John E. Sader. “Frequency response of cantilever beams immersed in viscous fluids with applications to the atomic force microscope : Arbitrary mode order”. In : *Journal of Applied Physics* 101.4 (fév. 2007), p. 044908. issn : 0021-8979. doi : 10.1063/1.2654274. eprint : https://pubs.aip.org/aip/jap/article-pdf/doi/10.1063/1.2654274/14978157/044908_1_online.pdf. url : https://doi.org/10.1063/1.2654274.

[14] Hiroshi Hosaka, Kiyoshi Itao et Susumu Kuroda. “Damping characteristics of beam-shaped micro-oscillators”. In : *Sensors and Actuators A : Physical* 49.1 (1995), p. 87-95. issn : 0924-4247. doi : https://doi.org/10.1016/0924-4247(95)01003-J. url : https://www.sciencedirect.com/science/article/pii/092442479501003J.

[15] A. Anwar Zainuddin et al. “Design and simulation of Clamped-Clamped and Clamped-Free resonators”. In : *Fifth Asia Symposium on Quality Electronic Design (ASQED 2013)*. 2013, p. 55-59. doi : 10.1109/ASQED.2013.6643564.

[16] Chuanguo Xiong et al. “Design and Optimization of a Novel MEMS Tuning Fork Gyroscope Microstructure”. In : *Micromachines* 13.2 (2022). issn : 2072-666X. doi : 10.3390/mi13020172. url : https://www.mdpi.com/2072-666X/13/2/172.

[17] Muhammad Ali Butt. “Beyond the detection limit : A review of high-Q optical ring resonator sensors”. In : *Materials Today Physics* 58 (2025), p. 101873. issn : 2542-5293. doi : https://doi.org/10.1016/j.mtphys.2025.101873. url : https://www.sciencedirect.com/science/article/pii/S2542529325002299.

[18] Wen Chen et al. “Design, Modeling and Characterization of High-Performance Bulk-Mode Piezoelectric MEMS Resonators”. In : *Journal of Microelectromechanical Systems* 31.3 (2022), p. 318-327. doi : 10.1109/JMEMS.2022.3159995.

[19] Tzu-Hsuan Hsu et al. “C-Band Lithium Niobate on Silicon Carbide SAW Resonator With Figure-of-Merit of 124 at 6.5 GHz”. In : *Journal of Microelectromechanical Systems* 33.5 (2024), p. 604-609. doi : 10.1109/JMEMS.2024.3423768.

[20] Sajal Singh et al. “Design and fabrication of high-Q birdbath resonator for MEMS gyroscopes”. In : *2018 IEEE/ION Position, Location and Navigation Symposium (PLANS)*. 2018, p. 15-19. doi : 10.1109/PLANS.2018.8373358.

[21] Lixia Li et al. “Quality Factor Enhancement of Piezoelectric MEMS Resonator Using a Small Cross-Section Connection Phononic Crystal”. In : *Sensors* 22.20 (2022). issn : 1424-8220. doi : 10.3390/s22207751. url : https://www.mdpi.com/1424-8220/22/20/7751.

[22] D. R. Southworth et al. “Stress and Silicon Nitride : A Crack in the Universal Dissipation of Glasses”. In : *Phys. Rev. Lett.* 102 (22 juin 2009), p. 225503. doi : 10.1103/PhysRevLett.102.225503. url : https://link.aps.org/doi/10.1103/PhysRevLett.102.225503.

[23] Kirsi Tappura, Panu Pekko et Heikki Seppä. “High-Q micromechanical resonators for mass sensing in dissipative media”. In : *Journal of Micromechanics and Microengineering* 21.6 (avr. 2011), p. 065002. doi : 10.1088/0960-1317/21/6/065002. url : https://doi.org/10.1088/0960-1317/21/6/065002.

[24] Jamilah Karim, A.H.M. Alam et Anis Nordin. “MEMS-BASED OSCILLATORS : A REVIEW”. In : *IIUM Engineering Journal* 15 (mai 2014). doi : 10.31436/iiumej.v15i1.446.

[25] Shirin Ghaffari et al. “Quantum Limit of Quality Factor in Silicon Micro and Nano Mechanical Resonators”. In : *Scientific Reports* 3.1 (nov. 2013). doi : 10.1038/srep03244. url : https://doi.org/10.1038/srep03244.

[26] Leo Sementilli, Erick Romero et Warwick P. Bowen. “Nanomechanical Dissipation and Strain Engineering”. In : *Advanced Functional Materials* 32.3 (2022), p. 2105247. doi : https://doi.org/10.1002/adfm.202105247. eprint : https://advanced.onlinelibrary.wiley.com/doi/pdf/10.1002/adfm.202105247. url : https://advanced.onlinelibrary.wiley.com/doi/abs/10.1002/adfm.202105247.

[27] Muhammad Wajih Ullah Siddiqi et al. “Numerical analysis of anchor loss and thermoelastic damping in piezoelectric AlN-on-Si Lamb wave resonators”. In : *Journal of Micromechanics and Microengineering* 29.10 (août 2019), p. 105013. doi : 10.1088/1361-6439/ab392c. url : https://doi.org/10.1088/1361-6439/ab392c.

[28] Hartono Sumali. “Squeeze-film damping in the free molecular regime : Model validation and measurement on a MEMS”. In : *J. Micromech. Microeng* 17 (nov. 2007), p. 2231-2240. doi : 10.1088/0960-1317/17/11/009.

[29] Minhang Bao et Heng Yang. “Squeeze film air damping in MEMS”. In : *Sensors and Actuators A : Physical* 136.1 (2007). 25th Anniversary of Sensors and Actuators A : Physical, p. 3-27. issn : 0924-4247. doi : https://doi.org/10.1016/j.sna.2007.01.008. url : https://www.sciencedirect.com/science/article/pii/S0924424707000118.

[30] Robert B. Darling, Chris Hivick et Jianyang Xu. “Compact analytical modeling of squeeze film damping with arbitrary venting conditions using a Green’s function approach”. In : *Sensors and Actuators A : Physical* 70.1 (1998), p. 32-41. issn : 0924-4247. doi : https://doi.org/10.1016/S0924-4247(98)00109-5. url : https://www.sciencedirect.com/science/article/pii/S0924424798001095.

[31] J.B. Starr. “Squeeze-film damping in solid-state accelerometers”. In : *IEEE 4th Technical Digest on Solid-State Sensor and Actuator Workshop*. 1990, p. 44-47. doi : 10.1109/SOLSEN.1990.109817.

[32] RG Christian. “The theory of oscillating-vane vacuum gauges”. In : *Vacuum* 16.4 (1966), p. 175-178. issn : 0042-207X. doi : https://doi.org/10.1016/0042-207X(66)91162-6. url : https://www.sciencedirect.com/science/article/pii/0042207X66911626.

[33] Minhang Bao et al. “Energy transfer model for squeeze-film air damping in low vacuum”. In : *Journal of Micromechanics and Microengineering* 12.3 (avr. 2002), p. 341. doi : 10.1088/0960-1317/12/3/322. url : https://doi.org/10.1088/0960-1317/12/3/322.

[34] Minhang Bao. “Chapter 3 - Air Damping”. In : *Analysis and Design Principles of MEMS Devices*. Amsterdam : Elsevier Science, 2005, p. 115-174. isbn : 978-0-444-51616-9. doi : https://doi.org/10.1016/B978-044451616-9/50004-7. url : https://www.sciencedirect.com/science/article/pii/B9780444516169500047.

[35] Weidong Wang, Jianyuan Jia et Jianwen Li. “Slide film damping in microelectromechanical system devices”. In : *Proceedings of the Institution of Mechanical Engineers Part N Journal of Nanoengineering and Nanosystems* 227 (déc. 2013), p. 162-170. doi : 10.1177/1740349913486097.

[36] Claudio L.A. Berli et Alberto Cardona. “On the calculation of viscous damping of microbeam resonators in air”. In : *Journal of Sound and Vibration* 327.1 (2009), p. 249-253. issn : 0022-460X. doi : https://doi.org/10.1016/j.jsv.2009.06.003. url : https://www.sciencedirect.com/science/article/pii/S0022460X09004921.

[37] Clarence M. Zener et Sidney Siegel. “Elasticity and Anelasticity of Metals.” In : *The Journal of Physical and Colloid Chemistry* 53.9 (1949), p. 1468-1468. doi : 10.1021/j150474a017. url : https://doi.org/10.1021/j150474a017.

[38] Amy Duwel et al. “Engineering MEMS Resonators With Low Thermoelastic Damping”. In : *Journal of Microelectromechanical Systems* 15.6 (2006), p. 1437-1445. doi : 10.1109/JMEMS.2006.883573.

[39] R. Abdolvand et al. “Quality factor in trench-refilled polysilicon beam resonators”. In : *Journal of Microelectromechanical Systems* 15.3 (2006), p. 471-478. doi : 10.1109/JMEMS.2006.876662.

[40] S.Y. Chen, X. Niu et F.L. Guo. “Thermoelastic damping in micromechanical resonators operating as mass sensors”. In : *European Journal of Mechanics - A/Solids* 71 (2018), p. 165-178. issn : 0997-7538. doi : https://doi.org/10.1016/j.euromechsol.2018.03.017. url : https://www.sciencedirect.com/science/article/pii/S0997753817304801.

[41] Valentina Zega et al. “Analysis of Frequency Stability and Thermoelastic Effects for Slotted Tuning Fork MEMS Resonators”. In : *Sensors* 18.7 (2018). issn : 1424-8220. doi : 10.3390/s18072157. url : https://www.mdpi.com/1424-8220/18/7/2157.

[42] Ron Lifshitz et M. L. Roukes. “Thermoelastic damping in micro- and nanomechanical systems”. In : *Phys. Rev. B* 61 (8 fév. 2000), p. 5600-5609. doi : 10.1103/PhysRevB.61.5600. url : https://link.aps.org/doi/10.1103/PhysRevB.61.5600.

[43] Daniel Schiwietz, Eva M. Weig et Peter Degenfeld-Schonburg. “Thermoelastic Damping in MEMS Gyroscopes at High Frequencies”. In : *Microsystems & Nanoengineering* 9.1 (2023). url : https://doi.org/10.1038/s41378-022-00480-1.

[44] Andrew Norris et Douglas Photiadis. “Thermoelastic Relaxation in Elastic Structures, with Applications to Thin Plates”. In : *The Quarterly Journal of Mechanics and Applied Mathematics* 58 (juin 2004). doi : 10.1093/qjmamj/hbi002.

[45] Zhili Hao, Ahmet Erbil et Farrokh Ayazi. “An analytical model for support loss in micromachined beam resonators with in-plane flexural vibrations”. In : *Sensors and Actuators A : Physical* 109.1 (2003), p. 156-164. issn : 0924-4247. doi : https://doi.org/10.1016/j.sna.2003.09.037. url : https://www.sciencedirect.com/science/article/pii/S0924424703004898.

[46] Douglas M. Photiadis et John A. Judge. “Attachment losses of high Q oscillators”. In : *Applied Physics Letters* 85.3 (juill. 2004), p. 482-484. issn : 0003-6951. doi : 10.1063/1.1773928. eprint : https://pubs.aip.org/aip/apl/article-pdf/85/3/482/18591734/482_1_online.pdf. url : https://doi.org/10.1063/1.1773928.

[47] I. Wilson-Rae. “Intrinsic dissipation in nanomechanical resonators due to phonon tunneling”. In : *Phys. Rev. B* 77 (24 juin 2008), p. 245418. doi : 10.1103/PhysRevB.77.245418. url : https://link.aps.org/doi/10.1103/PhysRevB.77.245418.

[48] M. C. Cross et Ron Lifshitz. “Elastic wave transmission at an abrupt junction in a thin plate with application to heat transport and vibrations in mesoscopic systems”. In : *Phys. Rev. B* 64 (8 août 2001), p. 085324. doi : 10.1103/PhysRevB.64.085324. url : https://link.aps.org/doi/10.1103/PhysRevB.64.085324.

[49] Cole GD et al. “Phonon-tunnelling dissipation in mechanical resonators”. In : *Nature Communications* 2.231 (mars 2011). doi : 10.1038/ncomms1212. url : https://doi.org/10.1038/ncomms1212.

[50] Jeronimo Segovia-Fernandez et al. “Anchor Losses in AlN Contour Mode Resonators”. In : *Journal of Microelectromechanical Systems* 24.2 (2015), p. 265-275. doi : 10.1109/JMEMS.2014.2367418.

[51] M.C. Cross et Ron Lifshitz. “Elastic wave transmission at an abrupt junction in a thin plate with application to heat transport and vibrations in mesoscopic systems”. In : *Physical Review B - Condensed Matter and Materials Physics* 64 (août 2001), p. 853241-8532422.

[52] Saeed Mohammadi et al. “High-Q micromechanical resonators in a two-dimensional phononic crystal slab”. In : *Applied Physics Letters* 94.5 (fév. 2009), p. 051906. issn : 0003-6951. doi : 10.1063/1.3078284. eprint : https://pubs.aip.org/aip/apl/article-pdf/doi/10.1063/1.3078284/14406316/051906_1_online.pdf. url : https://doi.org/10.1063/1.3078284.

[53] David Bindel et Sanjay Govindjee. “Elastic PMLs for resonator anchor loss simulation”. In : *International Journal for Numerical Methods in Engineering* 64 (oct. 2005), p. 789-818. doi : 10.1002/nme.1394.

[54] P. G. Steeneken et al. “Parameter extraction and support-loss in MEMS resonators”. In : *COMSOL Users Conference 2007 Grenoble* (2007). url : https://www.comsol.jp/paper/parameter-extraction-and-support-loss-in-mems-resonators-2421.

[55] J. Gaspar, V. Chu et J. P. Conde. “Dissipation Mechanisms in Thin-Film Silicon Microresonators on Glass Substrates”. In : *MRS Proceedings* 782 (2003), A5.37. doi : 10.1557/PROC-782-A5.37.

[56] G. Palasantzas. “Surface roughness influence on the quality factor of high frequency nanoresonators”. In : *Journal of Applied Physics* 103.4 (fév. 2008), p. 046106. issn : 0021-8979. doi : 10.1063/1.2874790. eprint : https://pubs.aip.org/aip/jap/article-pdf/doi/10.1063/1.2874790/15004528/046106_1_online.pdf. url : https://doi.org/10.1063/1.2874790.

[57] L. G. Villanueva et S. Schmid. “Evidence of Surface Loss as Ubiquitous Limiting Damping Mechanism in SiN Micro- and Nanomechanical Resonators”. In : *Phys. Rev. Lett.* 113 (22 nov. 2014), p. 227201. doi : 10.1103/PhysRevLett.113.227201. url : https://link.aps.org/doi/10.1103/PhysRevLett.113.227201.

[58] Janna Rodriguez et al. “Direct Detection of Akhiezer Damping in a Silicon MEMS Resonator”. In : *Scientific Reports* 9 (fév. 2019), p. 2244. doi : 10.1038/s41598-019-38847-6.

[59] Clarence Zener. “Internal Friction in Solids II. General Theory of Thermoelastic Internal Friction”. In : *Phys. Rev.* 53 (1 jan. 1938), p. 90-99. doi : 10.1103/PhysRev.53.90. url : https://link.aps.org/doi/10.1103/PhysRev.53.90.

[60] R. Ruby. “11E-2 Review and Comparison of Bulk Acoustic Wave FBAR, SMR Technology”. In : *2007 IEEE Ultrasonics Symposium Proceedings*. 2007, p. 1029-1040. doi : 10.1109/ULTSYM.2007.262.

[61] S. Pourkamali et al. “High-Q single crystal silicon HARPSS capacitive beam resonators with self-aligned sub-100-nm transduction gaps”. In : *Journal of Microelectromechanical Systems* 12.4 (2003), p. 487-496. doi : 10.1109/JMEMS.2003.811726.

[62] S. A. Chandorkar et al. “Limits of quality factor in bulk-mode micromechanical resonators”. In : *2008 IEEE 21st International Conference on Micro Electro Mechanical Systems*. 2008, p. 74-77. doi : 10.1109/MEMSYS.2008.4443596.

[63] Imtiaz Ahmed et al. “Super-High-Frequency Low-Loss Sezawa Mode SAW Devices in a GaN/SiC Platform”. In : *IEEE Transactions on Ultrasonics, Ferroelectrics, and Frequency Control* 70.4 (2023), p. 291-301. doi : 10.1109/TUFFC.2023.3241775.

[64] Ashwin K. Samarao et Farrokh Ayazi. “Temperature compensation of silicon micromechanical resonators via degenerate doping”. In : *2009 IEEE International Electron Devices Meeting (IEDM)*. 2009, p. 1-4. doi : 10.1109/IEDM.2009.5424221.

[65] Bao Jing-Fu, Muhammad Ammar Khan et Bao Fei-Hong. “Phononic Crystal Resonators”. In : *Phonons in Low Dimensional Structures*. Sous la dir. de Vasilios N. Stavrou. London : IntechOpen, 2018. Chap. 6. doi : 10.5772/intechopen.78584. url : https://doi.org/10.5772/intechopen.78584.

[66] Muhammad Wajih Ullah Siddiqi et Joshua E.-Y. Lee. “Wide Acoustic Bandgap Solid Disk-Shaped Phononic Crystal Anchoring Boundaries for Enhancing Quality Factor in AlN-on-Si MEMS Resonators”. In : *Micromachines* 9.8 (2018). issn : 2072-666X. doi : 10.3390/mi9080413. url : https://www.mdpi.com/2072-666X/9/8/413.

[67] A. H. Ghadimi et al. “Elastic strain engineering for ultralow mechanical dissipation”. In : *Science* 360.6390 (2018), p. 764-768. doi : 10.1126/science.aar6939. url : https://www.science.org/doi/abs/10.1126/science.aar6939.

[68] Y. Tsaturyan et al. “Ultracoherent nanomechanical resonators via soft clamping and dissipation dilution”. In : *Nature Nanotechnology* 12.8 (2017), p. 776-783. doi : 10.1038/nnano.2017.101.

[69] Ahmad Rahbar Ranji et al. “Recent Advances in MEMS-Based 3D Hemispherical Resonator Gyroscope (HRG)—A Sensor of Choice”. In : *Micromachines* 13.10 (2022). issn : 2072-666X. doi : 10.3390/mi13101676. url : https://www.mdpi.com/2072-666X/13/10/1676.

[70] David S. Bindel et Sanjay Govindjee. “Elastic PMLs for resonator anchor loss simulation”. In : *International Journal for Numerical Methods in Engineering* 64.6 (2005), p. 789-818. doi : https://doi.org/10.1002/nme.1394. eprint : https://onlinelibrary.wiley.com/doi/pdf/10.1002/nme.1394. url : https://onlinelibrary.wiley.com/doi/abs/10.1002/nme.1394.

[71] Ahmad Rahbar Ranji et al. “Design, Fabrication, and Dynamic Analysis of a MEMS Ring Resonator Supported by Twin Circular Curve Beams”. In : *Sensors* 24.14 (2024). issn : 1424-8220. doi : 10.3390/s24144499. url : https://www.mdpi.com/1424-8220/24/14/4499.

[72] Jing Wang, Z. Ren et C.T.-C. Nguyen. “1.156-GHz self-aligned vibrating micromechanical disk resonator”. In : *IEEE Transactions on Ultrasonics, Ferroelectrics, and Frequency Control* 51.12 (2004), p. 1607-1628. doi : 10.1109/TUFFC.2004.1386679.

[73] Guowei Zhi et al. “High performance BAW resonators with improved AlN thin films quality based on BaF2 buffer layer”. In : *Applied Physics Letters* 126.5 (fév. 2025), p. 052102. issn : 0003-6951. doi : 10.1063/5.0245758. eprint : https://pubs.aip.org/aip/apl/article-pdf/doi/10.1063/5.0245758/20372204/052102_1_5.0245758.pdf. url : https://doi.org/10.1063/5.0245758.

[74] Nicholas E. Bousse et al. “Dispersive readout of a high-Q encapsulated micromechanical resonator”. In : *Applied Physics Letters* 121.7 (août 2022), p. 073503. issn : 0003-6951. doi : 10.1063/5.0101402. eprint : https://pubs.aip.org/aip/apl/article-pdf/doi/10.1063/5.0101402/16484162/073503_1_online.pdf. url : https://doi.org/10.1063/5.0101402.

[75] Yang Yang, Corinne Dejous et Hamida Hallil. “Trends and Applications of Surface and Bulk Acoustic Wave Devices : A Review”. In : *Micromachines*. Micro/Nano Resonators, Actuators, and Their Applications 14(43) (jan. 2023), p. 21. doi : 10.3390/mi14010043. url : https://hal.science/hal-03939921.

[76] Tal Nagourney. “High-Q Fused Silica Micro-Shell Resonators for Navigation-Grade MEMS Gyroscopes”. Thèse de doct. Jan. 2018.

[77] Thomas D. Rossing et Mark French. “Science of Percussion Instruments”. In : *American Journal of Physics* 69.9 (sept. 2001), p. 1020-1021. issn : 0002-9505. doi : 10.1119/1.1383603. eprint : https://pubs.aip.org/aapt/ajp/article-pdf/69/9/1020/7529880/1020_2_online.pdf. url : https://doi.org/10.1119/1.1383603.

[78] T. Nagourney et al. “Micromachined high-Q fused silica bell resonator with complex profile curvature realized using 3D micro blowtorch molding”. In : *2015 Transducers - 2015 18th International Conference on Solid-State Sensors, Actuators and Microsystems (TRANSDUCERS)*. 2015, p. 1311-1314. doi : 10.1109/TRANSDUCERS.2015.7181172.

[79] A.W. Leissa et N.A. Jaber. “Vibrations of completely free triangular plates”. In : *International Journal of Mechanical Sciences* 34.8 (1992), p. 605-616. issn : 0020-7403. doi : https://doi.org/10.1016/0020-7403(92)90058-O. url : https://www.sciencedirect.com/science/article/pii/0020740392900580.

[80] COMSOL AB. *COMSOL Multiphysics® v6.1*. Finite element analysis software. COMSOL AB. Stockholm, Sweden, 2023. url : https://www.comsol.com.

[81] Thomas D. Rossing et Robert Perrin. “Vibrations of bells”. In : *Applied Acoustics* 20.1 (1987), p. 41-70. issn : 0003-682X. doi : https://doi.org/10.1016/0003-682X(87)90082-X. url : https://www.sciencedirect.com/science/article/pii/0003682X8790082X.

[82] Thomas D. Rossing et William J. Strong. “Acoustics of Bells edited by Thomas D. Rossing”. In : *The Journal of the Acoustical Society of America* 78.4 (oct. 1985), p. 1447-1448. issn : 0001-4966. doi : 10.1121/1.392879. eprint : https://pubs.aip.org/asa/jasa/article-pdf/78/4/1447/11782730/1447_1_online.pdf. url : https://doi.org/10.1121/1.392879.

[83] Mariana Domnica Stanciu et al. “Dynamic Analysis of the Musical Triangles—Experimental and Numerical Approaches”. In : *Applied Sciences* 12.12 (2022). issn : 2076-3417. doi : 10.3390/app12126275. url : https://www.mdpi.com/2076-3417/12/12/6275.

[84] L. Zoghaib et Pierre-Olivier Mattei. “Damping analysis of a free aluminum plate”. In : *Journal of Vibration and Control* 21 (oct. 2013), p. 2083-2098. doi : 10.1177/1077546313507098.

[85] A. Brenes et al. “Parameter estimation from nonlinear frequency response of MEMS resonators”. In : *2015 IEEE International Symposium on Circuits and Systems (ISCAS)*. 2015, p. 1318-1319. doi : 10.1109/ISCAS.2015.7168884.

[86] Ivan D. Breslavsky, Marco Amabili et Mathias Legrand. “Physically and geometrically non-linear vibrations of thin rectangular plates”. In : *International Journal of Non-Linear Mechanics* 58 (2014), p. 30-40. issn : 0020-7462. doi : https://doi.org/10.1016/j.ijnonlinmec.2013.08.009. url : https://www.sciencedirect.com/science/article/pii/S0020746213001637.

[87] Etienne Herth et al. “Micro-/Nanopillars for Micro- and Nanotechnologies Using Inductively Coupled Plasmas”. In : *physica status solidi (a)* 216.23 (2019), p. 1900324. doi : https://doi.org/10.1002/pssa.201900324. eprint : https://onlinelibrary.wiley.com/doi/pdf/10.1002/pssa.201900324. url : https://onlinelibrary.wiley.com/doi/abs/10.1002/pssa.201900324.

[88] E. Herth et al. “Fast ultra-deep silicon cavities : Toward isotropically etched spherical silicon molds using an ICP-DRIE”. In : *Journal of Vacuum Science & Technology B* 37 (mars 2019), p. 021206. doi : 10.1116/1.5081503.

[89] Y.-I. Lee et al. “Dry release for surface micromachining with HF vapor-phase etching”. In : *Journal of Microelectromechanical Systems* 6.3 (1997), p. 226-233. doi : 10.1109/84.623111.

[90] E. Herth et al. “Optimization of ohmic contact and adhesion on polysilicon in MEMS–NEMS wet etching process”. In : *Microelectronic Engineering* 88.5 (2011). The 2010 International workshop on “Materials for Advanced Metallization” - MAM 2010, p. 724-728. issn : 0167-9317. doi : https://doi.org/10.1016/j.mee.2010.06.032. url : https://www.sciencedirect.com/science/article/pii/S0167931710002182.

[91] Robert J. MacDonald et al. “Influence of Resist Profile on DRIE Sidewall Morphology”. In : *2021 32nd Annual SEMI Advanced Semiconductor Manufacturing Conference (ASMC)*. 2021, p. 1-4. doi : 10.1109/ASMC51741.2021.9435670.

[92] Etienne Herth et al. “Fast ultra-deep silicon cavities : Toward isotropically etched spherical silicon molds using an ICP-DRIE”. In : *Journal of Vacuum Science & Technology B* 37.2 (fév. 2019), p. 021206. issn : 2166-2746. doi : 10.1116/1.5081503. eprint : https://pubs.aip.org/avs/jvb/article-pdf/doi/10.1116/1.5081503/13293920/021206_1_online.pdf. url : https://doi.org/10.1116/1.5081503.

[93] A. Witvrouw et al. “Comparison between wet HF etching and vapor HF etching for sacrificial oxide removal”. In : *Proceedings of SPIE - The International Society for Optical Engineering* 4174 (août 2000). doi : 10.1117/12.396423.

[94] Wei Xu. “Modeling and fabrication of tunable 3D integrated Mirau micro-interferometers”. Theses. Université Paris Sud - Paris XI, déc. 2014. url : https://theses.hal.science/tel-01170068.

[95] M.P. Robinson et J. Clegg. “Improved determination of Q-factor and resonant frequency by a quadratic curve-fitting method”. In : *IEEE Transactions on Electromagnetic Compatibility* 47.2 (2005), p. 399-402. doi : 10.1109/TEMC.2005.847411.

[96] Wen-Teng Chang et Christian Zorman. “Electrical Characterization of Microelectromechanical Silicon Carbide Resonators”. In : *Sensors* 8.9 (2008), p. 5759-5774. issn : 1424-8220. doi : 10.3390/s8095759. url : https://www.mdpi.com/1424-8220/8/9/5759.

[97] Haoshen Zhu, Cheng Tu et Joshua Lee. “Anomalous DC-current-induced attenuation of Q factor in a silicon contour mode micromechanical resonator”. In : *2013 Joint European Frequency and Time Forum & International Frequency Control Symposium (EFTF/IFC)*. 2013, p. 141-144. doi : 10.1109/EFTF-IFC.2013.6702253.

[98] Feixia Pan et al. “Squeeze film damping effect on the dynamic response of a MEMS torsion mirror”. In : *Journal of Micromechanics and Microengineering* 8.3 (sept. 1998), p. 200. doi : 10.1088/0960-1317/8/3/005. url : https://doi.org/10.1088/0960-1317/8/3/005.

[99] Ashok Kumar Pandey et Rudra Pratap. “Effect of flexural modes on squeeze film damping in MEMS cantilever resonators”. In : *Journal of Micromechanics and Microengineering* 17.12 (nov. 2007), p. 2475. doi : 10.1088/0960-1317/17/12/013. url : https://doi.org/10.1088/0960-1317/17/12/013.

[100] David Ruffieux et al. “Silicon Resonator Based 3.2 W Real Time Clock With 10 ppm Frequency Accuracy”. In : *Solid-State Circuits, IEEE Journal of* 45 (fév. 2010), p. 224-234. doi : 10.1109/JSSC.2009.2034434.

[101] Samira Zali Asl et al. “A 3 ppm 1.5 × 0.8 mm 2 1.0 µA 32.768 kHz MEMS-Based Oscillator”. In : *IEEE Journal of Solid-State Circuits* 50 (2015), p. 291-302. url : https://api.semanticscholar.org/CorpusID:27277871.

[102] Giorgio Mussi et al. “An Outlook on Potentialities and Limits in Using Epitaxial Polysilicon for MEMS Real-Time Clocks”. In : *IEEE Transactions on Industrial Electronics* 67.8 (2020), p. 6996-7004. doi : 10.1109/TIE.2019.2938465.

[103] Weiguan Zhang, Haoshen Zhu et Joshua E.-Y. Lee. “Piezoresistive Transduction in a Double-Ended Tuning Fork SOI MEMS Resonator for Enhanced Linear Electrical Performance”. In : *IEEE Transactions on Electron Devices* 62.5 (2015), p. 1596-1602. doi : 10.1109/TED.2015.2414272.

[104] David Ruffieux et al. “A versatile timing microsystem based on wafer-level packaged XTAL/BAW resonators with sub-µW RTC mode and programmable HF clocks”. In : *Solid-State Circuits, IEEE Journal of* 49 (jan. 2014), p. 212-222. doi : 10.1109/JSSC.2013.2282111.

[105] Diego E. Serrano, Roozbeh Tabrizian et Farrokh Ayazi. “Electrostatically tunable piezoelectric-on- silicon micromechanical resonator for real-time clock”. In : *IEEE Transactions on Ultrasonics, Ferroelectrics, and Frequency Control* 59.3 (2012), p. 358-365. doi : 10.1109/TUFFC.2012.2204.

[106] Yunjia Li et al. “Capacitive Readout System for Micro Sensors and Actuators With Automatic Parasitic Cancellation”. In : *IEEE Transactions on Instrumentation and Measurement* 71 (2022), p. 1-10. doi : 10.1109/TIM.2021.3130203.

[107] Yuanjie Xu et Joshua E.-Y. Lee. “Single-Device and On-Chip Feedthrough Cancellation for Hybrid MEMS Resonators”. In : *IEEE Transactions on Industrial Electronics* 59.12 (2012), p. 4930-4937. doi : 10.1109/TIE.2011.2180274.

[108] Andrew N. Cleland. *Foundations of Nanomechanics*. Springer Berlin, Heidelberg, 2002. doi : 10.1007/978-3-662-05287-7.

[109] Hossein B. Khaniki, Mergen H. Ghayesh et Marco Amabili. “A review on the statics and dynamics of electrically actuated nano and micro structures”. In : *International Journal of Non-Linear Mechanics* 129 (2021), p. 103658. issn : 0020-7462. doi : https://doi.org/10.1016/j.ijnonlinmec.2020.103658. url : https://www.sciencedirect.com/science/article/pii/S0020746220303206.

[110] Stephen D. Senturia. *Microsystem Design*. Boston, MA : Springer US, 2001. doi : 10.1007/b117574.

[111] Matthew A. Hopcroft, William D. Nix et Thomas W. Kenny. “What is the Young’s Modulus of Silicon?” In : *Journal of Microelectromechanical Systems* 19.2 (2010), p. 229-238. doi : 10.1109/JMEMS.2009.2039697.